Measuring and modeling investigation of the Net Photochemical Ozone Production Rate via an improved dual-channel reaction chamber technique

Yixin Hao[1,2#], Jun Zhou[1,2#*], Jie-Ping Zhou[1,2], Yan Wang[1,2], Suxia Yang[1,2], Yibo Huangfu[1,2], Xiao-Bing Li[1,2], Chunsheng Zhang[3], Aiming Liu[3], Yanfeng Wu[1,2], Yaqing Zhou, Shuchun Yang[1,2], Yuwen Peng[1,2], Jipeng Qi[1,2], Xianjun He[1,2], Xin Song[1,2], Yubin Chen[1,2], Bin Yuan[1,2*], Min Shao[1,2]

[1]Institute for Environmental and Climate Research, Jinan University, Guangzhou 511443, China

[2]Guangdong-Hongkong-Macau Joint Laboratory of Collaborative Innovation for Environmental Quality, Guangzhou 511443, China

[3]Shenzhen National Climate Observatory, Shenzhen 518040, China

[#]Yixin Hao and Jun Zhou contribute equally to this work.

Correspondence to: Jun Zhou (Junzhou@jnu.edu.cn) and Bin Yuan (byuan@jnu.edu.cn)

Abstract. Current process-based research mainly uses box models to evaluate the photochemical ozone production and destruction rates, and it is not clear to what extent the photochemical reaction mechanisms are understood. Here, we modified and improved a net photochemical ozone production rate (NPOPR, $P(O_3)_{net}$) detection system based on the current dual-channel reaction chamber technique, which makes the instrument applicable to different ambient environments, and its various operating indicators were characterized, i.e., airtightness, light transmittance, wall losses of the reaction and reference chambers, conversion rate of O_3 to NO_2, air residence time, and performance of the reaction and reference chambers. The limits of detection of the NPOPR detection system were determined to be 0.07, 1.4, and 2.3 ppbv h^{-1} at sampling flow rates of 1.3, 3, and 5 L min^{-1}, respectively. We further applied the NPOPR detection system to field observations at an urban site in the Pearl River Delta (China). During the observation period, the maximum value of $P(O_3)_{net}$ was 34.1 ppbv h^{-1}, which was ~ 0 ppbv h^{-1} at night within the system detection error and peaked at approximately noon local time. The daytime (from 6:00–18:00) average value of $P(O_3)_{net}$ was 12.8 ($\pm$5.5) ppbv h^{-1}. We investigated the detailed photochemical O_3 formation mechanism in the reaction and reference chambers of the NPOPR detection system using a zero-dimensional box model. We found that the photochemical reactions in the reaction chamber were very close to those in ambient air, but it was not zero chemistry in the reference chamber, the reaction related to the production and destruction of RO_2 (=HO_2+RO_2) continued in the reference chamber, which

33 led to a small amount of $P(O_3)_{net}$. Therefore, the $P(O_3)_{net}$ measured here can be regarded as the lower

34 limit of the real $P(O_3)_{net}$ in the atmosphere; however, the measured $P(O_3)_{net}$ was still ~ 7.5 to 9.3 ppbv h$^-$

35 ^{1} higher than the modeled $P(O_3)_{net}$ value depending on different modeling methods, which may be due to

36 the inaccurate estimation of HO_2/RO_2 radicals in the modeling study. Short-lived intermediate

37 measurements coupled with direct $P(O_3)_{net}$ measurements are needed in the future to better understand

38 O_3 photochemistry. Our results show that the NPOPR detection system can achieve high temporal

39 resolution and continuous field observations, which helps us to better understand photochemical O_3

40 formation and provides a key scientific basis for continuous improvement of air quality in China.

1 Introduction

Surface O_3 pollution has become a major challenge in air quality management in China (Shen et al., 2021). Elevated surface O_3 mixing ratios exert severe adverse effects on public health, such as respiratory diseases, and the estimated annual mortality attributable to surface O_3 exposure exceeds 150,000 deaths in China (Malley et al., 2017). O_3 pollution is also detrimental to key staple crop yields, reducing the yields of wheat, soybean, and maize by up to 15 %, and is threatening global food security (Avnery et al., 2011; Mills et al., 2018; Karakatsani et al., 2010; Berman et al., 2012; O'Neill et al., 2003). As a greenhouse gas, O_3 also contributes significantly to climate change (Bell et al., 2004). With the rapid economic development and urbanization in the Pearl River Delta (PRD) region in China, O_3 pollution is pretty severe, especially in summer and autumn (Zou et al., 2015; Zhang et al., 2021).

The variation in O_3 in the planetary boundary layer is predominantly influenced by deposition, advection transport, vertical mixing (i.e., entrainment from the stratosphere), meteorological factors, and chemical reactions. Therefore, the O_3 budget in the boundary layer can be expressed as Eq. (1):

$$\frac{\partial[O_3]}{\partial t} = \underbrace{P(O_3) - D(O_3)}_{P(O_3)_{net}} \underbrace{- \frac{v}{H}[O_3]}_{SD} + \underbrace{u_i\frac{\partial[O_3]}{\partial x_i}}_{A} + STE \tag{1}$$

where SD, A, and STE represent the surface deposition, advection, and stratosphere-troposphere exchange (STE), respectively; $[O_3]$, $P(O_3)$ and $D(O_3)$ are the ambient O_3 mixing ratios, photochemical O_3 production and its loss rate, respectively; v, H, and u_i represent the O_3 deposition velocity, mixing layer height, and velocity in three directions, respectively; and A consists of u_i times the O_3 gradient in those three directions.

Tropospheric O_3 is a key component of photochemical smog, mainly formed by photochemical reactions of nitrogen oxides ($NO_x=NO+NO_2$) and volatile organic compounds (VOCs) (Lee et al., 2010). The specific process of the photochemical reaction is the photolysis of NO_2 at < 420 nm to generate $O(^3P)$ atoms, thereby promoting the formation of O_3 (Sadanaga et al., 2017). Simultaneously, there is a RO_X ($RO_X = OH + HO_2 + RO_2$) radical cycle in the troposphere, which continuously provides HO_2 and RO_2 to oxidize NO to NO_2 resulting in the accumulation of O_3 (Shen et al., 2021; Sadanaga et al., 2017; Cazorla et al., 2010).

Typical meteorological scenarios for the occurrence of O_3 pollution episodes in polluted urban

71 centers are usually characterized by weak winds, strong solar radiation, and high temperature (T). Under

72 such conditions, local formation of O_3 plays a crucial role in the rapid increase of surface O_3 in daytime.

73 In addition, in Eq. (1), the surface deposition and advection of O_3 are proportional to ambient O_3 mixing

74 ratios, $[O_3]$, which is mainly generated by local photochemistry (Carzorla et al., 2010). If $P(O_3)_{net}$ can be

75 reduced by regulatory measures, overall O_3 levels will decline proportionately over time (Cazorla et al.,

76 2010), thus, the investigation of $P(O_3)_{net}$ formation mechanism is urgently needed.

77   Current studies on $P(O_3)_{net}$ estimation mainly rely on modeling methods, the gas-phase chemical

78 mechanisms were frequently used to identify key drivers of O_3 pollution events and provide guidance for

79 making effective O_3 reduction strategies, such as the Master Chemical Mechanism (MCM), the regional

80 atmospheric chemistry mechanism (RACM), the Carbon Bond mechanisms (CBM) and the Mainz

81 Organic Mechanism (MOM) (Shen et al., 2021; Kanaya et al., 2016; Wang et al., 2014; Tadic et al.,

82 2020; Ren et al., 2013; Lu et al., 2010; Zhou et al., 2014; Mazzuca et al., 2016). However, uncertainties

83 in emission inventories, chemical mechanisms, and meteorology make it difficult to perfectly reproduce

84 real atmospheric processes, which can lead some bias in modeling the $P(O_3)_{net}$. According to the existing

85 field observations, researchers found that the mixing ratios of HO_2 or RO_2 obtained from the model

86 simulation was inconsistent with that obtained from the direct measurement, leading to the deviation of

87 $P(O_3)_{net}$ between observation and model simulation results (Wang et al., 2014; Tadic et al., 2020; Ren et

88 al., 2013; Martinez et al., 2003). Therefore, we urgently need a method that can directly measure the

89 $P(O_3)_{net}$.

90   Recently, researchers have developed sensors that can directly measure $P(O_3)_{net}$ in the atmosphere

91 using the dual-channel chamber technique (Sadanaga et al., 2017; Cazorla et al., 2010; Baier et al., 2015

92 and 2017; Sklaveniti et al., 2018), where ambient air is introduced into two chambers of identical size,

93 one UV transparent chamber (reaction chamber) and one UV protection chamber (reference chamber).

94 In the presence of solar UV light, O_3 is produced by photochemical reactions in the reaction chamber,

95 but not in the reference chamber. The system does not directly measure O_3 mixing ratios, it measures the

96 combined mixing ratios of O_3 and nitrogen dioxide (NO_2). $P(O_3)_{net}$ is determined by the difference of

97 $O_X(O_X=O_3+NO_2)$ mixing ratios between the reaction and reference chambers. These studies have greatly

98 helped us to understand the O_3 photochemical formation mechanism, but defects still exists in current

99 studies, for example, the sensors developed by Cazorla et al. (2010) and Baier et al. (2015) both have an

100 NO$_2$-to-O$_3$ converter unit, and uses a modified O$_3$ monitor (Thermo Scientific, Model 49i, USA) to

101 measure Ox, but the zero point of the O$_3$ monitor is easy to drift, together with the limitation of the

102 conversion efficiency of NO$_2$ to O$_3$ (~ 99.9 %) and the effects of the T and relative humidity (RH) to O$_3$

103 monitor, this method can introduce large measurement uncertainties. Sklaveniti et al. (2018) have shorten

104 the average residence time in the chambers to 4.5 min, which reduced the scattering and increased the

105 time resolution of ΔOx measurement, but large wall loss still exists in their system, which are 5 % and

106 3 % for O$_3$ and NO$_2$, respectively. Sadanaga et al. (2017) passed the NO standard gas into the PFA tube

107 to convert O$_3$ into NO$_2$ to detect Ox, which is easy to operate, but the LIF-NO$_2$ detector is less portable

108 and maintainable. Furthermore, all the current sensors have different degrees of wall loss of NO$_2$ and O$_3$

109 that can even reach 15 %, which largely affect the accuracy of the evaluation of $P(O_3)_{net}$.

110   In this study, we modified and improved a $P(O_3)_{net}$ sensor based on the dual-channel technique as

111 described above and named it the net photochemical ozone production rate (NPOPR) detection system.

112 Section 2 provides the improvement and characterization of the NPOPR detection system. Furthermore,

113 we applied the NPOPR detection system to an observation campaign conducted at Shenzhen

114 Meteorological Gradient Tower (SZMGT) in the Pearl River Delta (PRD) region in China. A zero-

115 dimensional box model based on the Framework for 0-D Atmospheric Modeling (F0AM) v3.2 coupled

116 with MCM v3.3.1 was used to simulate the photochemical reactions inside both the reaction and

117 reference chambers in the NPOPR system, which allowed us to assess the ability of the current modeling

118 method to model $P(O_3)_{net}$, as described in Sect. 3. The current research could help us study the source

119 and formation mechanism of O$_3$ and provide effective theoretical support for the prevention and control

120 of O$_3$ pollution. Because the system can directly obtain real-time $P(O_3)_{net}$ under different environmental

121 conditions, it can meet richer and more specific research needs.

122 **2 Method and materials**

123 **2.1 Development of the NPOPR detection system**

124 A schematic and actual diagram of the NPOPR detection system are shown in Fig. 1. The integral

125 construction is similar to the $P\text{-}L(Ox)$ measurement system built by Sadanaga et al. (2017) and Sklaveniti

126 et al. (2018), which mainly consists of reaction and reference chambers with the same geometry and

127 made of quartz (190.5 mm inner diameter and 700 mm length; more details can be found in Fig. S1). To

128 prevent photochemical reactions inside the reference chamber, an ultraviolet (UV) protection Ultem film

129 (SH2CLAR, 3 M, Japan) was used to cover the outer surface to block sunlight with wavelengths < 390

130 nm. During the experiment, both the reaction and reference chambers were located outdoors and exposed

131 to sunlight directly to simulate genuine ambient photochemistry reactions. Ambient air was introduced

132 into the reaction and reference chambers at the same flow rate, and a Teflon filter was mounted before

133 the chamber inlet to remove fine particles. A stream of air from the two chambers was alternately

134 introduced into an NO-reaction chamber every 2 min to convert O_3 in the air to NO_2 in the presence of

135 high mixing ratios of NO ($O_3+NO=NO_2$), and the Ox mixing ratios from the outlet NO-reaction chamber,

136 i.e., the total NO_2 mixing ratios including the inherent NO_2 in the ambient and that converted from O_3,

137 were measured by a Cavity Attenuated Phase Shift (CAPS) NO_2 Monitor (Aerodyne research, Inc.,

138 Billerica MA, USA) to avoid other nitrogen oxide interferences to the NO_2 measurement (such as alkyl

139 nitrates, peroxyacyl nitrates, peroxynitric acid, nitrogen pentoxide, etc.). Compared to previous studies

140 that used a dual-channel UV-absorption O_3 monitor (Cazorla et al., 2010) or a laser-induced fluorescence

141 (LIF) LIF-NO_2 monitor (Sadanaga et al., 2017) for Ox measurements, our choice could make the NPOPR

142 detection system have a more stable zero-baseline and be more portable by assembling each part together,

143 i.e., put the CAPS NO_2 monitor, the automatic sampling system, and the automatic data sampling system

144 onto the indoor cabinets with the push-pull base, and put the dual chambers onto the outdoor shelf with

145 the push-pull base. Additionally, we modified the air sampling system to adjust the total air flow rates

146 freely from 1.3 to 5 L min^{-1} in the reaction and reference chambers, which enabled us to achieve different

147 air residence times from 3.8 to 21 min. This time range covered all the residence times from previous

148 studies using different Ox measurement techniques, which ranged from 4.5 to 20.5 min (Cazorla et al.,

149 2010; Baier et al., 2015; Sadanaga et al., 2017; Sklaveniti et al., 2018). According to the simulation

150 results described in Sect. 3, the reaction rates of O_3 formation and destruction pathways and the radicals

151 that play critical roles in photochemical O_3 formation, such as HO_2, RO_2 and OH, reached quasi-steady

152 states in approximately 3 min, so it was reasonable for us to set the air flow rate highest at 5 L min^{-1},

153 where the sampled air has already reacted for 3.8 min in the reaction and reference chambers. On the

154 other hand, this also demonstrated that it was reasonable to set the alternate sampling time for the reaction

155 and reference chambers at 2 min, where the sampled air actually has already reacted for at least 3.8 min

156 in the reaction and reference chambers. The switch system was controlled by two Teflon three-way

157   solenoid valves (001-0028-900, Parker, GER) located before the NO-reaction chamber (see Fig. 1). We

158   used homemade circuit control software (Four-Channel-Valves boxed) and a solenoid valve (001-0028-

159   900, Parker, GER) to automatically switch the sampling lines every 2 min. To keep the flow rates in the

160   reaction and reference chambers the same and avoid gas flow accumulation in the chamber, a pump

161   (pump 3) was connected to the Teflon three-way solenoid valves in parallel to the NO-reaction chamber

162   to evacuate the air that was not introduced into the NO-reaction chamber. To reduce NO interference, the

163   system used O_X to infer the amount of O_3 generated by photochemical reactions (Liu et al., 1977; Pan et

164   al., 2015; Lu et al., 2010). The difference between the Ox mixing ratios in the reaction and reference

165   chambers, denoted by ΔOx, represents the amount of O_3 generated by the photochemical reaction.

166     $P(O_3)_{net}$ was obtained by dividing ΔOx by the average residence time of air in the reaction chamber $\langle \tau \rangle$:

167     $$P(O_3)_{net} = P(O_X) = \frac{\Delta O_X}{\tau} = \frac{[O_X]_{reaction} - [O_X]_{reference}}{\tau} \tag{2}$$

168   Igor Pro version 6 was used to calculate $P(O_3)_{net}$ as follows: ① separate the data of the reaction

169   and the reference chambers into two sets using the recorded valve number of 1 (reaction chamber) and 0

170   (reference chamber) during the sampling time; ② for each 2 min period of data, delete the first 20 s and

171   the last 20 s when the signal was not stable, then average the rest data, and do the interpolate calculation

172   of the reference chamber dataset; ③ calculate the difference between the Ox mixing ratios in the reaction

173   and reference chambers (i.e., ΔO_X) at the time when the reaction chamber measured Ox; ④ divide ΔO_X

174   by the average residence time of air in the reaction chamber $\langle \tau \rangle$ and obtain $P(O_3)_{net}$ at a time resolution

175   of 4 min.

(a)

(b)
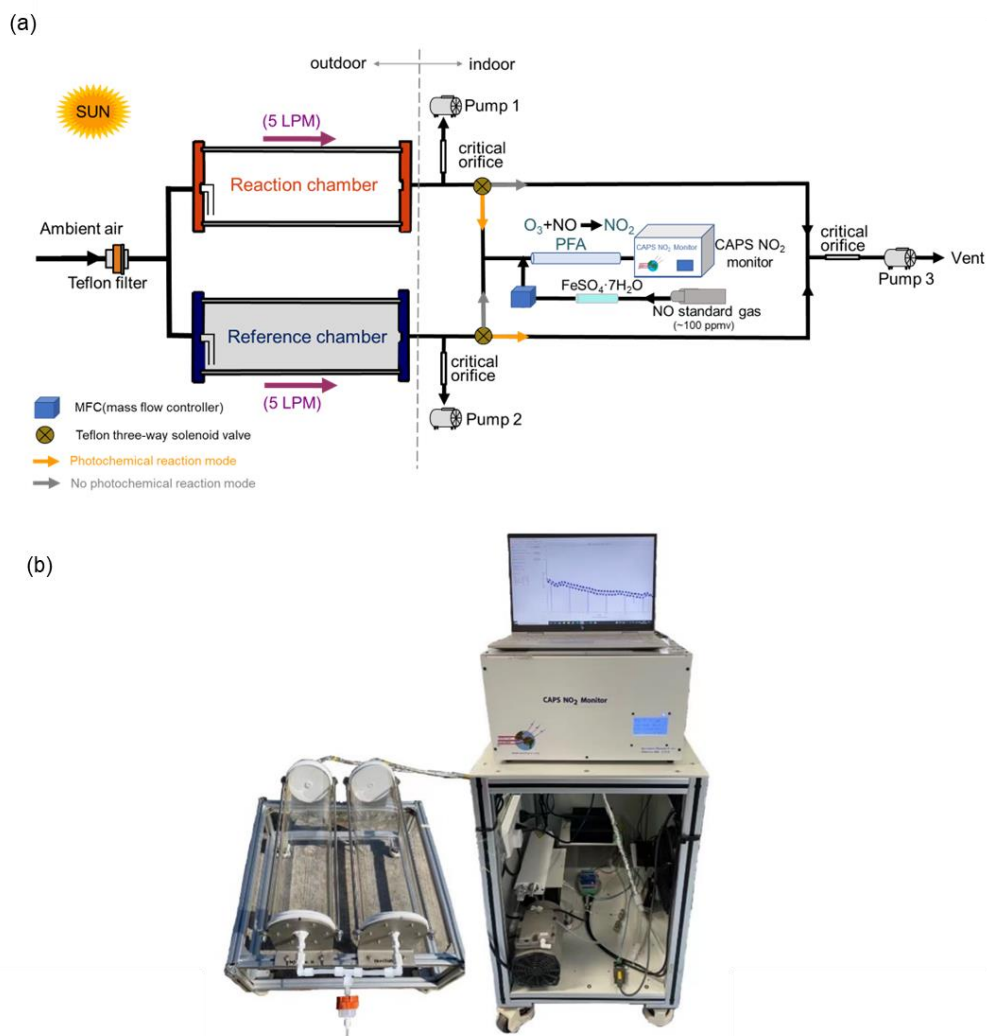
Figure 1: (a) Schematic and (b) actual diagram of the NPOPR detection system.

The major improvements of the NPOPR detection system described here compared to previous studies to optimize $P(O_3)_{net}$ measurements are as follows: (1) we improved the design of the reaction and reference chambers to ensure that they have good airtightness, which will increase the measurement accuracy of different species inside the chambers. More details can be found in Sect. 2.2 and Appendix I; (2) two pumps (labeled pump 1 and pump 2 in Fig. 1) were added directly after the reaction and reference chambers to continuously draw ambient air through the two chambers (as the makeup flow) to adjust the total air flow rates freely from 1.3 to 5 L min^{-1} in the chambers. By doing this, we were able to achieve different limits of detection (LODs) of the NPOPR system (see Sect. 2.4), making the instrument applicable to different ambient environments, i.e., in highly polluted areas, we could use higher air flow rates to reduce the wall loss effects of the chambers, and in less polluted areas, we could use lower flow rates to increase the instrument LOD. (3) We characterized the NPOPR detection system

189 at different air flow rates (including 1.3, 2, 3, 4, and 5 L min^{-1}) and tested the conversion efficiency of O_3

190 by NO to NO_2 in the NO-reaction chamber at different NO mixing ratios and NO-reaction chamber

191 lengths. These efforts enabled us to better understand the running parameters of the NPOPR system and

192 perform data corrections under different air flow rates (see Sect. 2.2); (4) we tested the performance of

193 both the reaction and reference chambers by combining the field measurements and MCM modeling,

194 which indicated that reaction pathways of $P(O_3)$ and $D(O_3)$ and the radicals that play critical roles in

195 photochemical O_3 formation, such as HO_2, RO_2 and OH, reached quasi-steady states in approximately 3

196 min, thus ensuring that the lowest air residence time of 3.8 min (at an air flow rate of 5 L min^{-1}) in the

197 reaction and reference chambers was long enough to obtain accurate $P(O_3)_{net}$ values (see Sect. 3.2). These

198 efforts made the NPOPR system less prone to biases than other systems and increased its applicability.

199 **2.2 Characterization of the NPOPR detection system**

200 We characterized the NPOPR detection system following the same procedures as previous researchers,

201 including the residence time of the air, the wall losses of NO_2 and O_3, the transmittance of light and

202 temperature differences in the reaction and reference chambers, and the quantitative conversion

203 efficiency of O_3 to NO_2 (α) in the NO-reaction chamber. Additionally, we investigated the residence time

204 of the air and the wall losses of NO_2 and O_3 in the reaction and reference chambers at different flow rates

205 (including 1.3, 2, 3, 4, and 5 L min^{-1}) and the conversion efficiency of O_3 by NO to NO_2 in the NO-

206 reaction chamber at different NO mixing ratios and NO-reaction chamber lengths. The detailed

207 experimental performances and data analysis are shown in Appendix I, and the corresponding results are

208 described as follows.

209 ***The residence time.*** We tested the residence time of air in both chambers under different air flow

210 rates, including 1.3, 2, 3, 4, and 5 L min^{-1}, the obtained related residence time in the reaction chamber

211 were 0.35, 0.16, 0.11, 0.07, and 0.06 h, respectively. By setting different air flow rates, we were able to

212 obtain different residence time thus different limit of detection of NPOPR system, which make it

213 applicable to different ambient environment. To make sure that the mean residence time of air is the same

214 in the reaction and reference chambers, we also tested the residence time of air in the reference chamber

215 in parallel, which were not much difference with that in the reaction chamber, as shown in Table S1. The

216 experimental schematic diagram is shown in Fig. S2, the related results of different air flow rates are

217   shown in Fig. S3 and Table S1.

218   ***Wall losses of NO$_2$ and O$_3$.*** At air flow rates of 1.3, 2, 3, 4, and 5 L min^{-1}, the wall losses of O$_3$ in

219   the reaction chamber were found to be approximately 2 %, 0 %, 0 %, 0 %, and 0 %, respectively, and the

220   wall losses of O$_3$ in the reference chamber were found to be approximately 2 %, 1 %, 1 %, 0 %, and

221   0.7 %, respectively. While the wall losses of NO$_2$ in the reaction chamber at air flow rates of 1.3, 2, 3, 4,

222   and 5 L min^{-1} were found to be approximately 4 %, 4 %, 2 %, 0 %, and 0.3 %, respectively, the wall

223   losses of NO$_2$ in the reference chamber were found to be approximately 2 %, 1 %, 0 %, 0 %, and 0. 6 %,

224   respectively. The experimental schematic diagram is shown in Fig. S4, and the related results of different

225   air flow rates are shown in Figs. S5-S6 and Tables S2-S5. We further compared the wall losses of O$_3$ and

226   NO$_2$ in the reaction and reference chambers at 5 L min^{-1} with previous studies (as shown in Table S6)

227   and found that they were significantly smaller, but even with a flow rate of 1.3 L min^{-1}, the wall losses

228   were still smaller than 4 % and 2 % in the reaction chamber and the reference chambers, respectively.

229   We also tested the wall losses of NO$_2$ and O$_3$ in the chamber at a 5 L min^{-1} flow rate at different humidities

230   of 35-75 %, the detailed results are shown in Fig. S7 and S8, which shows that the variation in humidity

231   effected the wall loss of NO$_2$ and O$_3$ by 0.03-0.12 % and 1.06-1.19 %, respectively, which is much

232   smaller than the instrument detection error (which is 2 % at ambient NO$_2$ mixing ratios of 0-100 ppb),

233   which indicates the small effects of Ox loss on $P(O_3)_{net}$ measurements in our NPOPR detection system.

234   ***The light transmittance and temperature differences in the reaction and reference chambers.*** It

235   is worth noting that there was still low transmittance of light ranging from 390 nm to 790 nm through

236   the UV protection film, and the reference chamber could not be regarded as completely dark; thus, we

237   tested the solar UV transmittance through the reaction and reference chambers of the NPOPR detection

238   system in the laboratory using a sunlight simulation lamp (SERIC XG-500B, Japan) to provide different

239   intensities of illumination. The photolysis frequencies of NO$_2$, O$_3$, HONO, H$_2$O$_2$, NO$_3$_M (photolysis of

240   NO$_3$ generates NO+O$_2$), NO$_3$_R (photolysis of NO$_3$ generates NO$_2$+O), HCHO_M (photolysis of HCHO

241   generates H$_2$+CO), and HCHO_R (photolysis of HCHO generates H+HCO) inside and outside the

242   reaction and reference chambers were measured using an actinic flux spectrometer (PFS-100; Focused

243   Photonics Inc., China). Table 1 presents the J(NO$_2$), J(O^{1}D), and J(HONO) results for the outside and

244   inside chambers from this study and from the literature. J(H$_2$O$_2$), J(NO$_3$_M), J(NO$_3$_R), J(HCHO_M),

245   and J(HCHO_R) are shown in Table S7.

246   The photolysis frequencies of all species inside the reaction chamber were in agreement with those

247 measured outside the reaction chamber within 4 %. Table S7 shows that the transmittivities of $J(H_2O_2)$,

248 $J(NO_3\_M)$, $J(NO_3\_R)$, $J(HCHO\_M)$, and $J(HCHO\_R)$ in the reaction chamber were more than 90 %.

249 However, we have observed that the transmittivities of $J(O^1D)$ were even higher than those of $J(HONO)$

250 (as shown in Table 1) in the reference chamber (which blocks sunlight at wavelengths < 390 nm),

251 theoretically, this is not possible according to JPL Publication 19-5 (Burkholder et al., 2020), where the

252 absorption cross section of HONO at wavelengths of 390-395 ranged from approximately $4.0\text{-}17.1\times10^{-21}$

253 cm^2, which is about two or three orders of magnitude higher than that of ozone (which ranged from

254 approximately $0.8\text{-}2.6 \times10^{-23}$ cm^2 at wavelengths of 390-410 nm), and the photolysis quantum yield of

255 HONO at wavelengths of 390-395 is unity, which is about ten times higher than that of ozone (~ 0.08).

256 This will surely make the J values of HONO inside the reference chamber (which only has sunlight with

257 wavelengths > 390 nm) higher than that of ozone, according to the Eq. (S9). We also found that the

258 transmittivity of HONO and O_3 in the reference chamber obtained from the TUV simulation (as described

259 in Sect. 3.2) were 0.01 and 0, respectively, as shown in Table S13. Therefore, we believe the non-zero

260 measurement results of the transmittivity of O_3 shown in Table 1 and Table S7 are mostly probably due

261 to the instrument measurement error, this error is relatively large due to a limit number of measurement

262 points (3 points for each species). We further evaluated the measurement error of J values based on the

263 instrument measurement error of the actinic flux spectrometer, which can reach ±5 % according to Bohn

264 et al. (2017), and re-evaluated the transmittivity error listed in Table 1 and Table S7 following the

265 procedures described in supplementary materials (Sect. 1.5). The calculation result from Eq. (S5) show

266 that the transmittivities errors are 0.07 for all species, within this error range, $J(O1D)$, $J(HONO)$, $J(H_2O_2)$,

267 $J(HCHO\_M)$, and $J(HCHO\_R)$ can be considered statistically indistinguishable from 0 in reference

268 chamber. However, $J(NO_2)$, $J(NO_3\_M)$, and $J(NO_3\_R)$ still distinctly positive values. Specifically, the

269 transmittivities of $J(NO_3\_M)$ and $J(NO_3\_R)$ of the reference chamber were more than 90 % (Table S7).

270 The influence of the measurement error of J values of all species on $P(O_3)_{net}$ will be discussed in Sect. 3.

271

272

273

274

275

276

277

Table 1. Transmittivities of photolysis frequency J (s^{-1}) values of different species in the reaction and reference chambers. The shaded and clear regions correspond to the transmittivities of J values in the reference (Ultem coated) and reaction (clear) chambers, respectively. The "transmittivities" column shows the transmittivities of the tested species from the measurements conducted with the set photolysis frequencies using SERIC XG-500B sunlight (this study) and ambient (literature). It should be noted that the errors listed here are relatively large and may not reliable due to a limit number of measurement points (3 points for each species). The calculated transmittivity errors are 0.07 for all species based on the ±5 % measurement error of the instrument.

	Transmittivities			
	Averaged (this study)	Cazorla *et al.*, 2010	Baier *et al.*, 2015	Sadanaga *et al.*, 2017
$J(NO_2)$	0.985 ±0.037	0.974	0.990	0.986
	0.094 ±0.014	0.021	0.01	0.121
$J(O^1D)$	1.020 ±0.04	0.991	0.978	1.030
	0.019 ±0.011	0.0058	0.001	~0
$J(HONO)$	0.983 ±0.037	0.976	0.982	0.988
	0.002 ±0.0002	0.0067	~0	0.017

We further detected the temperature in both the reaction and reference chambers when running the NPOPR system in an ambient observation campaign during November 2022 on the Panyu campus of Jinan University in Guangzhou, China (113° 36′ E, 23° 02′ N). We found that the UV protection Ultem film on the reference chamber did not block the heat outside the chamber, and the temperature remained the same in the reaction and reference chambers during the measurement test, as shown in Fig. S10.

The quantitative conversion efficiency of O_3 to NO_2 (α) in the NO-reaction chamber is crucial for accurate measurement of $P(O_3)_{net}$. Here, we used a perfluoroalkoxy (PFA) tube (outer diameter of 12.7 mm; inner diameter of 9.5 mm) as the NO-reaction chamber. The experimental schematic diagram is shown in Fig. S12. Known mixing ratios of O_3 and NO standard gas were introduced into the NO-reaction chamber, and NO reacted with O_3 to produce NO_2. To avoid the influence of small amounts of NO_2 impurity in the NO standard gas used for conversion, we added a cylinder filled with partialized crystals of $FeSO_4 \cdot 7H_2O$ to reduce NO_2 in the NO/N_2 gas cylinder to NO. We injected ~1800 ppbv NO into the NO-reaction chamber and tested the NO_2 mixing ratios from its outlet using a CAPS NO_2 monitor, as shown in Fig. S13. We found that the standard deviation of the NO_2 mixing ratios was lower than 0.027

ppbv, which is smaller than the baseline drifts of the CAPS (which were 0.043 and 0.030 ppbv (1 σ) at

integration times of 35 and 100 s, respectively, as mentioned in Sect. 2.3), so we believe the particulate

crystals of $FeSO_4 \cdot 7H_2O$ performed well and the potential bias introduced by the impurity in NO mixing

ratio for $P(O_3)_{net}$ was negligible. Finally, the total NO_2 mixing ratios, including that from the ambient air,

were measured using a CAPS NO_2 monitor ($[NO_2]_{CAPS}$). The O_3 mixing ratios were controlled at

approximately 310 ppbv according to the maximum mixing ratio range in the normal ambient atmosphere

(to ensure that all ambient and newly generated O_3 can react with NO and produce equivalent amounts

of NO_2). An O_3 generator equipped with a low-pressure mercury lamp was employed to generate O_3, and

the generated O_3 mixing ratios ($[O_3]_g$) were measured by a 2B O_3 monitor as mentioned above. Here, we

note that the O_3 mixing ratios were diluted by the added NO/N_2 gas (with a flow rate of 20 mL min^{-1}) in

the NO-reaction chamber (with a total flow rate of 1.11 L min^{-1}), taking 1800 ppbv NO/N_2 gas as an

example, the relationship between $[NO_2]_{CAPS}$ and $[O_3]_g$ can be described by Eq. (3):

$$[NO_2]_{CAPS} = \frac{1.09}{1.11}[O_3]_g \alpha \tag{3}$$

To determine the optimal length of the NO-reaction chamber and NO mixing ratios, we performed

a cross test of α under the following scenarios: the NO-reaction chamber lengths were increased from 30

to 650 cm in 50 cm steps, and the NO standard gas (102.1 ppmv) was diluted to 600, 900, 1200, 1500,

1800, 2100, and 2400 ppbv in the NO reaction chamber. The results are shown in Fig. 2. We found that

at $[O_3]_g$ of approximately 310 ppbv, with NO mixing ratios $\geq$1800 ppbv in the NO reaction chamber, α

reached 99 %, 99.6 %, and 99.9 % with NO-reaction chamber lengths of 50, 70, and 100 cm, respectively,

where the corresponding O_3 residence times in the NO reaction chamber were 1.95, 2.74, and 3.91 s,

respectively. Considering both the optimal reaction time in the NO reaction chamber and α, we selected

the NO reaction chamber length as 100 cm with an NO mixing ratio of 1800 ppbv for the NPOPR

detection system.
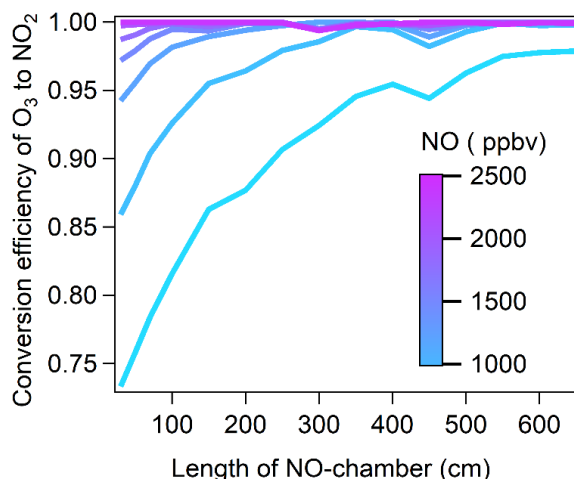
Figure 2: The conversion efficiency of O₃ by NO to NO₂ in the NO reaction chamber as a function of the NO chamber length, color coded by the NO mixing ratios.

The airtightness of the reaction and reference chambers We also checked the airtightness of the reaction and reference chambers by passing through gases with different flow rates based on the schematic diagram shown in Fig. S14 and compared the values of [air flow rate × pressure] between the inlet and outlet of the chambers (as indicated in Fig. 3). We found that the deviations in [air flow rate × pressure] at the inlet and outlet of the reaction and reference chambers at different flow rates were <3 % (as shown in Table S8), indicating the good airtightness of the reaction and reference chambers. This ensured that the photochemical reactions in the reaction and reference chambers would not be affected by the ambient air outside the chambers.
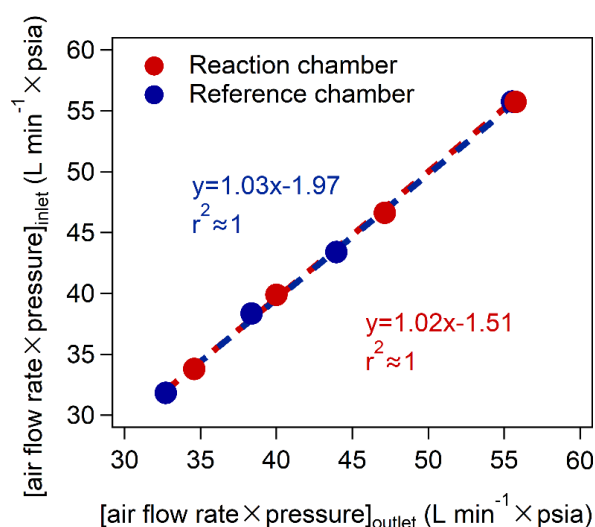
Figure 3: The relationship of the values of [air flow rate × pressure] between the inlet and outlet of the chambers (psia: Pounds Per Square Inch Absolute).

340

The flow states in the reaction and reference chambers We calculated the Reynolds number to check the gas flow state in the reaction and reference chambers. The Reynolds number (expressed as Eq. (4)) is a dimensionless number that can be used as the basis for judging the flow characteristics of a fluid:

$$Re = \rho v d / \mu \tag{4}$$

where v, ρ and μ are the flow velocity, density and viscosity coefficient of the fluid, respectively. In this study, the fluid is air, and d is the equivalent diameter of the reaction and reference chambers. The calculated Reynolds numbers in the two chambers under flow rates of 1.3, 2, 3, 4, and 5 L min^{-1} were 9.39, 14.58, 21.75, 29.05, and 36.34, respectively, indicating laminar flows in both chambers at different flow rates.

The HONO production in the reaction and reference chambers We tested the HONO production in the reaction and reference chambers under weather conditions similar to those during the SZMGT observations (humidity of 60-90% at a temperature of ~ 20 °C and $J(NO_2)$ of ~ 0-8 × 10^{-3} s^{-1}) at a 5 L min^{-1} sampling flow rate. We found that the HONO mixing ratios in the reaction and reference chambers were almost the same and not statistically different from that in the ambient air within the standard deviation, as shown in Fig. S9; therefore, we assumed that the HONO production in the reaction and reference chambers would not cause a significant difference in $P(O_3)_{net}$ in the two chambers. Unfortunately, we did not test HONO during the field observation period, but we have added the modeled HONO produced from the precursors before the ambient air was injected into the NPOPR system, as described in Sect. 3.2.

2.3 Calibration and measurement error of the CAPS NO$_2$ monitor

The Ox in the NPOPR detection system was measured by the CAPS NO$_2$ monitor. Detailed descriptions of this technique can be found elsewhere (Kebabian et al., 2008, 2005). We calibrated the CAPS NO$_2$ monitor using a NO$_2$ standard gas (with an original mixing ratio of 2.08 ppmv), which was first calibrated using the gas-phase titration method using NO standard gas and excessive O$_3$. The related experimental results are shown in Fig. S15. The detailed calibration procedure is as follows: a. injected ~ 10–100 ppbv of NO$_2$ standard gas for 30 min to passivate the surfaces of the monitor and then injected dry pure air for ~ 10 min to minimize the zero point drift, which were 0.043 and 0.047 ppbv at integration times of 35 and 100 s, respectively, and resulted in LODs of CAPS of 0.13 and 0.14 ppbv (3 σ), respectively; b.

369   injected a wide range of NO_2 mixing ratios (from 0–160 ppbv) prepared by mixing the NO_2 standard gas

370   with ultrapure air into the CAPS NO_2 monitor and repeated the experiments three times at each NO_2

371   mixing ratio. The final results are shown in Fig. 4. To check the baseline drift of the CAPS at different

372   humidities, we added another two sets of tests (as shown in Fig. S11) using ambient air and wet pure air

373   and found that (a) when injecting ambient air into the CAPS (RH ranged from ~30-35%), the baseline

374   drifts were 0.035 and 0.032 ppbv (1 σ) at integration times of 35 and 100 s, respectively; and (b) when

375   injecting wet pure air into the CAPS (RH ranged from 35-70%), the baseline drifts were 0.043 and 0.030

376   ppbv (1 σ) at integration times of 35 and 100 s, respectively. These baseline drifts were smaller than those

377   when injecting dry pure air to estimate the LOD of the CAPS. We chose the largest baseline drift when

378   injecting dry pure air to estimate the $P(O_3)_{net}$ error in the following analysis; by doing this, we were able

379   to include all the short-duration baseline drifting in the CAPS NO_2 monitor under different humidities.

380   To obtain an accurate measurement error of the CAPS NO_2 monitor (($O_{X_{CAPS}})_{error}$), we fitted the

381   calibration results with a 68.3 % confidence level, and the blue line in Fig. 4 represents the maximum

382   fluctuation range under this confidence level. $(O_{X_{CAPS}})_{error}$ was then calculated from the fluctuation

383   range of the 68.3 % confidence interval of the calibration curve. The relationship between $(O_{X_{CAPS}})_{error}$

384   and the measured Ox value ($[Ox]_{measured}$) can be expressed as a power function curve, as shown in Eq.

385   (5):

386    $$(O_{X_{CAPS}})_{error} = 9.72 \times [O_X]_{measured}^{-1.0024} \tag{5}$$

387   Subsequent $P(O_3)_{net}$ error estimation according to the instrument measurement error of the CAPS

388   NO_2 monitor and the O_3 light-enhanced loss in the reaction and reference chambers are described in

389   Appendix II.
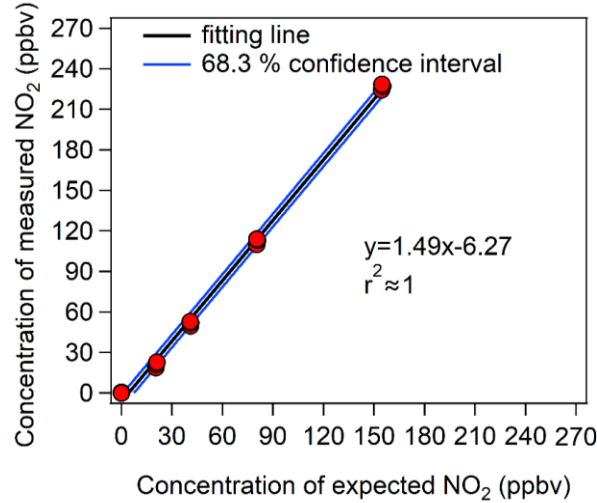
390

391 **Figure 4: Calibration results of the CAPS NO₂ monitor with different NO₂ mixing ratios. The y-axis represents**

392 **the NO₂ mixing ratios measured by the CAPS NO₂ monitor, and the x-axis represents the prepared NO₂**

393 **mixing ratios from the diluted NO₂ standard gas.**

394 **2.4 The measurement error of $P(O_3)_{net}$ and the LOD of the NPOPR detection system**

395 To assess the measurement error of $P(O_3)_{net}$ and the LOD of the NPOPR detection system, dry pure air

396 was introduced into the NPOPR detection system in sequence to adjust the system for ~ 2 h, followed by

397 dry pure air or ambient air when the time resolution of the CAPS NO₂ monitor was 1 s and the integration

398 time period was 100 s (the measurement durations for the reaction and reference chambers were both 2

399 min). The LOD of the NPOPR detection system was obtained as three times the measurement error of

400 $P(O_3)_{net}$, which was determined at a time resolution of 4 min by propagating the errors of the Ox measured

401 by the CAPS NO₂ monitor when ultrapure air or ambient air was introduced into the NPOPR detection

402 system, combined with the related $\langle \tau \rangle$ under different flow rates, i.e., $\langle \tau \rangle$ was 0.063 h at a flow rate of 5

403 L min⁻¹. The detailed calculation method is shown in Eq. (6):

404 $$LOD = \frac{3 \times \sqrt{([O_X]_{rea\_std})^2 + ([O_X]_{ref\_std]})^2}}{\tau} \tag{6}$$

405 where $[O_X]_{rea\_std}$ and $[O_X]_{ref\_std}$ represent the standard deviation of O_X in the reaction and reference

406 chambers measured by the CAPS NO₂ monitor with an integration time period of 100 s, respectively.

407 However, considering that the background Ox mixing ratios (measured by the CAPS NO₂ monitor

408 of the air in the reference chamber) changed when measuring the ambient air, the measured O_X errors in

409 the reaction and reference chambers changed with the Ox mixing ratios (as shown in Sect. 2.3), and the

410 LOD must also be a function of the intrinsic ambient and photochemically formed O_3 and NO₂ mixing

411   ratios (i.e., the Ox mixing ratios measured by the CAPS NO_2 monitor). It is worth noting that the

412   measured O_X errors may also be influenced by the light-enhanced loss of O_3 in the reaction and reference

413   chambers under ambient conditions when the light intensity (especially $J(O^1D)$) and O_3 mixing ratios are

414   high, as tested and shown in Appendix II, but this effect is included in the measured O_X errors. Therefore,

415   when injecting ambient air into the NPOPR system, the error and LOD of $P(O_3)_{net}$ with a residence time

416   of τ can be calculated using Eq. (7) and Eq. (8), respectively:

417 $$P(O_3)_{net\_error}=\frac{\sqrt{(O_{X_\gamma})_{rea\_error}^2+((9.72\times[(O_X]_{rea\_measured}^{-1.0024})_{rea\_std})^2+(O_{X_\gamma})_{ref\_error}^2+((9.72\times[(O_X]_{ref\_measured}^{-1.0024})_{ref\_std})^2}}{\tau} \qquad (7)$$

418 $$LOD= 3\times P(O_3)_{net\_error} \qquad (8)$$

419   where $(O_{X_\gamma})_{rea\_error}$ and $(O_{X_\gamma})_{ref\_error}$ represent the measurement error caused by the light-enhanced loss

420   of O_3 in the reaction and reference chambers, respectively, and $(9.72\times[O_X]_{measured}^{-1.0024})_{rea\_std}$ and

421      $(9.72\times[O_X]_{measured}^{-1.0024})_{ref\_std}$ represent the standard deviation of O_X in the reaction and reference

422   chambers caused by the CAPS NO_2 monitor with an integration time period of 100 s, respectively. More

423   details about the $(O_{X_\gamma})_{rea\_error}$ and $(O_{X_\gamma})_{ref\_error}$ estimation method can be found in Appendix II.

424   In conclusion, the LOD of the NPOPR detection system is determined to be three times $P(O_3)_{net\_error}$,

425   where $P(O_3)_{net\_error}$ is mainly determined by the measurement error of Ox (including the Ox measurement

426   error of the CAPS NO_2 monitor, the light-enhanced loss of O_3, and the chamber Ox losses). Because the

427   measurement error of the CAPS NO_2 monitor decreases with increasing Ox mixing ratios (as shown in

428   Sect. 2.3), higher LODs could be obtained when injecting dry pure air into the NPOPR detection system,

429   which were approximately 0.07, 1.4, and 2.3 ppbv h^{-1} at air flow rates of 1.3, 3, and 5 L min^{-1}, respectively.

430   The results are summarized in Table S9.

431   During the field observations, the LOD values were highly dependent on the ambient conditions,

432   especially the light intensity and the Ox mixing ratios, and higher O_3 mixing ratios and lower light

433   intensity will likely result in lower LOD values.

434   **2.5 Laboratory tests of the NPOPR detection system**

435   We conducted an experiment in the laboratory to test the performance of the NPOPR detection system at

436   Jinan University Panyu Campus (23.0° N, 113.4° E) on 26 March 2021. Ambient air (5 L min^{-1}) was

437 simultaneously injected into the reaction and reference chambers of the NPOPR detection system in

438 parallel, and the sunlight simulation lamp mentioned above was used to simulate sunlight radiation. The

439 light intensities of the sunlight simulation lamp were decreased from 26000 cd to 0 cd in steps of 3700

440 cd, where cd indicates the light intensity SI unit candela. $P(O_3)_{net}$ was 28.6 ppbv h^{-1} at a light intensity of

441 26000 cd and gradually approached 0 ppbv h^{-1} at 0 cd (as shown in Fig. 5), indicating that the $P(O_3)_{net}$

442 change due to the different sunlight radiation could be well captured by the NPOPR detection system.
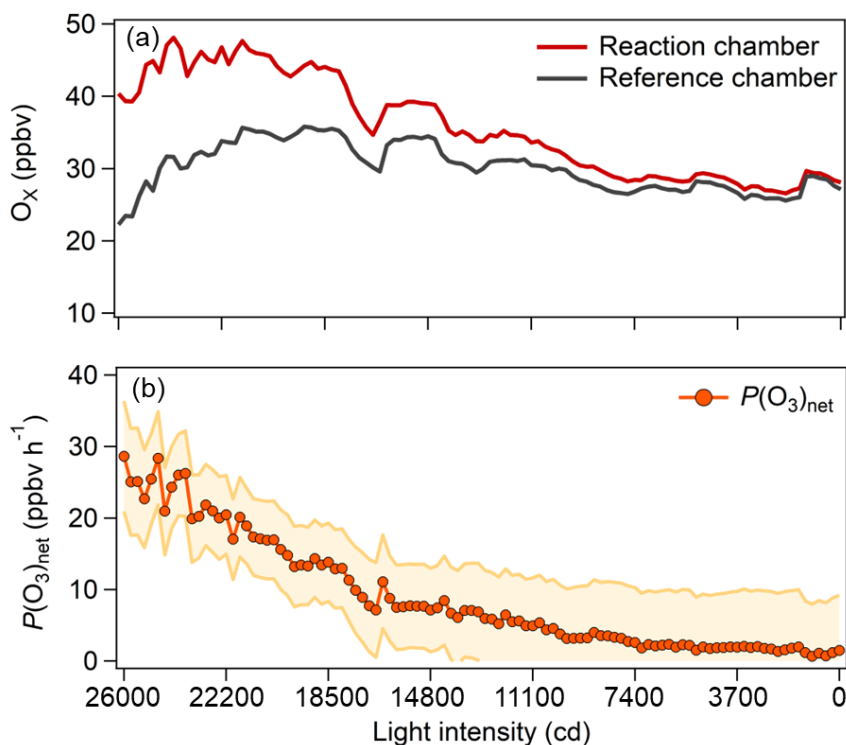
443
444 **Figure 5: (a) Measured Ox mixing ratios in the reaction and reference chambers and (b) the related $P(O_3)_{net}$**
445 **as a function of the light intensity during the experiment.**

446 **3 Atmospheric study and discussion**

447 **3.1 Field observations**

448 The self-built NPOPR detection system was employed in the field campaign conducted at SZMGT, which

449 is located in Shenzhen, China (as shown in Fig. S17), from 7 to 9 December 2021. During the campaign,

450 to achieve the lowest O_3 and NO_2 wall loss, we used a 5 L min^{-1} air flow rate in the reaction and reference

451 chambers (with a residence time of ~ 4 min). The photolysis frequencies of different species were

452 measured using the actinic flux spectrometer as mentioned above. O_3 and NO_X (NO+NO_2) mixing ratios

453 were measured using a 2B O_3 monitor and a chemiluminescence NOx monitor (Model 42i, Thermo

454 Fisher Scientific, USA), respectively. *T* and RH were measured by a portable weather station (Met Pak,

455 Gill Instruments Ltd, UK). Volatile organic compounds (VOCs) were measured by high-resolution

456 proton transfer reaction time-of-flight mass spectrometry (PTR-ToF-MS, Ionicon Analytik, Austria)

457 (Wang et al., 2020a; Wu et al., 2020) and an off-line gas chromatography mass spectrometry flame

458 ionization detector (GC–MS-FID) technique (Wuhan Tianhong, Co. Ltd, China) (Yuan et al., 2012)

459 (Table S11). Additionally, a self-built formaldehyde analyzer was used to detect formaldehyde (HCHO)

460 (Zhu et al., 2020). Figure 6 presents the temporal and diurnal variations in the $P(O_3)_{net}$, O_X, O_3, NO,

461 NO_2, NO_X, *T*, RH, $J(O^1D)$, and $J(NO_2)$ mixing ratios at SZMGT during the campaign.
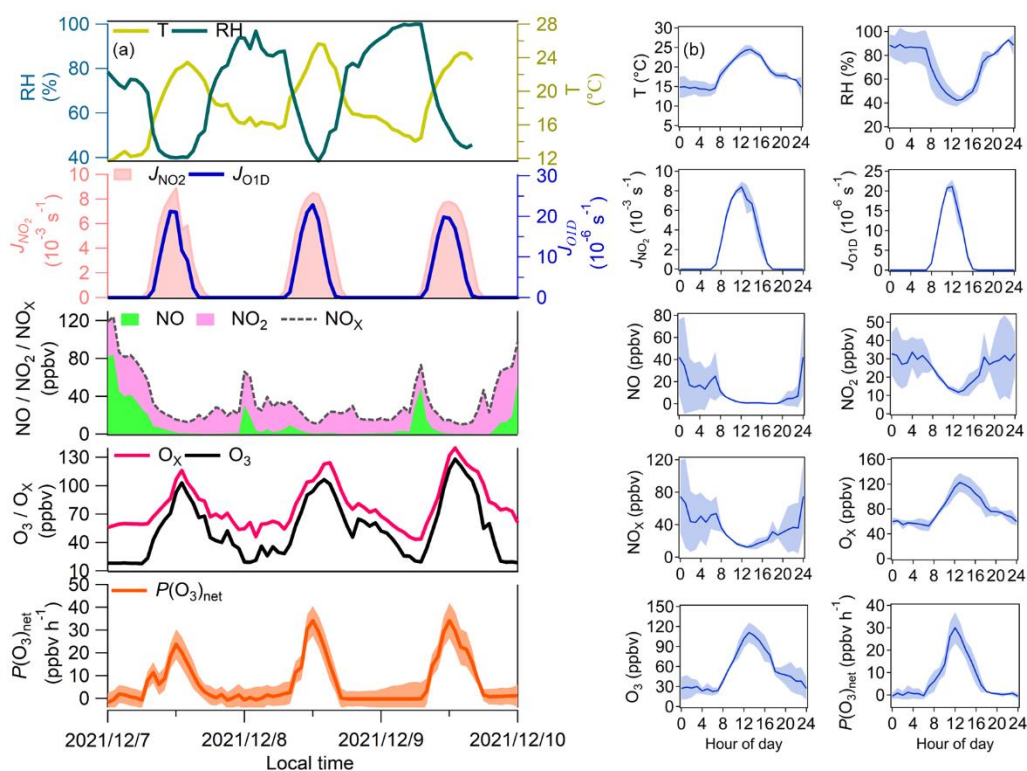
462

463 **Figure 6: (a) Time series and (b) average diurnal variations of $P(O_3)_{net}$, $J(NO_2)$, $J(O^1D)$, T, RH, O_X, NO_2 and**

464 **NO measured at SZMGT from 7 to 9 December 2021. The shaded areas represent the error of each measured**

465 **species, where the error of $P(O_3)_{net}$ was calculated according to the method described in Appendix II (the**

466 **estimation of the $P(O_3)_{net}$ error).**

467

468 During the measurement period, $P(O_3)_{net}$ ranged from ~ 0 to 34.1±7.8 ppbv h^{-1}, with an average

469 daytime (from 6:00–18:00) value of 12.8 (±5.5) ppbv h^{-1}. The maximum $P(O_3)_{net}$ at SZMGT was lower

470 than that measured in the urban area of Houston in the US (40–50 ppbv h^{-1} and 100 ppbv h^{-1} in autumn

471 and spring, respectively) (Baier et al., 2015; Ren et al., 2013), close to that measured in Indiana in the

472 US (~ 30 ppbv h^{-1} in spring) (Sklaveniti et al., 2018), and much higher than that measured at the

473   Wakayama Forest Research Station, a remote area of Japan (10.5 ppbv h^{-1} in summer) (Sadanaga et al.,

474   2017) and an urban area of Pennsylvania in the US (~ 8 ppbv h^{-1} in summer) (Cazorla et al., 2010). The

475   result indicates the rationality of the measured $P(O_3)_{net}$ in this study. From previous studies, the O_3

476   pollution in the PRD area is more severe in summer and autumn than in winter and spring (Zhang et al.,

477   2021). In this study, $P(O_3)_{net}$ was measured in wintertime, which was already high, so we believe that the

478   O_3 pollution of the PRD is severe and urgently needs to be controlled. More measurements of $P(O_3)_{net}$

479   worldwide are listed in Table S10, and we found that $P(O_3)_{net}$ was much higher in urban areas than in

480   remote areas using both modeling and direct measurement methods.

481   According to the diurnal variation in all the measured pollutant indicators, $P(O_3)_{net}$ started to

482   increase at approximately 7:00 local time, which may be due to two reasons: (1) the rise in O_3 precursors

483   (i.e., VOCs) due to the high-altitude atmospheric residual layer transported downward near the surface

484   at this time and (2) the increase in solar radiation intensity after 7:00, which increased the oxidation

485   capacity of the pollutants. These two factors jointly enhanced the photochemical oxidation reaction of

486   VOCs and gradually increased $P(O_3)_{net}$. $P(O_3)_{net}$ then peaked at approximately 12:0, which was consistent

487   with $J(NO_2)$, but this peak time was earlier than that of O_3, which peaked at approximately 14:00 , which

488   may be due to the photochemical reactions dominating O_3 mixing ratio changes between 12:00 and 14:00 .

489   After 14:00, the O_3 mixing ratios started to decrease, which may be due to other processes dominating

490   O_3 mixing ratio changes at this time, such as O_3 reacting with other pollutants or surface deposition and

491   the outflow of O_3 by physical transport. In conclusion, changes in O_3 mixing ratios were influenced by

492   both photochemical production and physical transport. Because HO_2 and RO_2 were not well captured in

493   the model, the simulations could lead to an underestimation of $P(O_3)_{net}$.

494   **3.2 Model simulation of $P(O_3)_{net}$ in the reaction and reference chambers**

495   **3.2.1 Modeling method**

496   To obtain a comprehensive understanding of the ozone production rate $P(O_3)$ and ozone destruction rate

497      $D(O_3)$ during the 4-min photochemical reaction in the reaction and reference chambers, we modeled

498      $P(O_3)$ and $D(O_3)$ at 12:00 on 7 December 2021 based on field observation data using a zero-dimensional

499   box model based on the Framework for 0-D Atmospheric Modeling (F0AM) v3.2 coupled with MCM

500   v3.3.1, which contains a total of 143 VOCs, more than 6700 species, involving more than 17000 reactions

501   (Jenkin et al., 2015). $P(O_3)_{net}$ can be expressed by the difference between $P(O_3)$ and $D(O_3)$, and $P(O_3)$

502 and $D(O_3)$ can be expressed as Eq. (9)–(10).

503 $$P(O_3)=k_{HO_2+NO}[HO_2][NO]+\sum_i k_{RO_{2,i}+NO}[RO_{2i}][NO]\varphi_i \tag{9}$$

504 $$D(O_3)=k_{O(^1D)+H_2O}[O(^1D)][H_2O]+k_{OH+O_3}[OH][O_3]+k_{HO_2+O_3}[HO_2][O_3]$$

505 $$+\sum_i\left(k_{O_3+Alkene_i}[O_3][Alkene_i]+k_{OH+NO_2}[OH][NO_2]+k_{RO_{2,i}+NO_2}[RO_{2i}][NO_2]\right) \tag{10}$$

506 where k_{M+N} represents the bimolecular reaction rate constant of M and N, and φ_i is the yield of NO_2 from

507 the reaction RO_{2i} +NO. The relevant reaction rates of $P(O_3)$ and $D(O_3)$ and the VOCs mixing ratios during

508 7–9 December 2021 in SZMGT used in the model are listed in Tables 2 and S11.

509

510 **Table 2. O_3 production and destruction reactions and the relevant reaction rates used in the model.**

Reactions	Rate coefficient / unit	Number
O_3 production pathways - $P(O_3)$		
$RO_2+ NO \rightarrow RO + NO_2$	$2.7\times10^{-12}\times exp(360/T)$ / molecules $^{-1}$ cm^3 s^{-1}	(R1)
$HO_2+ NO \rightarrow OH + NO_2$	$3.45\times10^{-12}\times exp(270/T)$ / molecules $^{-1}$ cm^3 s^{-1}	(R2)
O_3 loss pathways - $D(O_3)$		
$O_3 + hv \rightarrow O^1D + O_2$	Measured JO^1D / s^{-1}	(R3)
$O_3 + C_2H_4 \rightarrow HCHO + CH_2OOA$	$9.1\times10^{-15}\times exp(-2580/T)$ / molecules $^{-1}$ cm^3 s^{-1}	(R4)
$O_3 + C_3H_6 \rightarrow CH_2OOB + CH_3CHO$	$2.75\times10^{-15}\times exp(-1880/T)$ / molecules $^{-1}$ cm^3 s^{-1}	(R5)
$O_3 + C_3H_6 \rightarrow CH_3CHOOA + HCHO$	$2.75\times10^{-15}\times exp(-1880/T)$ / molecules $^{-1}$ cm^3 s^{-1}	(R6)
$O_3 + C_5H_8 \rightarrow CH_2OOE + MACR$	$3.09\times10^{-15}\times exp(-1995/T)$ / molecules $^{-1}$ cm^3 s^{-1}	(R7)
$O_3 + C_5H_8 \rightarrow CH_2OOE + MVK$	$2.06\times10^{-15}\times exp(-1995/T)$ / molecules $^{-1}$ cm^3 s^{-1}	(R8)
$O_3 + C_5H_8 \rightarrow HCHO + MACROOA$	$3.09\times10^{-15}\times exp(-1995/T)$ / molecules $^{-1}$ cm^3 s^{-1}	(R9)
$O_3 + C5H_8 \rightarrow HCHO + MVKOOA$	$2.06\times10^{-15}\times exp(-1995/T)$ / molecules $^{-1}$ cm^3 s^{-1}	(R10)
$O_3+ HO_2 \rightarrow OH$	$2.03\times10^{-16}\times (T/300)^{4.57}\times exp(693/T)$ / molecules $^{-1}$ cm^3 s^{-1}	(R11)
$RO_2+ NO_2 \rightarrow$ peroxy nitrates	$(3.28\times10^{-28}\times7.24\times10^{18}\times P/T\times(T/300)^{-6.87}\times1.125 \times10^{-11}\times(T/300)^{-1.105})\times10^{(log10(0.30)}/(1+(log10(2.93 \times10^{-17}\times7.24\times10^{18}\times P/T\times(T/300)^{-5.765})/0.75-1.27 \times log10(0.30))^2))/(2.926\times10^{-17}\times7.24\times10^{18}\times P/T \times(T/300)^{-5.765})$ / molecules $^{-1}$ cm^3 s^{-1}	(R12)
$NO_2+ OH \rightarrow HNO_3$	$3.2\times10^{-30}\times7.24\times10^{18}\times P/T\times(T/300)^{-4.5}\times3\times10^{-11} \times10^{log10(0.41)}/(1+(log10(3.2\times10^{-30}\times7.24\times10^{18}\times P/T \times(T/300)^{-4.5}/3\times10^{-11})/(0.75-1.27 \times(log10(0.41))^2)/(3.2\times10^{-30}\times7.24\times10^{18}\times P/T \times(T/300)^{-4.5}+3\times10^{-11})$ / molecules $^{-1}$ cm^3 s^{-1}	(R13)
$O_3+ OH \rightarrow HO_2$	$1.70\times10^{-12}\times exp(-940/T)$ / molecules $^{-1}$ cm^3 s^{-1}	(R14)

511 *The rate coefficient obtained from the MCM v3.3.1 model.

512   In total, three-stage simulations were carried out to obtain the 4-min photochemical reactions in

513   the reaction and reference chambers, and all three-stage models were operated in a time-dependent mode

514   with a 1 s resolution. In the 1st-stage, to establish a real atmospheric environment system, all observations

515   on 7 December 2021, 6:00-11:30, were used to constrain the model to obtain the mixing ratios of the

516   unmeasured species in the ambient atmosphere, including oxygenated VOCs (OVOCs, in total 16

517   species), non-methane hydrocarbons (in total 47 species), O_3, NO, NO_2, J values, T, RH, and pressure

518   (P). Because O_3-NO-NO_2 was not in a steady state when all species were constrained, we conducted a

519   2nd-stage simulation during 11:30–12:00. In this stage, we used the output mixing ratios of the

520   unmeasured species from the simulation in the last 1 s of the 1st-stage simulation as the input, which were

521   not constrained after providing initial values. For the measured species, O_3, NO, and NO_2 were no longer

522   constrained after providing initial values, while all other variables (including NO_X, VOCs, J values, RH,

523   T, P, etc.) were still constrained in a time-dependent mode with a 1 s resolution after providing initial

524   values. In the 3rd-stage, we modeled the 4-min photochemical reactions in the reaction and reference

525   chambers. We used the output mixing ratios of the unmeasured species (i.e., OH, HO_2, RO_2, SO_2, HONO,

526   etc.) from the simulation in the last 1 s of the 2nd-stage simulation and all measured values (i.e., O_3, NO,

527   NO_2, VOCs, J values, RH, T, P, etc.) as the model input, which were not constrained after providing

528   initial values. In addition, while maintaining the setup conditions for the 2nd-stage of the simulation, we

529   extended the simulation of the environment to 12:04 to obtain the modeled $P(O_3)_{net}$ in the environment

530   in the 3rd-stage simulation. The result is shown in orange marker in Fig. 10d. Figure 7 is an explicit

531   explanation of the 3rd-stage simulation in the reaction and reference chambers.
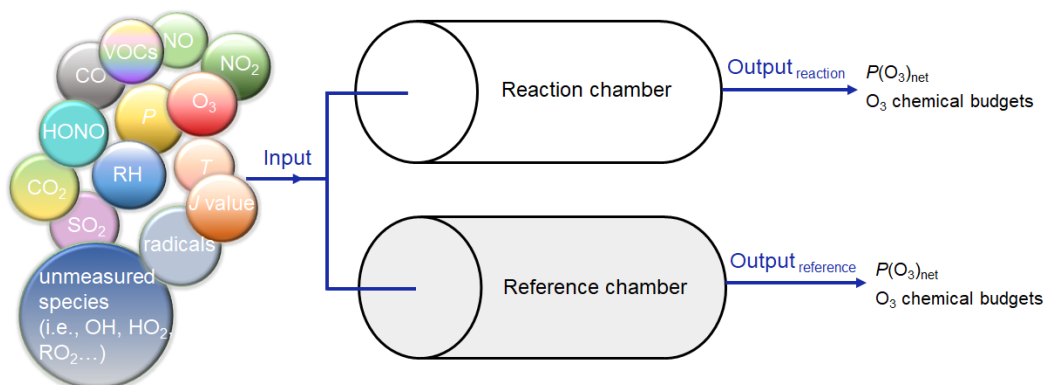
532

533   **Figure 7: Explicit explanation of the 3rd-stage model simulation (input meteorological conditions: P: 1015.3**
534   **hPa, T: 295.6 K, RH: 39.7 %).**

535   Specifically, because the photolysis frequencies play critical roles in the simulation of $P(O_3)_{net}$, the

536   J values obtained from two methods (labeled method I and method II) were used in the 3rd-stage 4-min

537   simulation. The J values used in method I were obtained from the measured values (including $J(NO_2)$,

538    $J(O^1D)$, $J(HONO)$, $J(H_2O_2)$, $J(NO_3\_M)$, $J(NO_3\_R)$, $J(HCHO\_M)$, and $J(HCHO\_R)$) and the simulated values

539   using the Tropospheric Ultraviolet and Visible (TUV) radiation model (version 5.3) (including $J(HNO_3)$,

540    $J(CH_3CHO)$, $J(MACR)$, $J(MEK)$, $J(HOCH_2CHO)$, $J(C_2H_5CHO)$, $J(C_3H_7CHO)$, and $J(C_4H_9CHO)$).), while the J

541   values in method II were all obtained from the simulated values using the TUV model, detailed

542   information on these two methods is introduced in Appendix IV (Tables S12 and S13).

3.2.2 Radical chemistry in the reaction and reference chambers

544   The variations in the radical mixing ratios (i.e., HO_2, OH, RO_2) and NO_3, NO, NO_2, and O_3 mixing

545   ratios obtained from method I and method II during the 3rd-stage 4-min model simulation are shown in

546   Fig. 8 and Fig. S18, respectively. The production and destruction reactions of HO_2, OH, RO_2, and NO_3

547   in the reaction and reference chambers obtained from methods I and II are shown in Fig. 9 and Fig. S19,

548   respectively, the production and destruction reactions of RO_X in the reaction and reference chambers

549   obtained from methods I and II are shown in Fig. S20, the detailed ROx production pathways of

550   NO_3+VOCs are shown in Fig. S21, and the final modeling results are shown in Fig. 10 and Fig. S22.

551   From Fig. 8, in the reaction chamber, the HO_2, OH, RO_2, and NO_3 concentrations first slightly

552   increased and then became stable, and their final concentrations were 2.00×10^8, 7.64×10^6, 1.08×10^8, and

553   8.47×10^6 molecules cm^{-3}, respectively. In the reference chamber, the HO_2 and RO_2 concentrations

554   dropped during the 1st half minute and rose afterward. The final HO_2 concentration (1.35×10^8 molecules

555   cm^{-3}) was lower than that in the reaction chamber, while the RO_2 concentration exceeded that in the

556   reaction chamber at the end of the 2nd minute and gradually became stable at 1.27×10^8 molecules cm^{-3}.

557   The OH concentration dropped significantly at the 1st minute and then became stable at approximately

558   6.16×10^5 molecules cm^{-3}. The NO_3 concentration rose significantly during the 4-min simulation and

559   reached 3.55×10^7 molecules cm^{-3} at the end, which was much higher than that in the reaction chamber.
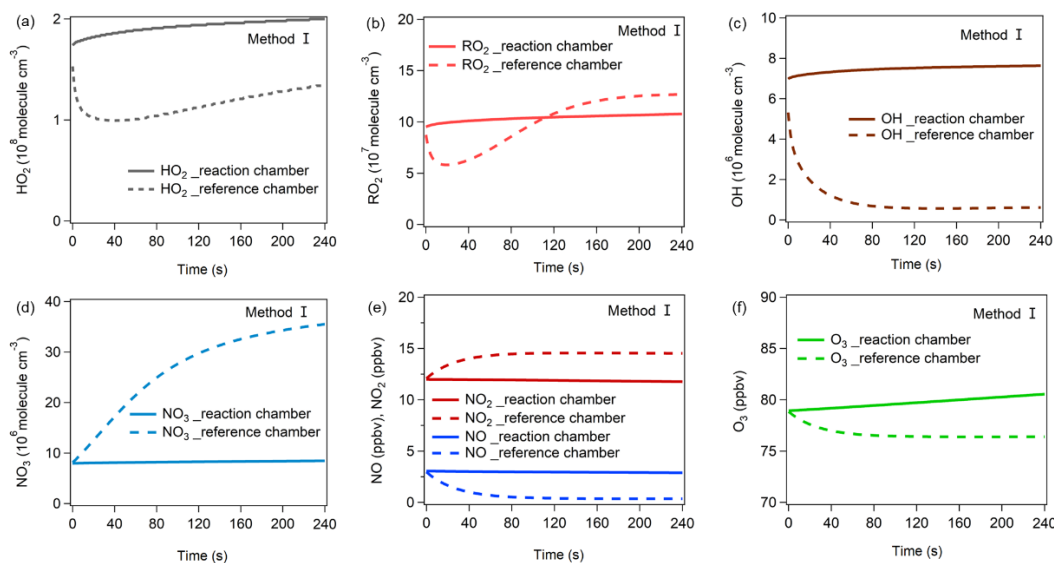
Figure 8: The variations of (a)HO$_2$, (b) RO$_2$, (c) OH, (d)NO$_3$, (e) NO, NO$_2$, and (f) O$_3$ mixing ratios during the 3rd-stage 4-min model simulation using method I. The mixing ratios changes of these items for method II is shown in Fig. S18.

OH, HO$_2$, RO$_2$, and NO$_3$ concentrations greatly impact the O$_3$ production and destruction rate. To better understand the factors that drive the OH, HO$_2$, RO$_2$, and NO$_3$ concentration changes, we have added their production and destruction pathways in Fig. 9. We found that the decrease in HO$_2$ and RO$_2$ concentrations in the reference chamber in the 1st half minute was mainly due to NO titration effects, as high NO mixing ratios existed during the 1st half minute. The increase in HO$_2$ concentrations afterward was largely attributable to RO+O$_2$ reaction/RO decomposition, OH+CO/VOCs reaction, OVOCs photolysis (i.e., C$_3$H$_4$O$_2$, C$_2$H$_2$O$_2$, C$_4$H$_6$O$_2$), and NO$_3$+VOCs reaction, and the increase in RO$_2$ concentrations afterward were largely attributable to OH+VOCs oxidation, OVOCs photolysis and O$_3$+VOCs reaction. The main OH sources in the reference chamber were both HO$_2$+NO in method I and method II. Due to sufficiently high J(NO$_3$) (~ 90% of that in the reaction chamber) and NO$_2$ concentrations in the reference chamber, the NO$_3$ photolysis and NO$_2$+NO$_3$ reaction consumed NO$_3$ in the reference chamber, but the NO$_3$ concentrations were still sufficiently high due to high production rates of NO$_3$ at the same time. The main NO$_3$ source in the reference chamber was the NO$_2$+O$_3$ reaction, followed by N$_2$O$_5$ decomposition. The NO concentrations were relatively high in the 1st minute and consumed NO$_3$ very quickly, but due to continuous NO$_3$ sources, the net NO$_3$ production rates (P(NO$_3$)$_{net}$) were positive (as shown in Fig. 9), which caused the NO$_3$ concentration to continue to increase (as shown in Fig. 8d). The main difference in NO$_3$ production in the reference chamber compared to that in the

581 reaction chamber was the much higher N_2O_5 decomposition, which was mainly due to the high NO_2

582 concentrations in the reference chamber. On the other hand, although the $NO+NO_3$ reaction was also one

583 of the dominant NO_3 destruction pathways, NO_3 consumed by the $NO+NO_3$ reaction was significantly

584 smaller than NO_3 produced by the NO_2+O_3 reaction. Furthermore, in order to check if the NO_3+VOCs

585 reactions exists, we extracted all the P(ROx) pathways related to NO_3+VOCs reactions during the 3rd-

586 stage 4-min model simulation in the reaction and reference chambers in method I, as shown in Fig. S20.

587 We found that the NO_3+VOCs reactions are mostly related to the OVOCs (i.e. 6-Ethyl-m-cresol and 3-

588 Ethyl-6-methylbenzene-1,2-diol) in Fig. S21. The production and destruction rates of ROx are shown in

589 Fig. S20.

590
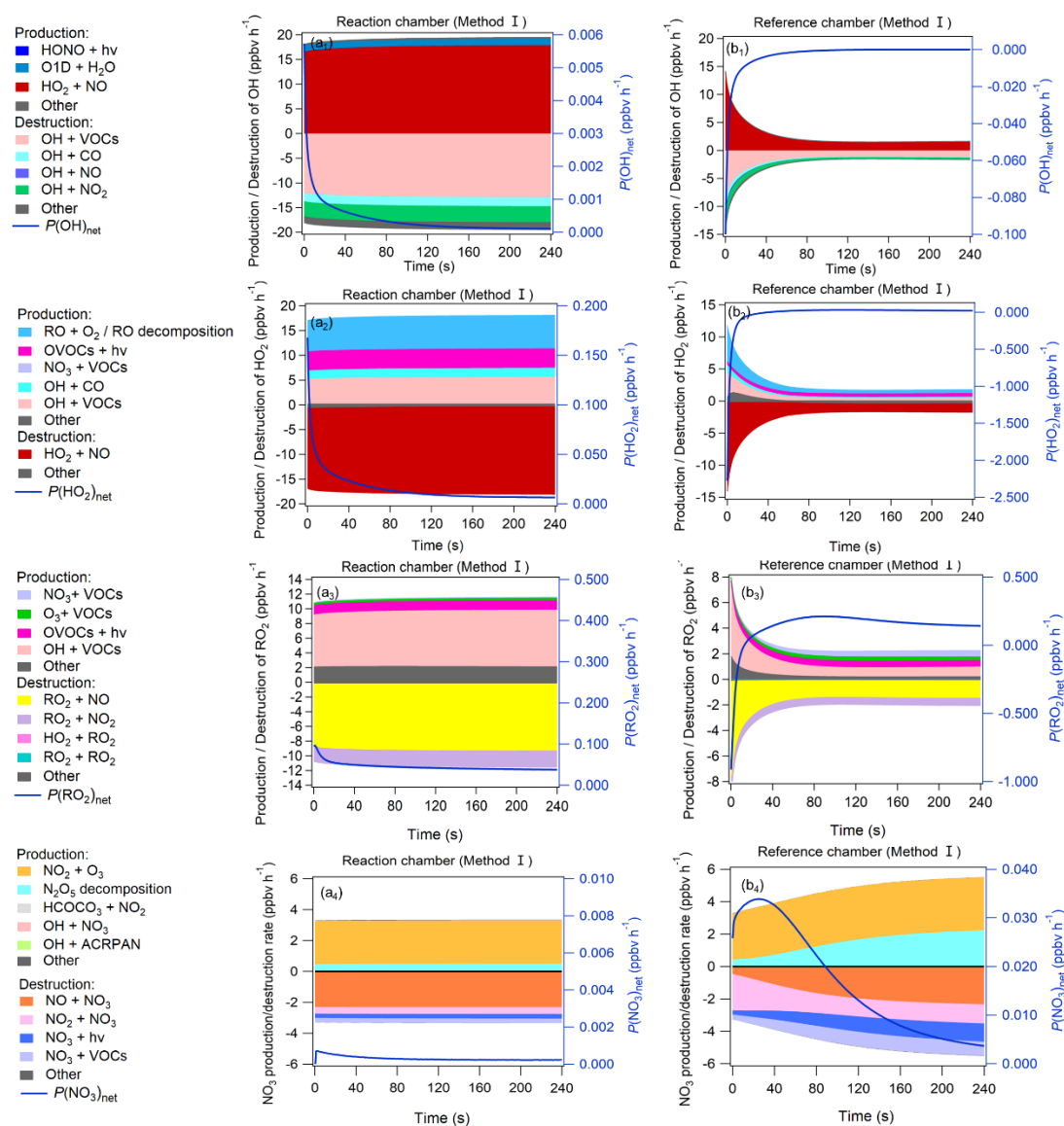
591
592 **Figure 9: Production and destruction pathways of OH (a_1-b_1), HO$_2$ (a_2-b_2), RO$_2$ (a_3-b_3), and NO$_3$ (a_4-b_4) during**

the 3rd-stage 4-min model simulation in the reaction and reference chambers in method I. The related contents for method II (c)-(d) are shown in Fig. S19 in the supplementary materials.

3.2.3 $P(O_3)_{net}$ formation and destruction pathways in the reaction and reference chambers

Figures 10a–d show the modeled $P(O_3)_{net}$ and the sources and sinks of various species during the 3rd-stage 4-min simulation. Figure 10a shows the steady state of $P(O_3)_{net}$ and the various species in the ambient atmosphere achieved in the last 1 s of the 2nd-stage simulation; Figures 10b and c show the modeled $P(O_3)_{net}$ and the O_3 chemical budgets in the reaction and reference chambers during the model simulation period; Figure 10d summarizes the modeled $P(O_3)_{net}$ in the ambient air (represented as blue and orange markers at the time when the ambient air was going in and out of the NPOPR system, respectively) and the modeled $P(O_3)_{net}$ in the reaction and reference chambers. To compare the modeled results with our measured results, we calculated the integral mean of the modeled $P(O_3)_{net}$ in the reaction and reference chambers and appended the related measured $P(O_3)_{net}$ value during the 4-min simulation time onto Fig. 10d (green maker). Furthermore, the reaction weights of different production and destruction reaction processes of O_3 are shown in Figs. 10e–h.
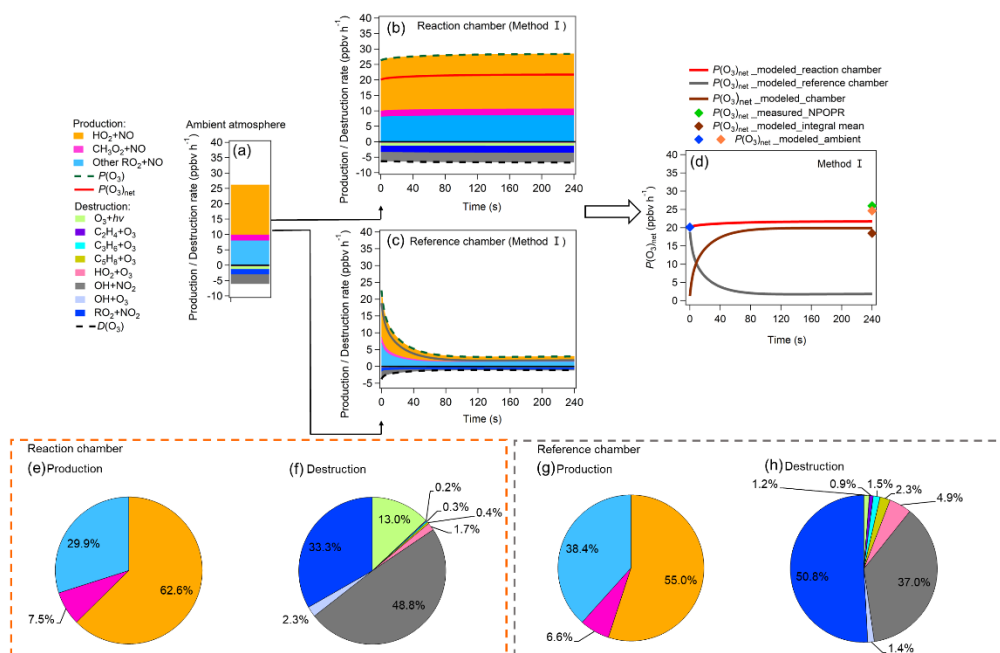
Figure 10: (a)–(c) show the modeled $P(O_3)_{net}$ and the O_3 chemical budgets in (a) the ambient atmosphere when injected into the reaction and reference chambers and (b–c) the reaction and reference chambers during the 4-min model simulation; (d) shows $P(O_3)_{net}$, where $P(O_3)_{net}$_modeled_ambient represent the modeled $P(O_3)_{net}$ in the ambient air at the time before (blue marker) and after (orange marker) the sampled ambient air was injected into the dual-channel reaction chamber. $P(O_3)_{net}$_modeled_reaction chamber and $P(O_3)_{net}$_modeled_reference chamber represent the $P(O_3)_{net}$ changing trend during the 4-min photochemical reactions in the reaction and reference chambers, respectively, $P(O_3)_{net}$_modeled_chamber =

$P(O_3)_{net}$_modeled_reaction chamber–$P(O_3)_{net}$_modeled_reference chamber, $P(O_3)_{net}$_modeled_integral mean represents the integral mean of the $P(O_3)_{net}$_modeled_chamber, and $P(O_3)_{net}$_measured_NPOPR represent the measured $P(O_3)_{net}$ by NPOPR detection system. (e)–(h) show the reaction weights of each production and destruction reactions process of O_3 in the reaction and reference chambers in method I.

Figure 10a-h shows the contribution of different reaction pathways to $P(O_3)$ and $D(O_3)$. $P(O_3)$ and $D(O_3)$ were almost the same within the 4-min reaction in the reaction chamber (all species reached a steady-state condition), while $P(O_3)$ and $D(O_3)$ in the reference chamber decreased significantly within the 1st min and remained stable in the following minutes. In the reaction chamber, the HO_2+NO reaction contributed most to $P(O_3)$, accounting for 62.6 % of the total $P(O_3)$, with an integral mean value of 17.5 ppbv h^{-1} in the reaction chamber. The second important pathway of $P(O_3)$ was RO_2+NO (accounting for 37.4 % of the total $P(O_3)$). The reaction of RO_2+NO core presents more than approximately 1200 types of RO_2 radicals, and the pathway of CH_3O_2+NO contributed 7.5 % of the total $P(O_3)$. The most important contributor of $D(O_3)$ was $OH+NO_2$ (48.8 %), followed by RO_2+NO_2 (33.3 %), O_3 photolysis (13.0 %), O_3+OH (2.3 %), O_3+HO_2 (1.7 %), $C_5H_8+O_3$ (0.4 %), $C_3H_6+O_3$ (0.3 %), and $C_2H_4+O_3$ (0.2 %). In the reference chamber, the integral mean value of the HO_2+NO reaction was 2.3 ppbv h^{-1}, which had the largest contribution to $P(O_3)$ (accounting for 55.0 %). The second largest contributor of $P(O_3)$ was RO_2+NO (accounting for 45.0 % of the total $P(O_3)$), in which the pathway of CH_3O_2+NO contributed 6.6 % of the total $P(O_3)$. The most important contributor of $D(O_3)$ was RO_2+NO_2 (50.8 %), followed by $OH+NO_2$ (37.0 %), O_3+HO_2 (4.9 %), $C_5H_8+O_3$ (2.3 %), $C_3H_6+O_3$ (1.5 %), O_3+OH (1.4 %), O_3 photolysis (1.2 %), and $C_2H_4+O_3$ (0.9 %). For all $P(O_3)$ reactions, the weight of the RO_2+NO reaction in the reference chamber was 7.5 % higher than that in the reaction chamber; however, for all $D(O_3)$ reactions, the weight of the RO_2+NO_2 reaction in the reference chamber was 17.5 % higher than that in the reaction chamber, which mitigates the high $P(O_3)$ caused by RO_2+NO in the reference chamber. Furthermore, the weight of the $OH+NO_2$ reaction in the reference chamber was 11.9 % lower than that in the reaction chamber, which may be the main reason that led to NO_2 mixing ratios in the reference chamber being much higher than those in the reaction chamber. It is worth noting that the different reaction pathways of $P(O_3)$ and $D(O_3)$ stabilized at approximately 1.5 min for both methods I and II (as shown in Figs. 10 and S22), and the radicals that play critical roles in photochemical O_3 formation, such as HO_2, RO_2 and OH, reached quasi-steady states in approximately 3 min (as shown in Figs. 8 and S18). As the lowest experimental residence time in the reaction and reference chambers was 3.8 min at an air flow rate of 5 L min^{-1}, the photochemical reaction time at different air flow rates in the NPOPR system is sufficient for

646   investigating $P(O_3)_{net}$, and it is reasonable for us to set the alternate ambient air sampling time for the

647   reaction and reference chambers at 2 min, where the ambient air actually has already reacted for at least

648   3.8 min in the chambers.

649   The $P(O_3)_{net}$ value measured by the NPOPR detection system at 12:04 was 26.0 ppbv h^{-1}, which

650   was 1.4 ppbv h^{-1} higher than the modeled $P(O_3)_{net}$ value in the ambient air (orange marker in Fig. 10d,

651   24.6 ppbv h^{-1}) and 7.5 ppbv h^{-1} higher than the modeled $P(O_3)_{net}$ value of the NPOPR system (brown

652   marker in Fig. 10d, 18.5 ppbv h^{-1}, calculated from the integral mean of the 3rd-stage 4-min modeled

653    $P(O_3)_{net}$ in the reaction and reference chambers). Here, we note that for a better comparison between the

654   measured and modeled $P(O_3)_{net}$ values, the measured $P(O_3)_{net}$ used here was obtained from a 4-min time

655   resolution, which is 1.4 ppbv h^{-1} higher than the measured $P(O_3)_{net}$ value used in Fig. 6 (1-h time

656   resolution). The ratio of measured and modeled $P(O_3)_{net}$ values was 1.4, which is consistent with the

657   measured-to-modeled ratio of the cumulative $P(O_3)_{net}$ (1.3 and 1.4) obtained from previous studies

658   (Cazorla et al., 2012; Ren et al., 2013), where $P(O_3)_{net}$ values were also measured directly in the

659   atmosphere and were independent of the OH and HO$_2$ measurements. The reason for the difference

660   between the measured and modeled $P(O_3)_{net}$ here may be due to the inaccurate estimation of HO$_2$/RO$_2$

661   radicals; for example, Ren et al. (2013) found that $P(O_3)$ calculated from the modeled HO$_2$ was lower

662   than that calculated from the measured HO$_2$. The unknown HO$_2$ source should be identified for a more

663   accurate estimation of $P(O_3)_{net}$ in future studies.

664   Additionally, the modeled $P(O_3)_{net}$ using the J values obtained from method II was 9.3 ppbv h^{-1}

665   lower than the measured $P(O_3)_{net}$, and this discrepancy was slightly larger than that using method I, as

666   shown in Appendix IV (Fig. S22). The differences in the measured and modeled $P(O_3)_{net}$ by method I

667   and method II were 28.8 % and 35.8 %, respectively. This difference was mainly due to the transmittance

668   of $J(NO_2)$ in method II (30 %) being much higher than that in method I (9 %), and NO$_2$ photolysis

669   products were involved in the main reaction of O$_3$ production of HO$_2$+NO and RO$_2$+NO, so the modeled

670    $P(O_3)_{net}$ in the reference chamber was slightly overestimated in method II, thus leading to an

671   underestimation of the final $P(O_3)_{net}$.

672   Furthermore, because the NO$_2$ data used here were measured by a commercially available

673   chemiluminescence NOx monitor, the NO$_2$ and NOx mixing ratios would be overestimated due to NOz

674   interference (i.e., HNO$_3$, PANs, HONO, etc.) (Dunlea et al., 2007). According to our test, the

675   chemiluminescence technique could bias NO_2 by 5 % compared to the CAPS technique, which is

676   regarded as a trustworthy NO_2 measurement technique without chemical interference. Therefore, we

677   simulated the interference of NO_2 measured by a chemiluminescence NOx monitor in method I as follows:

678   reducing and increasing the ambient NO_2 mixing ratios by 5 % in the 3rd-stage 4-min simulation in the

679   reaction and reference chambers. The results show that increasing and decreasing NO_2 by 5 % resulted

680   in a decrease in $P(O_3)_{net}$ by 1.64 % and 3.68 %, respectively (as shown in Fig. S23), which is much

681   smaller than the bias caused by $P(O_3)_{net}$ in the reference chambers (which were 13.9 % and 22.3 % for

682   method I and method II, respectively). To evaluate $P(O_3)_{net}$ error caused by the measurement error of J

683   values, we introduced a ±5 % error to the measured J values during the 3rd stage of the 4-min simulation

684   in method I. The modeled $P(O_3)_{net}$ results are presented in Fig. S24 in the supplementary materials. We

685   observed that the inclusion of a -5 % measurement error in J values led to a decrease in $P(O_3)_{net}$ by

686   7.27 %, while adding a +5 % measurement error in J values caused an increase in $P(O_3)_{net}$ by 3.08 %.

687   This implies that the maximum bias of $P(O_3)_{net}$ caused by the measurement error of J values falls within

688   the error range of the currently assessed $P(O_3)_{net}$ error, which was 13.9 % for method I. Therefore, we

689   conclude that this type of error will not influence our final modeling results and conclusions.

690   In conclusion, modeling tests demonstrated that the radicals and gas species in the reaction

691   chamber of the NPOPR detection system were similar to those in genuine ambient air, while these

692   radicals also unexpectedly existed in the reference chamber. This was mainly because the UV protection

693   film used by the reference chamber did not completely filter out sunlight, which led to the low

694   transmittance of light ranging from 390 nm to 790 nm. The $P(O_3)_{net}$ biases caused by this interference

695   modeled in method I and method II were 13.9 % and 22.3 %, respectively, which ensured that the

696   measured $P(O_3)_{net}$ by the NPOPR detection system should be regarded as the lower limit values of real

697   $P(O_3)_{net}$ in the atmosphere. We recommend that the J values obtained from method I should be used in

698   the model simulation, which can better explain the photochemical formation of O_3 in the actual

699   atmosphere, but if direct J value measurements cannot be achieved during field observations, the J values

700   obtained from method II would also be acceptable in modeling studies.

701   **4 Conclusions**

702   We modified and improved a net photochemical ozone production rate (NPOPR) detection system based

703 on a dual-channel reaction chamber technique, which provides more accurate results and has broader

704 application potential compared to previous studies. The main improvements of NPOPR detection system

705 compared to previous studies were as follows: (1) improved the design of the reaction and reference

706 chambers to make sure they have good airtightness; (2) changed the air sampling structure to enable the

707 total air flow rates change freely from 1.3 to 5 L min^{-1} in the reaction and reference chambers, which can

708 make the NPOPR system achieve different limits of detection (LODs) and appliable to different ambient

709 environment; (3) characterized the NPOPR detection system at different air flow rates to optimize the

710 $P(O_3)_{net}$ measurements, the LODs of the NPOPR detection system are 0.07, 1.4, and 2.3 ppbv h^{-1} at air

711 flow rates of 1.3, 3, and 5 L min^{-1}, respectively; (4) tested the performance of both reaction and reference

712 chambers by combining the field measurement and the MCM modeling method.

713 The NPOPR detection system was employed in the field observation at the Shenzhen

714 Meteorological Gradient Tower (SZMGT), which is located in PRD, China. During the measurement

715 period, the $P(O_3)_{net}$ was around zero during nighttime and ranged from ~ 0 to 34.1±7.8 ppbv h^{-1} during

716 daytime (from 6:00–18:00), with the average value of 12.8 (±5.5) ppbv h^{-1}. Besides, $P(O_3)_{net}$ start to

717 increase at around 7:00 at local time, this may be due to the rise of the O_3 precursors (i.e., VOCs)

718 transported down from the high-altitude atmospheric residual layer to the near-surface and the increase

719 of solar radiation intensity increased the atmospheric oxidation capacity. $P(O_3)_{net}$ was then reaches a peak

720 at around 12:00 at noon time, by coupling with diurnal O_3 mixing ratios trends, we confirmed that the

721 ground-level O_3 mixing ratios were influenced by both photochemical production and physical transport.

722 In order to clarify the detailed photochemical reaction processes in the reaction and reference

723 chambers of NPOPR system, we modeled the $P(O_3)_{net}$ on 7 December 2021, 12:00-12:04 in the reaction

724 and reference chambers using MCM v3.3.1. As the photolysis frequencies of different species (J values)

725 play critical roles in the formation of $P(O_3)_{net}$, the J values obtained from two methods were used in the

726 4-min chamber photochemical reaction (labeled as method I and method II), in method I , eight main J

727 values (e.g., $J(NO_2)$, $J(O^1D)$, $J(HONO)$, etc.) were measured directly, and other J values were obtained

728 from the simulated values using the Tropospheric Ultraviolet and Visible (TUV) radiation model, while

729 in method II, J values were all obtained from the simulated values using TUV model (as described in

730 Sect. 3.2). Modeling tests demonstrated that the mixing ratios of different radicals and gas species (i.e.,

731 OH, HO_2, RO_2, NO_3, NO, NO_2, and O_3) in the reaction chamber were similar with those in the real

ambient environment, while due to the UV protection film used by the reference chamber does not completely filter out the sunlight, there was low transmittance of the light ranged from 390 nm to 790 nm. In the reaction chamber, the contribution of different reactions to $P(O_3)$ and $D(O_3)$ modeled by method I and II were quite similar, where the HO_2+NO reaction contributed most to $P(O_3)$ (~ 62.6 %), followed by the RO_2+NO reaction (~ 37.4 %). The $OH+NO_2$ reaction contributed most to $D(O_3)$, which accounted for ~ 48.9 %, followed by the RO_2+NO_2 reaction O_3 photolysis, which accounted for ~ 33.3 % and 13.0 %, respectively. In the reference chamber, the contribution of different reactions to $P(O_3)$ and $D(O_3)$ modeled by method I and II were different, where the HO_2+NO reaction contributed ~ 55.0 % and ~ 58.2 % to the total $P(O_3)$, respectively, and RO_2+NO contributed ~ 44.9 % and 41.8 % to the total $P(O_3)$, respectively. The most important contributor of $D(O_3)$ modeled by method I was RO_2+NO_2 (50.8 %), followed by $OH+NO_2$ (37.0 %), while the most important contributor of $D(O_3)$ modeled by method II was $OH+NO_2$ (46.8 %), followed by RO_2+NO_2 (44.1 %). For all $P(O_3)$ reactions, the weight of RO_2+NO reaction in the reference chamber was 7.5 % and 4.3 % higher than that in the reaction chamber in method I and II, respectively, however, for all $D(O_3)$ reactions, the weight of RO_2+NO_2 reaction in the reference chamber was 17.5 % and 10.9 % higher than that in the reaction chamber in method I and II, respectively, which will somehow mitigate the high $P(O_3)$ caused by RO_2+NO in the reference chamber. The different reaction pathways of $P(O_3)$ and $D(O_3)$ had stabilized at around 1.5 min, and the radicals that play critical roles in photochemical O_3 formation, such as HO_2, RO_2 and OH, reached quasi-steady states in about 3 min, the long enough ambient air residence time in the reaction and reference chambers ($\geq$ 3.8 min) make the photochemical reaction time at different air flow rates in the NPOPR system sufficient enough for investigating the $P(O_3)_{net}$, and it is reasonable for us to set the alternate ambient air sampling time for the reaction and reference chambers at 2 min, where the ambient air actually has already reacted for at least 3.8 min in the chambers.

The biases of the modeled $P(O_3)_{net}$ caused by the interference of the reactions in the reference chamber in method I and method II were 13.9 % and 22.3 %, respectively; thus, the measured $P(O_3)_{net}$ by the NPOPR detection system should be regarded as the lower limit values of the real $P(O_3)_{net}$ in the atmosphere. Nevertheless, the measured $P(O_3)_{net}$ values were 7.5 and 9.3 ppbv h^{-1} higher than the modeled $P(O_3)_{net}$ values obtained from methods I and II, respectively, which may be due to the inaccurate modeling of HO_2/RO_2 radicals. Short-lived intermediate measurements coupled with direct $P(O_3)_{net}$

measurements are needed in future study in order to studies to better understand the photochemical production and destruction mechanisms of O_3. We recommend that the J values obtained from method I should be used in the model simulation, which can better explain the photochemical formation of O_3 in the actual atmosphere, but if direct J value measurements cannot be achieved during field observations, the J values obtained from method II would also be acceptable in modeling studies.

The self-built NPOPR detection system in this study filled the gap in the observation method in China. The research results not only help us to understand the tropospheric O_3 budget but also provide an important data basis for formulating correct O_3 pollution prevention measures and control strategies.

Data availability. The observational data used in this study are available from corresponding authors upon request (junzhou@jnu.edu.cn).

Author contributions. JZ, BY, and MS designed the experiment, YXH and JZ developed and assembled the NPOPR detection system, YXH, JZ, JPZ, BY, YW, YFW, SCY, YWP, JPQ, XJH, XS and YBC collected and analyzed the data YXH and JZ wrote the manuscript, all authors revised the manuscript.

Competing interests. The authors declare that they have no known competing interests.

Acknowledgements. This study was funded by the Key-Area Research and Development Program of Guangdong Province (grant no. 2020B1111360003), and the Natural Science Foundation of Guangdong Province (grant no. 2020A1515110526). We thank Nan Ma and Xiaofeng Su for the HONO production experiment.

References

Avnery, S., Mauzerall, D. L., Liu, J., and Horowitz, L. W.: Global crop yield reductions due to surface ozone exposure: 1. Year 2000 crop production losses and economic damage, Atmos. Environ., 45, 2284-2296, https://doi.org/10.1016/j.atmosenv.2010.11.045, 2011.

Baier, B. C., Brune, W. H., Lefer, B. L., Miller, D. O., and Martins, D. K.: Direct ozone production rate measurements and their use in assessing ozone source and receptor regions for Houston in 2013, Atmos. Environ., 114, 83-91, http://dx.doi.org/10.1016/j.atmosenv.2015.05.033, 2015.

Baier B C, Brune W H, Miller D O, et al., Higher measured than modeled ozone production at increased NOx levels in the Colorado Front Range, Atmos. Chem. Phys., 17: 11273–11292,

789   https://doi.org/10.5194/acp-17-11273-2017, 2017.

790   Bell, M. L., McDermott, A., Zeger, S. L., Samet, J. M., and Dominici, F.: Ozone and short-term mortality

791   in 95 US urban communities, J. Am. Med. Assoc. 1987-2000., 292, 2372-

792   2378, https://doi.org/10.1001/jama.292.19.2372, 2004.

793   Berman, J. D., Fann, N., Hollingsworth, J. W., Pinkerton, K. E., Rom, W. N., Szema, A. M., Breysse, P.

794   N., White, R. H., and Curriero, F. C.: Health benefits from large-scale ozone reduction in the United

795   States, Environ. Health. Persp., 120, 1404-10, https://doi.org/10.1289/ehp.1104851, 2012.

796   Bohn B, Lohse I. Calibration and evaluation of CCD spectroradiometers for ground-based and airborne

797   measurements of spectral actinic flux densities. Atmos. Meas. Tech., 10, 3151–3174,

798   https://doi.org/10.5194/amt-10-3151-2017, 2017.

799   Burkholder, J., Sander, S., Abbatt, J., Barker, J., Cappa, C., Crounse, J., Dibble, T., Huie, R., Kolb, C.,

800   and Kurylo, M.: Chemical kinetics and photochemical data for use in atmospheric studies, evaluation

801   number 19, Pasadena, CA: Jet Propulsion Laboratory, National Aeronautics and

802   Space Administration, 2020, http://jpldataeval.jpl.nasa.gov. 2020.

803   Cazorla, M., Brune, and W. H.: Measurement of ozone production sensor, Atmos. Meas. Tech., 3, 545-

804   555, https://doi.org/10.5194/amt-3-545-2010, 2010.

805   Cazorla, M., Brune, W. H., Ren, X., and Lefer, B.: Direct measurement of ozone production rates in

806   Houston in 2009 and comparison with two estimation methods, Atmos. Chem. Phys., 12, 1203-1212,

807   https://doi.org/10.5194/acp-12-1203-2012, 2012.

808   Dunlea, E. J., Herndon, S. C., Nelson, D. D., Volkamer, R. M., Martini, F. S., Sheehy, P. M., Zahniser,

809   M. S., Shorter, H., Wormhoudt, J. C., Lamb, B. K., Allwine, E. J., Gaffney, J. S., Marley, N. A., Grutter,

810   M., Marquez, C., Blanco, S., Cardenas, B., Retama, A., Villegas, C. R. R., Kolb, C. E., Molina, L. T.,

811   and Molina, M. J.: Evaluation of nitrogen dioxide chemiluminescence monitors in a polluted urban

812   environment, Atmos. Chem. Phys., 7, 2691–2704, https://doi.org/10.5194/acp-7-2691-2007, 2007.

813   Jenkin, M. E., Young, J. C., and Rickard, A. R.: The MCM v3.3.1 degradation scheme for isoprene,

814   Atmos. Chem. Phys., 15, 11433-11459, https://doi.org/10.5194/acp-15-11433-2015, 2015.

815   Kanaya, Y., Tanimoto, H., Yokouchi, Y., Fumikazu Taketani, F. T., Komazaki, Y., Irie, H., Takashima, H.,

816   Pan, X., Nozoe, S., and Inomata, S.: Diagnosis of photochemical ozone production rates and limiting

817   factors in continental outflow air masses reaching Fukue Island, Japan: ozone-control implications,

818   Aerosol. Air. Qual. Res., 16, 430-441, https://doi.org/10.4209/aaqr.2015.04.0220, 2016.

819   Karakatsani, A., Kapitsimadis, F., Pipikou, M., Chalbot, M. C., Kavouras, I. G., Orphanidou, D., Papiris,

820   S., and Katsouyanni, K.: Ambient air pollution and respiratory health effects in mail carriers, Environ.

821   Res., 110, 278-85, https://doi.org/10.1016/j.envres.2009.11.002, 2010.

822   Lee, S.-B., Bae, G.-N., Lee, Y.-M., Moon, K.-C., and Choi, M.: Correlation between light intensity and

823   ozone formation for photochemical smog in urban air of seoul, Aerosol. Air. Qual. Res., 10, 540-549,

824   https://doi.org/10.4209/aaqr.2010.05.0036, 2010.

825   Liu, S. C.: Possible effects on fropospheric O3 and OH due to NO emissions, Geophys. Res. Lett., 4,

826   325-328, https://doi.org/10.1029/GL004i008p00325, 1977.

827   Liu, X., Wang, N., Lyu, X., Zeren, Y., Jiang, F., Wang, X., Zou, S., Ling, Z., and Guo, H.: Photochemistry

828   of ozone pollution in autumn in Pearl River Estuary, South China, Sci. Total Environ., 754, 141812,

829   https://doi.org/10.1016/j.scitotenv.2020.141812, 2020.

830   Luecken, D. J., Phillips, S., Sarwar, and G., Jang, C.: Effects of using the CB05 vs. SAPRC99 vs. CB4

831   chemical mechanism on model predictions: Ozone and gas-phase photochemical precursor

832   concentrations, Atmos. Environ., 42, 5805-5820, https://doi.org/10.1016/j.atmosenv.2007.08.056,

833   2008.

834   Lu, K., Zhang, Y., Su, H., Brauers, T., Chou, C. C., Hofzumahaus, A., Liu, S. C., Kita, K., Kondo, Y,

835   Shao, M., Wahner, A., Wang, J., Wang, X., and Zhu, T.: Oxidant (O3+ NO2) production processes and

836   formation   regimes   in   Beijing,   J.   Geophys.   Res.   Atmos.,   115,   D07303,

837   https://doi.org/10.1029/2009JD012714, 2010.

838   Malley, C. S., Henze, D. K., Kuylenstierna, J. C. I., Vallack, H. W., Davila, Y., Anenberg, S. C., Turner,

839   M. C., and Ashmore, M. R.: Updated global estimates of respiratory mortality in adults ≥30 years of

840   age   attributable   to   long-term   ozone   exposure,   Environ.   Health.   Persp.,   125,   087021,

841   https://doi.org/10.1289/EHP1390, 2017.

842   Martinez, M.: OH and HO2 concentrations, sources, and loss rates during the Southern Oxidants Study

843   in   Nashville,   Tennessee,   summer   1999,   J.   Geophys.   Res.-Atmos.,   108,   4617,

844   https://doi.org/10.1029/2003JD003551, 2003.

845   Mazzuca, G. M.,Ren, X., Loughner, C. P., Estes, M., Crawford, J. H., Pickering, K. E., Weinheimer, A.

846   J., and Dickerson, R. R.: Ozone production and its sensitivity to NOx and VOCs: results from the

847  DISCOVER-AQ field experiment, Houston 2013, Atmos. Chem. Phys., 16, 14463-14474,

848  https://doi.org/10.5194/acp-16-14463-2016, 2016.

849 Mills, G., Sharps, K., Simpson, D., Pleijel, H., Broberg, M., Uddling, J., Jaramillo, F., Davies, W. J.,

850  Dentener, F., Van den Berg, M., Agrawal, M., Agrawal, S. B., Ainsworth, E. A., Buker, P., Emberson,

851  L., Feng, Z., Harmens, H., Hayes, F., Kobayashi, K., Paoletti, E., and Van Dingenen, R.: Ozone

852  pollution will compromise efforts to increase global wheat production, Glob. Chang. Biol., 24, 3560-

853  3574, https://doi.org/10.1111/gcb.14157, 2018.

854 O'Neill, M. S., Jerrett, M., Kawachi, I., Levy, J. I., Cohen, A. J., Gouveia, N., Wilkinson, P., Fletcher, T.,

855  Cifuentes, L., Schwartz, J.: Health, wealth, and air pollution: advancing theory and methods, Environ.

856  Health. Persp., 111, 1861-70, https://doi.org/10.1289/ehp.6334, 2003.

857 Pan, X.; Kanaya, Y., Tanimoto, H., Inomata, S., Wang, Z., Kudo, S., and Uno, I.: Examining the major

858  contributors of ozone pollution in a rural area of the Yangtze River Delta region during harvest season,

859  Atmos. Chem. Phys., 15, 6101-6111, https://doi.org/10.5194/acp-15-6101-2015, 2015.

860 Ren, X., van Duin, D., Cazorla, M., Chen, S., Mao, J., Zhang, L., Brune, W. H., Flynn, J. H., Grossberg,

861  N., Lefer, B. L., Rappenglück, B., Wong, K. W., Tsai, C., Stutz, J., Dibb, J. E., Thomas Jobson, B.,

862  Luke, W. T., and Kelley, P.: Atmospheric oxidation chemistry and ozone production: results from

863  SHARP 2009 in Houston, Texas, J. Geophys. Res.-Atmos., 118, 5770-5780,

864  https://doi.org/10.1002/jgrd.50342, 2013.

865 Sadanaga, Y., Kawasaki, S., Tanaka, Y., Kajii, Y., and Bandow, H.: New system for measuring the

866  photochemical ozone production rate in the atmosphere, Environ. Sci. Technol., 51, 2871-2878,

867  https://doi.org/10.1021/acs.est.6b04639, 2017.

868 Shen, H., Liu, Y., Zhao, M., Li, J., Zhang, Y., Yang, J., Jiang, Y., Chen, T., Chen, M., Huang, X., Li, C.,

869  Guo, D., Sun, X., Xue, L., and Wang, W.: Significance of carbonyl compounds to photochemical ozone

870  formation in a coastal city (Shantou) in eastern China, Sci. Total. Environ., 764, 144031,

871  https://doi.org/10.1016/j.scitotenv.2020.144031, 2021.

872 Sklaveniti, S., Locoge, N., Stevens, P. S., Wood, E., Kundu, S., and Dusanter, S.: Development of an

873  instrument for direct ozone production rate measurements: measurement reliability and current

874  limitations, Atmos. Meas. Tech., 11, 741-761, https://doi.org/10.5194/amt-11-741-2018, 2018.

875 Tadic, I., Crowley, J. N., Dienhart, D., Eger, P., Harder, H., Hottmann, B., Martinez, M., Parchatka, U.,

876   Paris, J.-D., Pozzer, A., Rohloff, R., Schuladen, J., Shenolikar, J., Tauer, S., Lelieveld, J., and Fischer,

877   H.: Net ozone production and its relationship to nitrogen oxides and volatile organic compounds in the

878   marine boundary layer around the Arabian Peninsula, Atmos. Chem. Phys., 20, 6769-6787,

879   https://doi.org/10.5194/acp-20-6769-2020, 2020.

880   Wang, C., Yuan, B., Wu, C., Wang, S., Qi, J., Wang, B., Wang, Z., Hu, W., Chen, W., Ye, C., Wang, W.,

881   Sun, Y., Wang, C., Huang, S., Song, W., Wang, X., Yang, S., Zhang, S., Xu, W., Ma, N., Zhang, Z.,

882   Jiang, B., Su, H., Cheng, Y., Wang, X., and Shao, M.: Measurements of higher alkanes using NO+

883   chemical ionization in PTR-ToF-MS: important contributions of higher alkanes to secondary organic

884   aerosols in China, Atmos. Chem. Phys., 20, 14123–14138, https://doi.org/10.5194/acp-20-14123-

885   2020, 2020a.

886   Wang, F., An, J., Li, Y., Tang, Y., Lin, J., Qu, Y., Chen, Y., Zhang, B., and Zhai, J.: Impacts of uncertainty

887   in AVOC emissions on the summer ROx budget and ozone production rate in the three most rapidly-

888   developing economic growth regions of China, Adv. Atmos. Sci., 31, 1331-1342,

889   https://doi.org/10.1007/s00376-014-3251-z, 2014.

890   Wolfe, G. M., Marvin, M. R., Roberts, S. J., Travis, K. R., and Liao, J.: The Framework for 0-D

891   Atmospheric   Modeling   (F0AM)   v3.1,   Geosci. Model. Dev.,   9,   3309-3319,

892   https://doi.org/10.5194/gmd-9-3309-2016, 2016.

893   Wu, C., Wang, C., Wang, S., Wang, W., Yuan, B., Qi, J., Wang, B., Wang, H., Wang, C., Song, W., Wang,

894   X., Hu, W., Lou, S., Ye, C., Peng, Y., Wang, Z., Huangfu, Y., Xie, Y., Zhu, M., Zheng, J., Wang, X.,

895   Jiang, B., Zhang, Z., and Shao, M.: Measurement report: Important contributions of oxygenated

896   compounds to emissions and chemistry of volatile organic compounds in urban air, Atmos. Chem.

897   Phys., 20, 14769–14785, https://doi.org/10.5194/acp-20-14769-2020, 2020.

898   Yuan, B., Chen, W., Shao, M., Wang, M., Lu, S., Wang, B., Liu, Y., Chang, C.-C., and Wang, B.:

899   Measurements of ambient hydrocarbons and carbonyls in the Pearl River Delta (PRD), China, Atmos.

900   Res., 116, 93-104, https://doi.org/10.1016/j.atmosres.2012.03.006, 2012.

901   Zhang, A., Lin, J., Chen, W., Lin, M., and Lei, C.: Spatial-temporal distribution variation of ground-level

902   ozone in China's Pearl River Delta metropolitan region, Int. J. Environ. Res. Public Health., 18, 872,

903   https://doi.org/10.3390/ijerph 18030872, 2021.

904   Zhou, W., Cohan, D. S., and Henderson, B. H.: Slower ozone production in Houston, Texas following

905   emission reductions: evidence from Texas Air Quality Studies in 2000 and 2006, Atmos. Chem. Phys.,

906   14, 2777-2788, https://doi.org/10.5194/acp-14-2777-2014, 2014.

907   Zhu, M., Dong, H., Yu, F., Liao, S., Xie, Y., Liu, J., Sha, Q., Zhong, Z., Zeng, L., Zheng, J.: A new

908   portable instrument for online measurements of formaldehyde: from ambient to mobile emission

909   sources. Environ. Sci. Technol. Lett, 7, 292-297, https://dx.doi.org/10.1021/acs.estlett.0c00169, 2020.

910   Zou, Y., Deng, X. J., Zhu, D., Gong, D. C., Wang, H., Li, F., Tan, H. B., Deng, T., Mai, B. R., Liu, X. T.,

911   and Wang, B. G.: Characteristics of 1 year of observational data of VOCs, NOX and O3 at a suburban

912   site in Guangzhou, China. Atmos. Chem. Phys., 15, 6625-6636, https://doi.org/10.5194/acp-15-6625-

913   2015, 2015.

Measuring and modeling investigation of the Net Photochemical Ozone Production Rate via an improved dual-channel reaction chamber technique

Yixin Hao[1,2#], Jun Zhou[1,2#*], Jie-Ping Zhou[1,2], Yan Wang[1,2], Suxia Yang[1,2], Yibo Huangfu[1,2], Xiao-Bing Li[1,2], Chunsheng Zhang[3], Aiming Liu[3], Yanfeng Wu[1,2], Yaqing Zhou, Shuchun Yang[1,2], Yuweng Peng[1,2], Jipeng Qi[1,2], Xianjun He[1,2], Xin Song[1,2], Yubin Chen[1,2], Bin Yuan[1,2*], Min Shao[1,2]

[1]Institute for Environmental and Climate Research, Jinan University

[2]Guangdong-Hongkong-Macau Joint Laboratory of Collaborative Innovation for Environmental Quality

[3]Shenzhen National Climate Observatory, Shenzhen 518040, China

[#]Yixin Hao and Jun Zhou contribute equally to this work.

Correspondence to: Jun Zhou (junzhou@jnu.edu.cn) and Bin Yuan (byuan@jnu.edu.cn)

Contents:

1   **S1: The reaction and reference chambers.**

2   **1.1 Schematic diagram**

3   The specifications of the reaction and reference chambers are basically the same, which are composed of

4   a quartz glass cylinder, two O rings, two PTFE plates, and PTFE joint connections. Both inlet and outlet

5   of the quartz cylinder are connected to the PTFE plates and sealed by the O rings, the PTFE plates were

6   then fixed by the stainless-steel plates on a stainless-steel shelf. The length and inner diameter of the

7   quartz glass cylinder are 700 mm and 190.5 mm, respectively. The PTFE plate has a PTFE tube (outer

8   diameter of 12.7 mm) for air intake and outflow. For air inject, an PTFE tube passes through one PTFE

9   plate and is bent as "L-shape" at the inner surface side of the PTFE plate. The other PTFE plate on the

10   other side is equipped with a straight PTFE tube for air outflow (see Fig. S1).
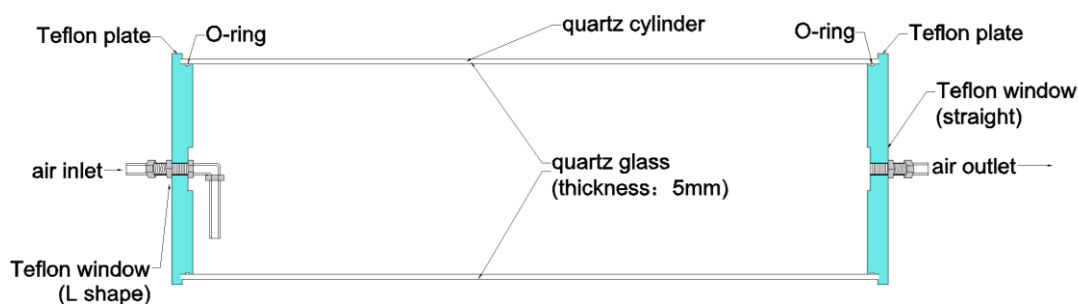
12   **Figure S1: Schematic diagram of the reaction and reference chambers.**

13   **1.2 Residence time of air in the reaction and reference chambers**

14   The residence time of air in the two chambers ($\langle\tau\rangle$) are critical for calculating $P(O_3)_{net}$. The air flow rate

15   through the reaction and reference chambers can be set at 1.3, 2, 3, 4, and 5 L min^{-1}, respectively,

16   depending on the measurement environment, therefore the residence time of air in these two chambers

17   under different air flow rates were also varied. The experimental schematic diagram and results of other

18   air flow rates are shown in the Supplement (Figs. S2 and S3).

19   We first measured $\langle\tau\rangle$ by introducing a short pulse of NO_2 gas at 5 L min^{-1} (obtained by mixing 0.2

20   L min^{-1} of 2.08 ppmv NO_2 standard gas with 5.2 L min^{-1} ultrapure) into the reaction and reference

21   chambers at $\tau = 0$, the airflow rates in the reaction and reference chambers were controlled by the flow

22   rate of the CAPS-NO_2 monitor (1.11 L min^{-1}) and pump (3.89 L min^{-1}), the time profile of NO_2 mixing

23   ratios ($C(\tau)$) at the exit of the chamber was measured using the CAPS-NO_2 monitor. The pulse width of

24   the introduced NO_2 gas was approximately 20 s and sufficiently shorter than $\langle\tau\rangle$. $C(\tau)$ is normalized by

25   Eq. (S1), which converts $C(\tau)$ to a probability density function ($E(\tau)$) (Sadanaga et al., 2017).

26    $$E\langle\tau\rangle=\frac{C(\tau)}{\int_0^\infty C(\tau)\,d\tau}$$ (S1)

27    $\langle\tau\rangle$ is an expectation value and was calculated using Eq. (S2).

28    $$\langle\tau\rangle=\int_0^\infty \tau E\langle\tau\rangle d\tau=\int_0^\infty \frac{\tau C(\tau)}{\int_0^\infty C(\tau)\,d\tau}\,d\tau$$ (S2)

29   Three sets of experiments of $\langle\tau\rangle$ of NO_2 in the reaction and reference chambers were carried out,

30   and the average $\langle\tau\rangle$ of NO_2 in the reaction and reference chambers were both 0.063 h, indicating that

31   there was no difference in the average $\langle\tau\rangle$ of the sampled air in these two chambers. We also investigated

32    $\langle\tau\rangle$ of NO_2 at the flow rate of 1.3, 2, 3, and 4 L min^{-1}, the measured average $\langle\tau\rangle$ were all closed to the

33   theoretical values. Figure S2 shows the schematic diagram of the experiments. We described the results

34   at the flow rates of 1.3, 2, 3, 4, and 5 L min^{-1} in Fig. S3 and Table S1.
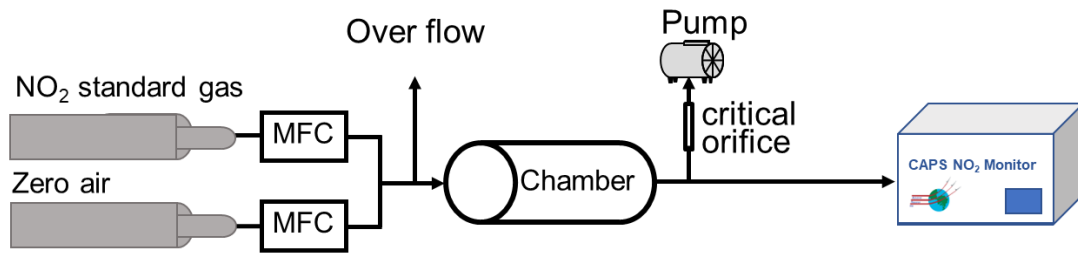
36   **Figure S2: Schematic diagram for measuring average residence time (MFC: Mass Flow Controller).**
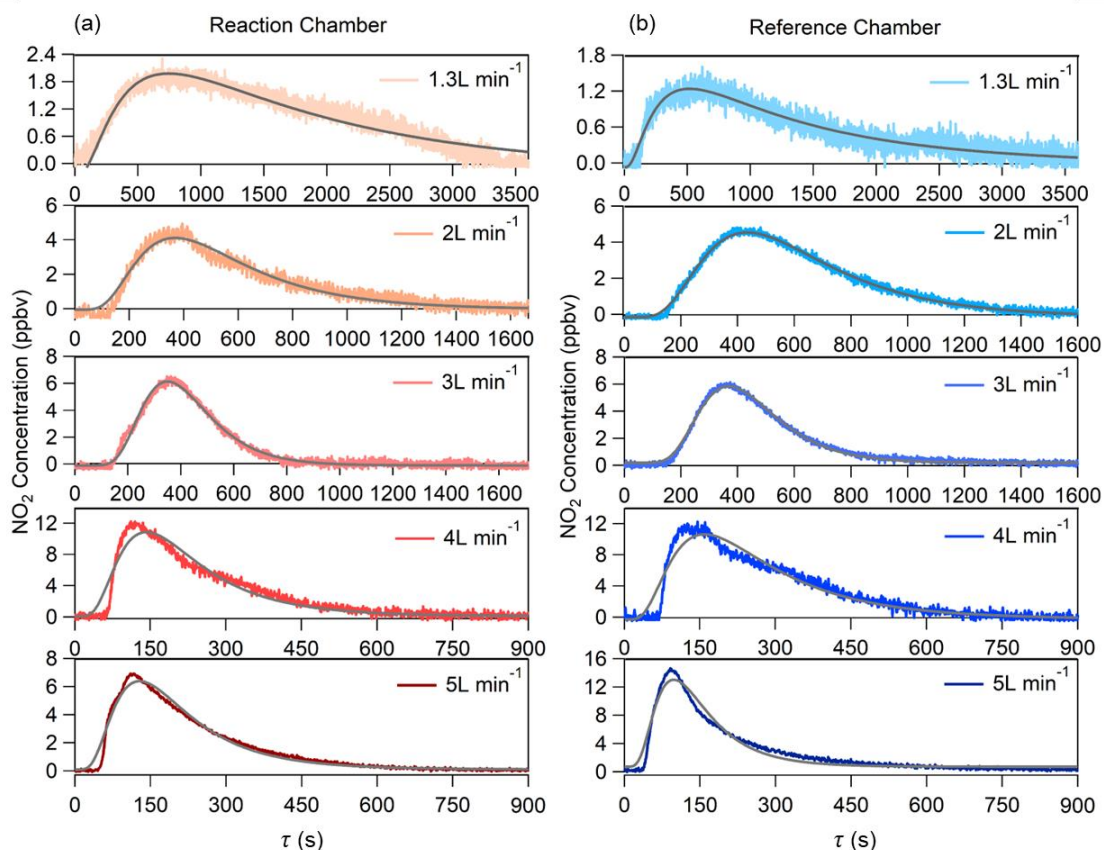
Figure S3: Average E(τ) time profiles in (a) the reaction and (b) the reference chambers at the sampling flow rates of 1.3, 2, 3, 4, and 5 L min^{-1}, respectively. The related residence time of NO$_2$ in the reaction and reference chambers of each air flow rate is shown in Table S1.

Table S1. Average residence time of air in the reaction and reference chambers.

Flow rate of air (L min^{-1})	Average residence time (h)	
	Reaction chamber	Reference chamber
1.3	0.350±0.0020	0.321±0.0026
2	0.160±0.0015	0.164±0.0022
3	0.111±0.0004	0.142±0.0002
4	0.067±0.0003	0.074±0.0003
5	0.063±0.0007	0.063±0.0005

1.3 Wall losses of NO$_2$ and O$_3$ in the reaction and reference chambers

In order to investigate the wall loss of O$_3$ or NO$_2$, we injected several steams of O$_3$ or NO$_2$ with different mixing ratios into the reaction and reference chambers, and measured the O$_3$ or NO$_2$ mixing ratios at the

49   inlet and outlet of the chambers. The O_3 used here were generated by injecting the ultrapure air into an

50   O_3 generator (P/N 97-0067-02, Analytic Jena, USA), O_3 mixing ratios were measured by a 2B O_3 monitor

51   based on a dual-channel UV-absorption technique (Model 205, 2B Technology, USA), and NO_2 mixing

52   ratios was monitored by the CAPS-NO_2 monitor. The wall losses of O_3 and NO_2 can be calculated as:

53    $O_{3\ loss} = \left(1 - \frac{[O_3]_{out}}{[O_3]_{in}}\right) \times 100\ \%$ (S3)

54    $NO_{2\ loss} = \left(1 - \frac{[NO_2]_{out}}{[NO_2]_{in}}\right) \times 100\ \%$ (S4)

55   where $[O_3]_{out}$ and $[NO_2]_{out}$ represent the mixing ratio of gas passing through the reaction and reference

56   chambers, $[O_3]_{in}$ and $[NO_2]_{in}$ represent the mixing ratio of gas passing through then bypass.

57   The experiments were conducted under dark conditions, the experimental schematic diagram is

58   shown in Fig. S4, and the results at the air flow rate of 1.3, 2, 3, 4, and 5 L min^{-1} are shown in Figs. S5-

59   S6 and Tables S2-S5. From Figs. S5-S6, at the air flow rate of 5 L min^{-1}, wall losses of O_3 in the reaction

60   and reference chambers were found to be approximately 0 % and 0.7 %, respectively, wall losses of NO_2

61   were found to be approximately less than 1.0 % for both chambers, which were smaller than the wall loss

62   of Ox in previous studies (as shown in Table S6), this indicates the small effects of Ox loss to $P(O_3)_{net}$

63   measurements in our NPOPR detection system. To investigate the influence of different flow rates to the

64   Ox wall losses, we also tested the wall loss of O_x at flow rates of 1.3, 2, 3, and 4 L min^{-1}, respectively,

65   we found that with the increase of the flow rate, the Ox wall losses decreased, but even with the flow rate

66   of 1.3 L min^{-1}, the wall loses were still smaller than 4 % and 2 % in the reaction chamber and the reference

67   chambers, respectively, more details are shown in Table S2. At the air flow rates of 1.3, 2, 3, and 4 L min^{-}

68   ^{1}, the wall losses of O_3 in the reaction chamber were found to be approximately 2 %, 0 %, 0 %, and 0 %,

69   respectively, the wall losses of O_3 in the reference chamber was found to be approximately 2 %, 1 %,

70   1 %, and 0 %, respectively. While the wall losses of NO_2 in the reaction chamber at the air flow rates of

71   1.3, 2, 3, and 4 L min^{-1} were found to be approximately 4 %, 4 %, 2 %, and 0 %, respectively, the wall

72   losses of NO_2 in the reference chamber were found to be approximately 2 %, 1 %, 0 %, and 0 %,

73   respectively. The regression lines have non-zero intercepts but not significant. We added the regression

74   fittings without intercept, and compared the regression fitting results with and without intercept (as

75   shown in Figs. S5 and S6). We found that the O_3 and NO_2 wall losses were not much different (as shown

76   in Tables S2 and S3), and the wall loss affected by the fitting intercepts for NO_2 (at ambient mixing ratios

77   of 0-100 ppbv) and O_3 (at ambient mixing ratios of 0-200 ppbv) at the air flow rate of 5 L min^{-1} were all

78   below 4 % (as shown in Tables S4 and S5). We found that when the O_3 have negative intercepts, the O_3

79   wall losses are still below 4 %, which is not significant.

80   Sklaveniti et al. (2018) found that the wall loss of NO_2 is significantly less than that of O_3 at higher

81   humidity levels. However, in our O_3 photo-enhanced uptake experiments, the wall loss of O_3 was almost

82   unaffected by humidity at a flow rate of 5 L min^{-1}. We also tested the wall losses of NO_2 and O_3 in the

83   chamber at a 5 L min^{-1} flow rate at different humidities of 35-75 %, the detailed results are shown in Fig.

84   S7 and S8, which shows that the variation in humidity effected the wall loss of NO_2 and O_3 by 0.03-

85   0.12 % and 1.06-1.19 %, respectively, which is much smaller than the instrument detection error (which

86   is 2 % at ambient NO_2 mixing ratios of 0-100 ppb), thus we didn't count this interference during the data

87   analysis.

88
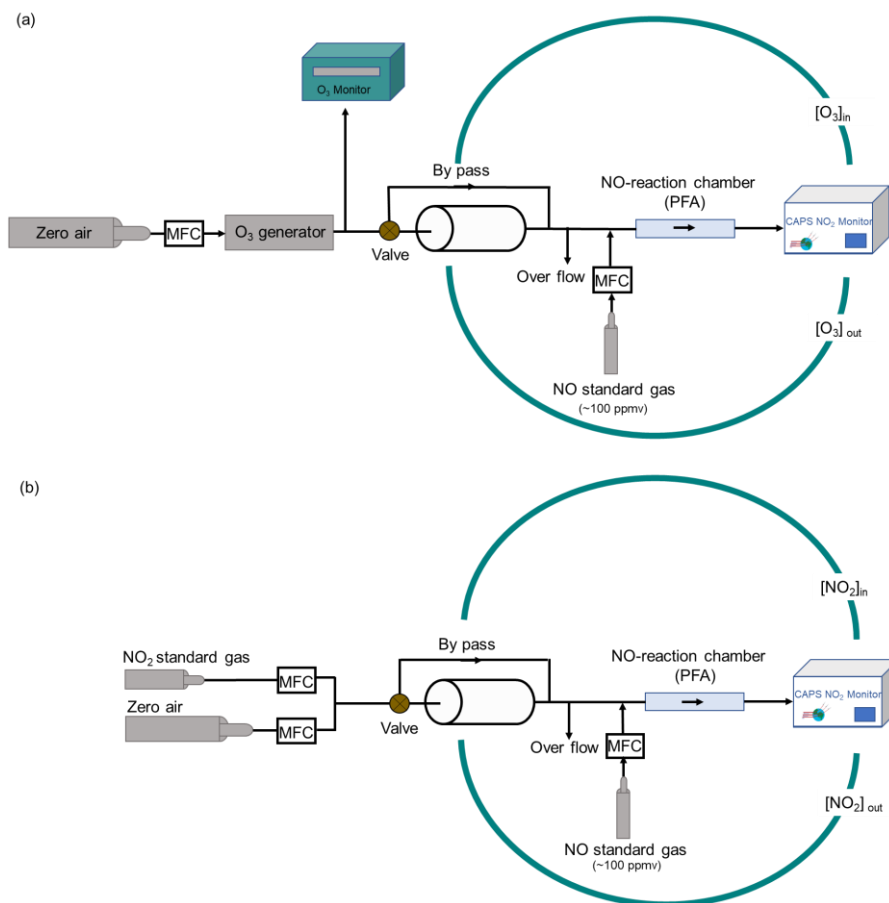
89
90
91   **Figure S4: Schematic diagram for testing (a) O_3 and (b) NO_2 wall loss in the reaction and reference chambers**
92   **(MFC: Mass Flow Controller).**

93
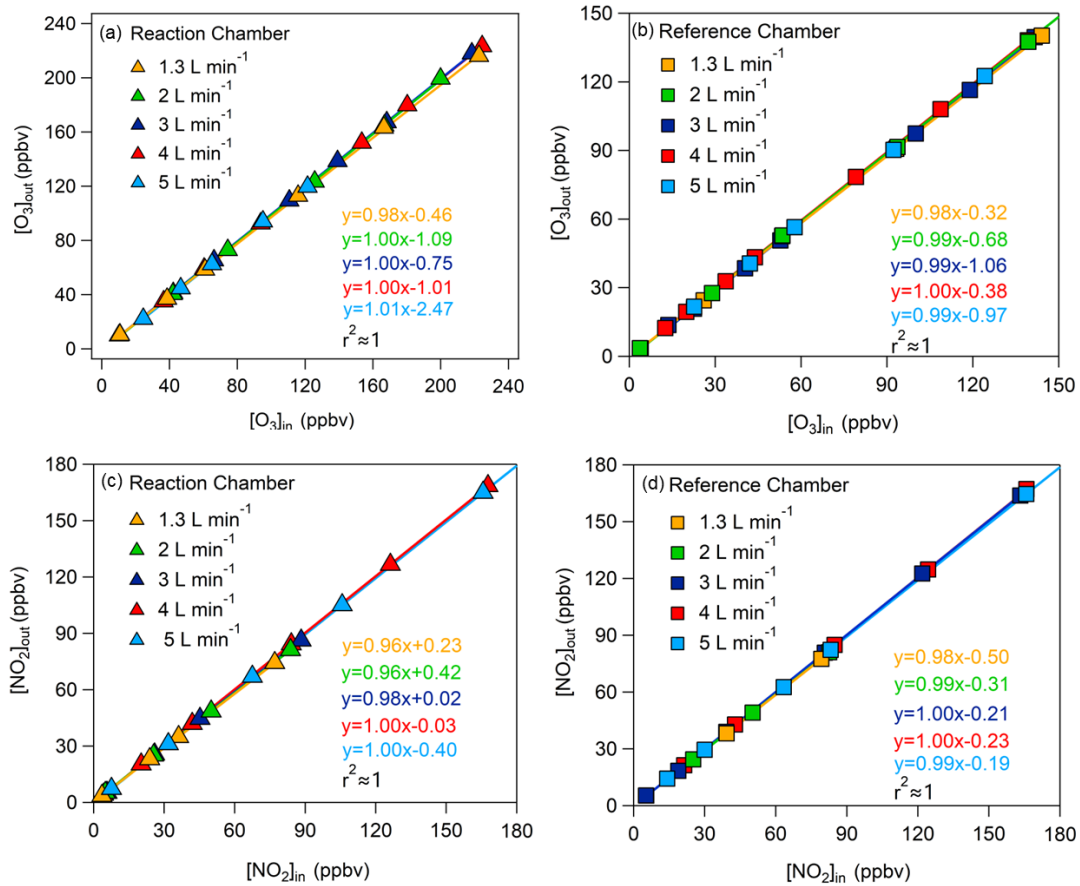
Figure S5: Relationship between (a,b) $[O_3]_{in}$ and $[O_3]_{out}$ and (c,d) $[NO_2]_{in}$ and $[NO_2]_{out}$ in the reaction and reference chambers with intercepts at the flow rates of 1.3, 2, 3, 4, and 5 L min^{-1}, respectively, the solid lines represent the linear fitting of the O_3 or NO_2 mixing ratios at the inlet and outlet of the chambers.

94

95

96

97

98
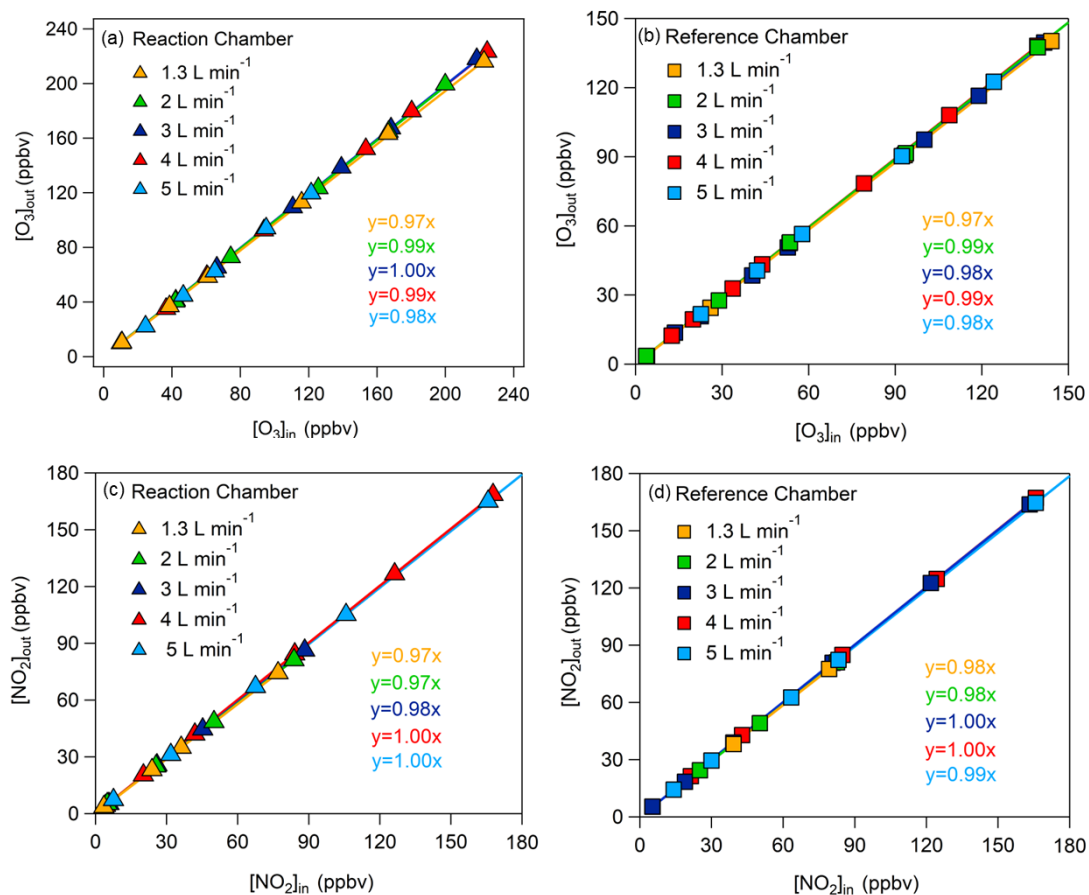
Figure S6: Relationship between (a, b) $[O_3]_{in}$ and $[O_3]_{out}$ and (c,d) $[NO_2]_{in}$ and $[NO_2]_{out}$ in the reaction and

reference chambers without intercepts at the flow rates of 1.3, 2, 3, 4, and 5 L min^{-1}, respectively, the solid

lines represent the linear fitting of the O_3 or NO_2 mixing ratios at the inlet and outlet of the chambers.

102

Table S2. Wall losses of O_3 and NO_2 of the reaction and reference chambers with intercepts.

Flow rate of air (L min^{-1})	Wall losses of O_3 (%)		Wall losses of NO_2 (%)	
	Reaction chamber	Reference chamber	Reaction chamber	Reference chamber
1.3	2.0	2.0	4.0	2.0
2	0.0	1.0	4.0	1.0
3	0.0	1.0	2.0	0.0
4	0.0	0.0	0.0	0.0
5	0	0.7	0.3	0.6

108 **Table S3. Wall losses of O$_3$ and NO$_2$ of the reaction and reference chambers without intercepts.**

Flow rate of air (L min^{-1})	Wall losses of O$_3$ (%)		Wall losses of NO$_2$ (%)	
	Reaction chamber	Reference chamber	Reaction chamber	Reference chamber
1.3	3.0	3.0	3.0	2.0
2	1.0	1.0	3.0	2.0
3	0.0	2.0	2.0	0.0
4	1.0	1.0	0.0	0.0
5	2.0	2.0	0.0	1.0

109

110 **Table S4. NO$_2$ wall loss affected by the intercept.**

Ambient NO$_2$ mixing ratios (ppbv)	Wall loss affected by the intercept (NO$_2$, %)	
	Reaction chamber	Reference chamber
20	2.0	2.0
40	1.0	1.5
60	0.7	1.3
80	0.5	1.2
100	0.4	1.2

111

112 **Table S5. O$_3$ wall loss affected by the intercept.**

Ambient O$_3$ mixing ratios (ppbv)	Wall loss affected by the intercept (O$_3$, %)	
	Reaction chamber	Reference chamber
50	3.9	2.9
80	2.1	2.2
120	1.1	1.8
160	0.5	1.6
200	0.2	1.5

113

114

115

116

117 **Table S6. O₃ and NO₂ wall loss from this study (at air flow rate of 5 L min⁻¹) and literatures (variable air flow**
118 **rate).**

	Reaction chamber	Reference chamber	Literatures / air flow rate
O$_3$ loss rate	<3 %	<3 %	Cazorla *et al.*,2010 / 1.5 L min⁻¹
	1.3 %	1.4 %	Sadanaga *et al.*,2017 / 0.5 L min⁻¹
	5-15 %	5-13 %	Sklaveniti *et al.*, 2018 / 2.3 L min⁻¹
	0 %	0.7 %	This study / 5.0 L min⁻¹
NO$_2$ loss rate	<1 %	<1 %	Cazorla *et al.*,2010 / 1.5 L min⁻¹
	insignificant	insignificant	Sadanaga *et al.*,2017 / 0.5 L min⁻¹
	<3%	<3 %	Sklaveniti *et al.*, 2018 / 2.3 L min⁻¹
	0.3 %	0.6 %	This study / 5.0 L min⁻¹

119
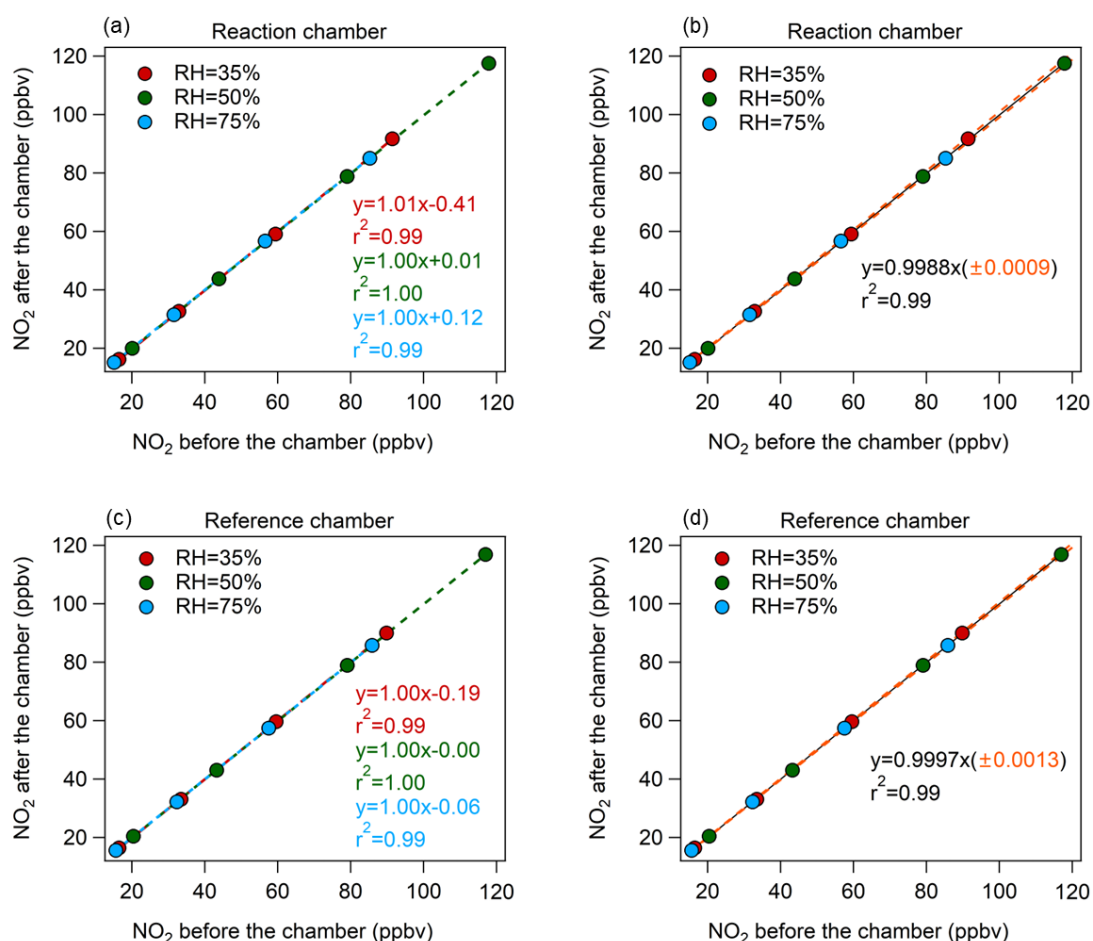
120

121 **Figure. S7 (a) and (c) represent the NO₂ wall loss at different humidities for the reaction and reference**

122 **chambers, respectively, (b) and (d) represent the points fitted to all humidities, respectively. Uncertainty in**

123 **the regression formula was one standard deviation (1σ).**

124
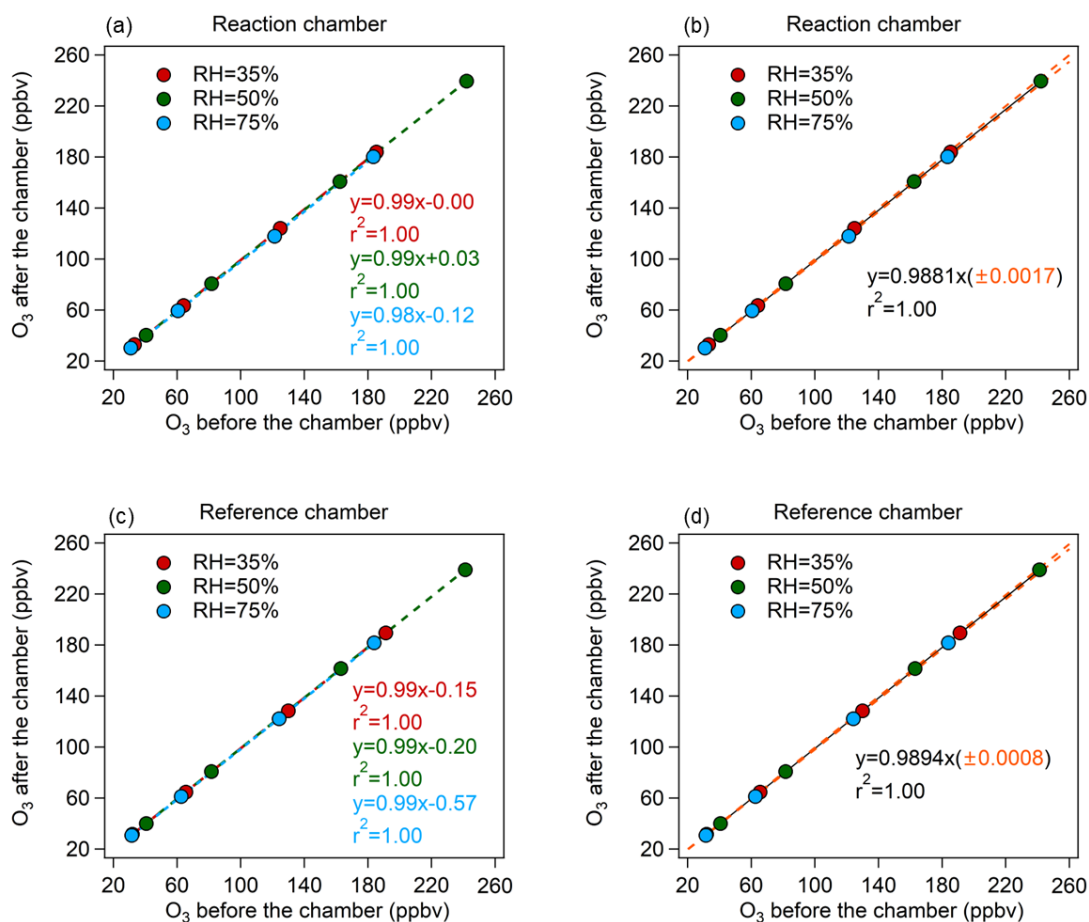
Figure. S8 (a) and (c) represent the O₃ wall loss at different humidities for the reaction and reference chambers,

respectively, (b) and (d) represent the points fitted to all humidities, respectively. Uncertainty in the regression

formula was one standard deviation (1σ).

1.4 HONO production in the reaction and reference chambers with variations of temperature and

humidities

We tested the HONO production in the reaction and reference chambers under weather conditions similar

to those during the SZMGT observations (humidities of 60-90% at a temperature of ~ 20 °C and J(NO$_2$)

of ~ 0-8 × 10^{-3} s^{-1}) at a 5 L min^{-1} sampling flow rate. We found that the HONO mixing ratios in the

reaction and reference chambers were almost the same and not statistically different from that in the

ambient air within the standard deviation, as shown in Fig. S9; therefore, we assumed that the HONO

production in the reaction and reference chambers would not cause a significant difference in P(O$_3$)$_{net}$ in

the two chambers.
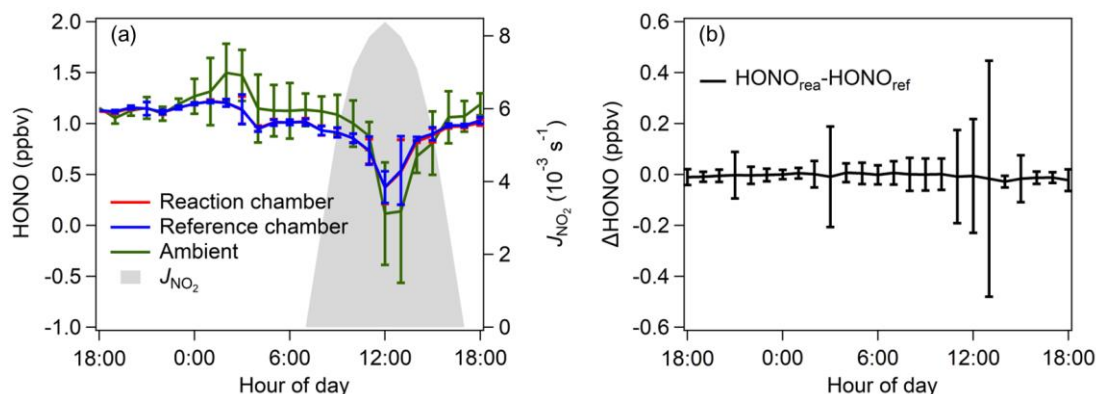
138

139   **Figure. S9 (a) The mixing ratios of HONO in the reaction and reference chambers and (b) the difference of**

140   **HONO mixing ratios the reaction and reference chambers.**

141   **1.5 The light transmittance in the reaction and reference chambers**

142   We measured the transmittivities of all species as follows: we simulated the illumination by adjusting

143   the sun light (SERIC XG-500B) to provide different intensities of illumination to study the solar UV

144   transmittance through the reaction and reference chambers. The photolysis frequencies of the species

145   NO_2, O_3, and HONO, etc. were measured using the Actinic flux spectrometer (PFS-100; Focused

146   Photonics Inc). Measurements are performed in laboratory. The UV blocking of the reference chamber

147   coated with UV protection film was evaluated by comparing the radiation measurements outside the

148   reference chamber with the measurements inside the reference chamber. Similar measurements and

149   comparisons were made for transparent reaction chambers. The results for the reaction and reference

150   chambers are shown in Table S7.

151   According to the working theory of the actinic flux spectrometer, the measurement error may rise

152   from the angular response deviation of the quartz receiver head. According to Bohn et al. (2017), the

153   measurement error of the actinic flux spectrometer can reach±5 %. According to this, we re-evaluated

154   the transmittivity error listed in Table 1 and Table S7 as follows:①calculate the absolute measurement

155   error of all measured J values inside and outside the reaction and reference chambers based on the ±5 %

156   instrument measurement error; ②calculate the average values of all the measured J values (including

157   ($J(NO_2)$, $J(O1D)$, $J(HONO)$, $J(H_2O_2)$, $J(NO_3\_M)$, $J(NO_3\_R)$, $J(HCHO\_M)$, and $J(HCHO\_R)$) inside and

158   outside the chambers; ③calculate the propagated error of transmittivity, using the following error

159   propagation equation:

160 $$\sigma_{\text{Transmittivity}}= \sqrt{(\frac{\sigma_{J\text{ value in}}}{A_{J\text{ value in}}})^2 + (\frac{\sigma_{J\text{ value out}}}{A_{J\text{ value out}}})^2} \qquad (S5)$$

161 where $\sigma_{\text{Transmittivity}}$ represents the transmittivity error; $\sigma_{J\text{ value in}}$ and $\sigma_{J\text{ value out}}$ represent the

162 measurement error of J value inside and outside the chambers, respectively; $A_{J\text{ value in}}$ and $A_{J\text{ value out}}$

163 represent the average J values measured inside and outside the chambers, respectively.

164

165 **Table S7. Photolysis frequency J (s^{-1}) of different species and the transmittivities of J values in the reaction**

166 **and reference chambers. The shaded and clear regions correspond to the photolysis frequencies and the**

167 **transmittivities of J values in the reference (Ultem coated) and reaction (clear) chambers, respectively. The**

168 **"transmittivities" column shows the transmittivities of the tested species from the measurements conducted**

169 **with the set photolysis frequencies using SERIC XG-500B sunlight (this study) and ambient (literature). It**

170 **should be noted that the errors listed here are relatively large and may not reliable due to a limit number of**

171 **measurement points (3 points for each species). The calculated transmittivity errors are 0.07 for all species**

172 **based on the ±5 % measurement error of the instrument.**

173

	Outside Chamber (s^{-1})	Inside chamber (s^{-1})	Transmittivities	
			Each experiment	Averaged
$J(NO_2)$	6.068E-03	5.744E-03	0.947	
	8.418E-03	8.598E-03	1.021	0.985 ±0.037
	1.360E-02	1.344E-02	0.988	
	5.996E-03	4.700E-04	0.078	
	1.064E-02	1.134E-03	0.107	0.094 ±0.014
	1.382E-02	1.324E-03	0.095	
$J(O^1D)$	5.609E-05	5.484E-05	0.978	
	1.088E-04	1.151E-04	1.050	1.020 ±0.04
	1.240E-04	1.240E-04	1.000	
	7.005E-05	6.750E-07	0.010	
	9.825E-05	3.016E-06	0.031	0.019 ±0.011
	1.243E-04	2.205E-06	0.018	
$J(HONO)$	1.058E-03	9.994E-04	0.944	
	1.468E-03	1.494E-03	1.018	0.983 ±0.037
	2.376E-03	2.344E-03	0.986	
	1.047E-03	2.154E-06	0.002	
	1.281E-03	2.588E-06	0.002	0.002 ±0.0002
	2.417E-03	5.596E-06	0.002	
$J(H_2O_2)$	6.157E-06	5.818E-06	0.944	1.000

	1.370E-05	1.356E-05	0.990	±0.060
	1.200E-05	1.279E-05	1.065	
	6.145E-06	3.451E-08	0.006	0.005
	1.080E-05	4.942E-08	0.005	±0.0006
	1.393E-05	6.160E-08	0.004	
$J(NO_3\_M)$	1.314E-02	1.277E-02	0.971	1.002
	2.983E-02	2.993E-02	1.003	±0.030
	1.849E-02	1.906E-02	1.086	
	1.284E-02	9.929E-03	0.773	0.916
	2.342E-02	2.437E-02	1.041	±0.134
	3.040E-02	2.839E-02	0.934	
$J(NO_3\_R)$	9.881E-02	9.575E-02	0.970	0.999
	2.224E-01	2.226E-01	1.001	±0.030
	1.386E-01	1.425E-01	1.028	
	9.669E-02	7.461E-02	0.772	0.913
	1.751E-01	1.814E-01	1.036	±0.030
	2.268E-01	2.113E-01	0.932	
$J(HCHO\_M)$	2.645E-05	2.492E-05	0.942	0.997
	5.927E-05	5.845E-05	0.986	±0.006
	5.188E-05	5.514E-05	1.063	
	2.626E-05	1.017E-07	0.0038	0.0015
	4.643E-05	1.810E-08	0.0004	±0.002
	6.026E-05	1.620E-08	0.0003	
$J(HCHO\_R)$	5.800E-05	5.737E-05	0.989	1.021
	5.081E-05	5.394E-05	1.062	±0.004
	3.594E-05	3.617E-05	1.007	
	3.174E-05	2.670E-09	~0	0.0026
	4.561E-05	1.800E-07	0.0039	±0.002
	5.892E-05	2.290E-07	0.0039	

174

175
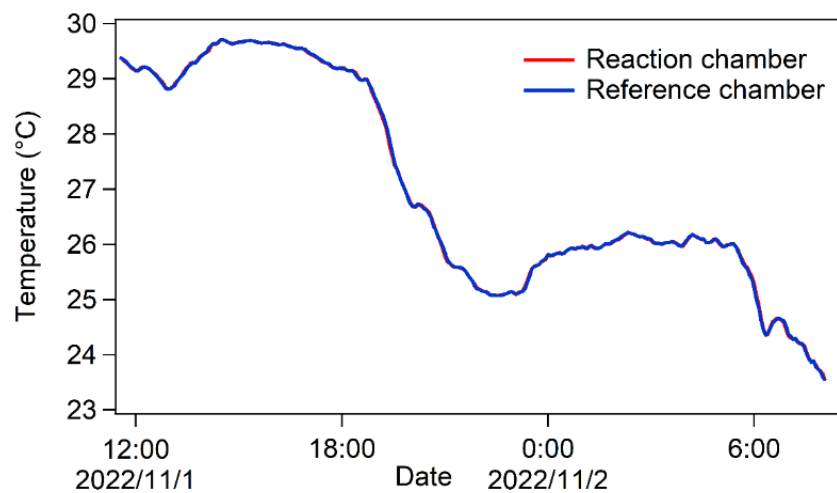
176 **Figure S10. Air temperature in the reaction and reference chambers during the ambient field observation on**

177 **Panyu campus of Jinan University.**

178
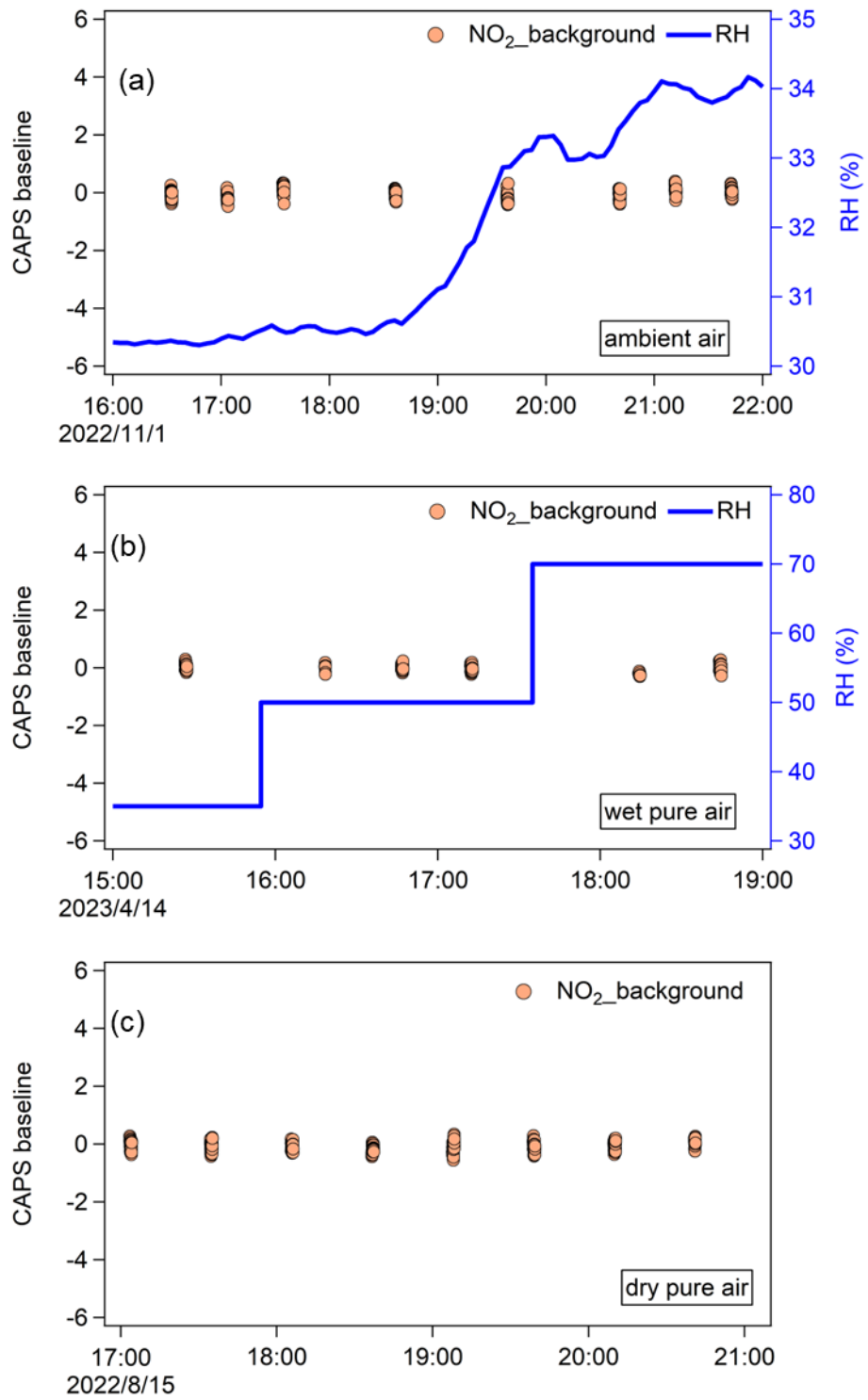
Figure S11. Time series of CAPS baseline and RH when measuring ambient air (a), and when injecting wet
(b) and dry (c) pure air in the laboratory, respectively.

181

182   **1.5 The quantitative conversion efficiency of O_3 to NO_2 (α) in the NO-reaction chamber**
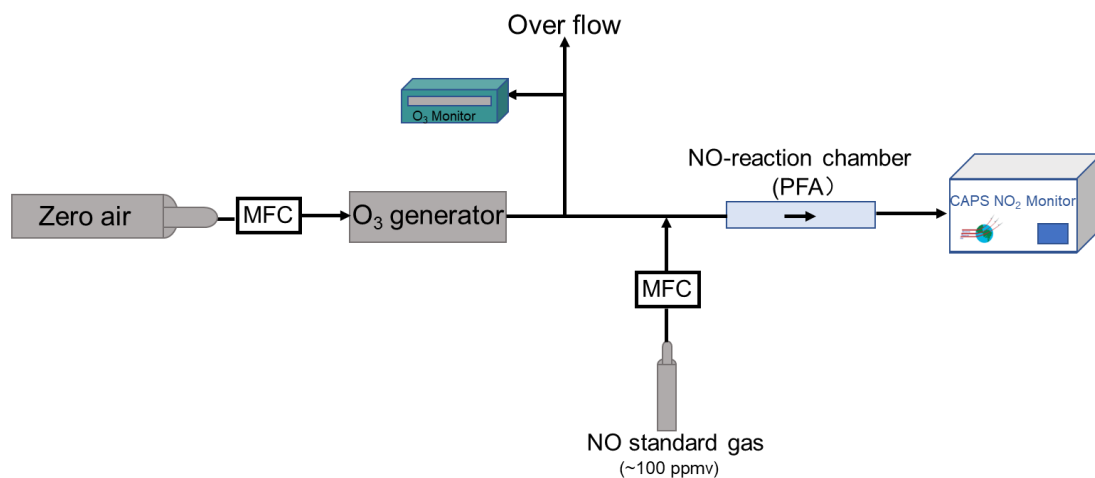
183
184   **Figure S12: Schematic diagram for measuring O_3 to NO_2 conversion efficiency in the NO-reaction chamber**
185   **(MFC: Mass Flow Controller).**
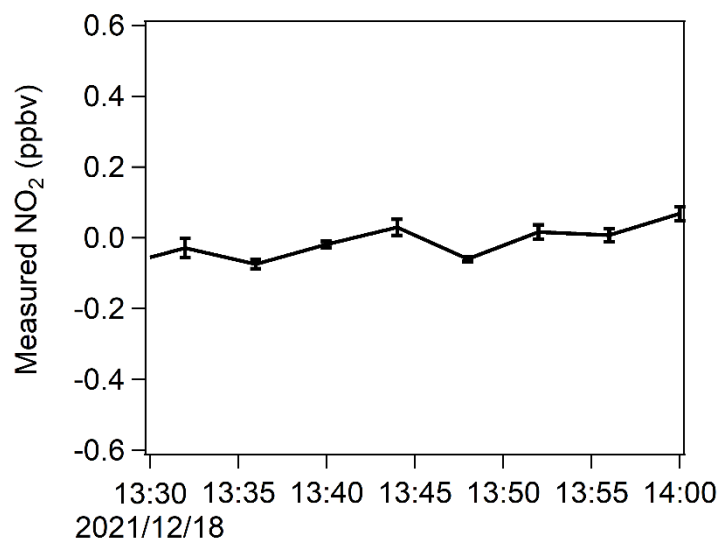
186
187   **Figure S13 Time series of NO_2 when injecting NO into CAPS-NO_2 monitor.**

188   **1.6 The airtightness of the reaction and reference chambers**

189
190

191   **Figure S14. Schematic diagram for investigating the airtightness of the reaction and reference chambers,**
192   **where MFC1 could measure air flow rate and pressure at the chamber inlet, MFC2 could measure air flow**
193   **rate and pressure at the chamber outlet.**

194

Table S8: Airtightness tests of the reaction and reference chambers (by testing the differences of [air flow rate × gas pressure] at the inlet and outlet of the chambers).

	Inlet flow rate (L min^{-1})	Inlet pressure (PSIA)	Inlet flow rate × Inlet pressure	Outlet flow rate (L min^{-1})	Outlet pressure (PSIA)	Outlet flow rate × Outlet pressure	Δ [air flow rate × pressure] (Difference at Inlet and Outlet) / [Inlet flow rate × Inlet pressure] (%)
Reaction chamber	3.80	14.67	55.74	3.81	14.63	55.74	0.00
	3.46	13.48	46.64	3.51	13.43	47.14	1.07
	3.19	12.51	39.90	3.22	12.42	39.99	0.22
	2.93	11.54	33.81	3.00	11.53	34.59	2.33
Reference chamber	3.80	14.68	55.78	3.80	14.61	55.52	0.47
	3.33	13.04	43.42	3.38	13.00	43.94	1.20
	3.12	12.3	38.37	3.16	12.14	38.36	0.03
	2.83	11.25	31.84	2.91	11.24	32.71	2.73

S2: The LOD and measurement error of the NPOPR detection system.

Table S9. The upper limit values of LODs of the CAPS-NO$_2$ monitor for the reaction chamber, reference chamber, and $P(O_3)_{net}$ at different flow rates.

Flow rate of air (L min^{-1})	LOD (3σ)		
	Reaction chamber (ppbv)	Reference chamber (ppbv)	$P(O_3)_{net}$ (ppbv h^{-1})
1.3	0.02	0.02	0.07
3	0.10	0.10	1.4
5	0.13	0.07	2.3

The $P(O_3)_{net}$ error was calculated according the instrumental error of the CAPS-NO$_2$ monitor and the O$_3$ light-enhanced loss in the reaction and reference chambers. More details are described as follows:

Calibration of CAPS NO$_2$ monitor CAPS NO$_2$ monitor was used to measure the NO$_2$ standard gas after we have calibrated it using the gas-phase titration method using NO and O$_3$. We used the CAPS-NO$_2$ monitor reading as a transition value between the two to obtain the NO$_2$ standard gas and NO+O$_3$

208 mixing ratios corresponding to the same CAPS-NO$_2$ monitor reading. Results showed the purification of

209 NO$_2$ standard gas was good enough to calibrate CAPS-NO$_2$ monitor, as shown in Fig. S15
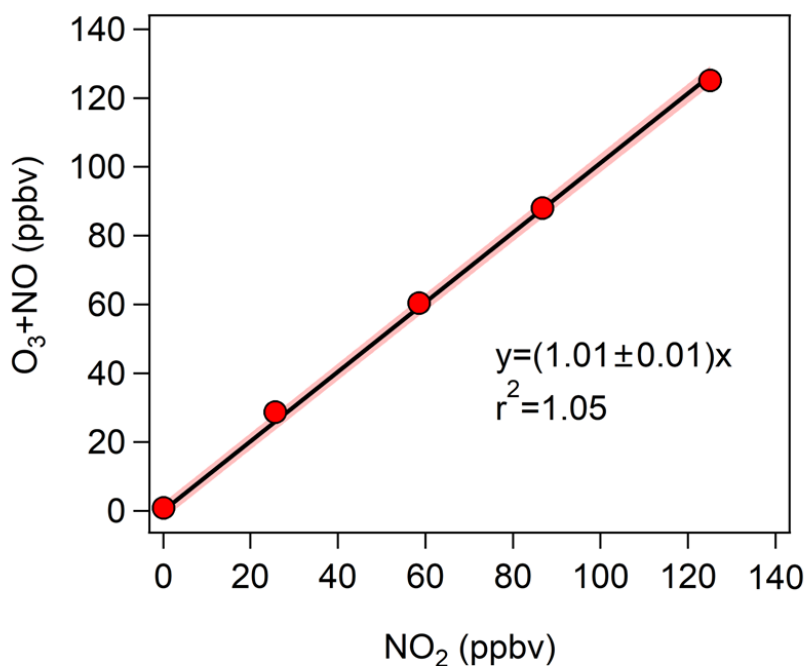
210

211 **Figure. S15 Correlation between NO$_2$ standard gas and the NO$_2$ generated using the gas-phase titration**

212 **method (NO + O$_3$).**

213 ***The instrumental error of CAPS-NO$_2$ monitor*** $((O_{X_{CAPS}})_{error})$ was calculated from the fluctuation

214 range of the 68.3 % confidence interval of the calibration curve as shown in Fig. 4, the relationship

215 between the $(O_{X_{CAPS}})_{error}$ and the measured Ox value ($f_{measured}$) can be expressed as a power function

216 curve, as shown in Eq. (S6):

217 $(O_{X_{CAPS}})_{error} = 9.72 f_{measured}^{-1.0024}$ (S6)

218 ***The light-enhanced loss of O$_3$ in the reaction and reference chambers*** at 5 L min^{-1} (the ambient

219 observation used flow rate in this study) were investigated by carrying out the following experiment:

220 injecting the O$_3$ with a mixing ratio of about 130 ppbv generated by the O$_3$ generator (P/N 97-0067-02,

221 Analytic Jena US, USA) to ensure that no photochemical O$_3$ was produced during the outdoor experiment.

222 The $J(O^1D)$, T, RH, P, and O$_3$ mixing ratios at the inlet and outlet of the reaction and reference chambers

223 were measured simultaneously. The T and RH were measured by the thermometer (Vaisala, HMP110,

224 USA). The light-enhanced loss coefficient of O$_3$ (γ) was calculated using Eq. (S7), the relationship of

225 $J(O^1D)$ with γ is shown in Fig. S16a. The obtained γ -$J(O^1D)$ equation listed in Eq. (S7) was used to

226 correct the light-enhanced loss of O_3 in the reaction and reference chambers during the daytime to

227 excluded the influence of light-enhanced loss.

228 $$\gamma = \frac{d[O_3] \times D}{\omega \times [O_3] \times \tau}$$ (S7)

229 where $d[O_3]$ represents the difference between the O_3 mixing ratios at the inlet and outlet of the reaction

230 and reference chambers, D is the diameter of the chambers, ω is the average velocity of O_3 molecules,

231 $[O_3]$ is the injected O_3 mixing ratio at the inlet of the reaction and reference chambers, and τ is the

232 average residence time of the air in the reaction and reference chambers.
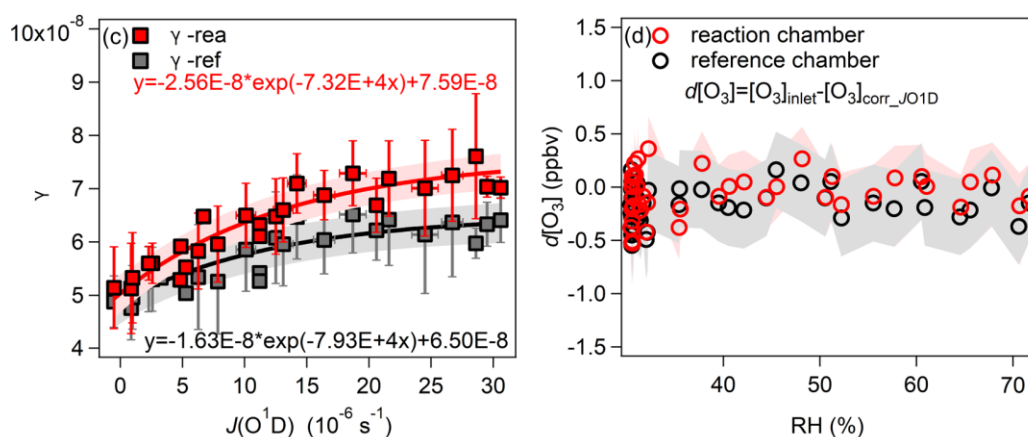
233

234 **Figure S16: The relationship of (a) γ and $J(O^1D)$ and (b) RH and $d[O_3]$ in the reaction and reference**

235 **chambers, which is calculated from the 68.3 % confidence interval of the fitting lines between γ and $J(O^1D)$,**

236 **the shaded areas represented the maximum fluctuation range under this confidence level.**

237 When quantifying the light-enhanced O_3 loss ($d[O_3]$) during ambient air measurement, we first

238 calculate γ using the measured $J(O^1D)$ and the γ -$J(O^1D)$ equations listed in Fig. S16a in the reaction

239 and reference chambers, then using the measured $[O_3]$ and Eq. (S7) to calculate $d[O_3]$.

240 The O_3 mixing ratio change after the correction of the light-enhanced loss of O_3 ($d[O_3]$) showed no

241 clear correlation with RH for both reaction and reference chambers, as shown in Fig. S16b, which

242 indicates that the RH had no influence to the O_3 mixing ratio change during the observation period. It

243 should be noted that the final error of Ox of the reaction and reference chambers includes the

244 measurement error of CAPS-NO_2 monitor (calculated by Eq. (S6)) and the error caused by γ, so the

245 measured $P(O_3)_{net}$ error can be calculated according to Eq. (7) in manuscript.

246 $$\left(O_X\right)_{error} = \sqrt{\left(O_{X\gamma}\right)_{error}^2 + \left(O_{XCAPS}\right)_{error}^2}$$ (S8)

247 where $(O_{X\gamma})_{error}$ represents the error of the Ox of the reaction and reference chambers corrected by γ.

248

 S3: Supplement materials for the field observations.

250   Figure S17 shows the measurement site of the observation campaign, conducted at the Shenzhen

251 Meteorological Gradient Tower (SZMGT), which is located in Shenzhen, Pearl River Delta (PRD) region

252 in China.
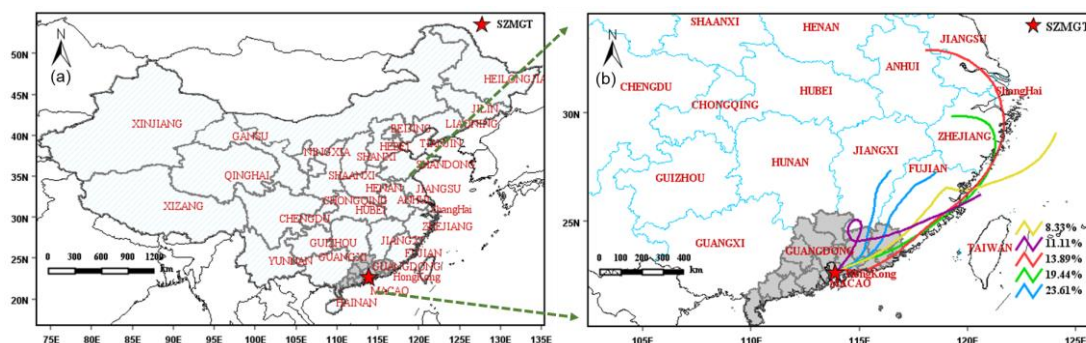
253

254

255 **Figure S17: (a)The geographic location of the measurement site and (b) the integrated ambient air backward**

256 **trajectories during sampling period from 7 December, 00:00 to 10 December 2021, 00:00 in Shenzhen (China).**

257 **The above figures were obtained by using the MeteoInfo weather mapping software in the TrajStat plugin**

258 **(Deshpande et al., 2016; Hao et al., 2020). Figure S17b was obtained by the Internet-based Hybrid-Single**

259 **Particle Lagrangian Integrated Trajectory (HYSPLIT) Model, the required data was downloaded via**

260 **ftp://arlftp.arlhq.noaa.gov/pub/archives/gdas1 (NOAA). Frequency grid resolution: 5.0° × 5.0°,trajectory**

261 **duration: 72 h. The air mass during the campaign were mainly from Jiangxi and Fujian, which had a 23.61 %**

262 **probability, followed by Zhejiang, Anhui, east coast, and East China Sea, which had 19.44 %, 13.89 %,**

263 **11.11 %, and 8.33 % probability, respectively.**

264
265
266
267
268
269
270
271
272
273
274
275
276
277
278
279
280
281

282 **Table S10a: Summary of maximum $P(O_3)_{net}$ of field measurements in literatures.**

Measurement site	The type of site	Time	$P(O_3)_{net}$ (ppbv h^{-1})	Reference
Wakayama, Kyoto, Japan	remote area	27 July to 8 August 2014	10.5 ppbv h^{-1}	Sadanaga et al., 2017
State College, Pennsylvania, U.S.A.	urban area	Summer 2008	~30 ppbv h^{-1}	Cazorla et al., 2010
Houston, Texas, U.S.A.	urban area	October 2013	40-50 ppbv h^{-1}	Baier et al., 2015
Bloomington, Indiana, U.S.A.	a site 2.5 km northeast of the Indiana University Bloomington campus	30 May 2010	~30 ppbv h^{-1}	Sklaveniti et al., 2018
Houston, Texas, U.S.A.	urban area	15 April to 31 May 2009	100 ppbv h^{-1}	Ren et al., 2013
Shenzhen, Guangdong, China	a village in Bao'an district	7 to 9 December 2021	34.1 ppbv h^{-1}	This study

283

284 **Table S10b: Summary of maximum $P(O_3)_{net}$ of model simulation in literatures.**

285

Site	The type of site	Time	$P(O_3)_{net}$ (ppbv h^{-1})	Reference
Fukue Island, Japan	a remote area	May to June 2009	1-2 ppbv h^{-1}	Kanaya et al., 2016
Chelmsford, Essex, U.K.	a site 2 miles west of Chelmsford in Essex and 25 miles north east of London	Summer 2003	7.2 ppbv h^{-1}	Emmerson et al., 2007
Houston, Texas, U.S.A.	suburban area	the September 2013	~10 ppbv h^{-1}	Mazzuca et al., 2016
Houston, Texas, U.S.A.	urban area	from 15 April to 31 May 2009	15-20 ppbv h^{-1}	Ren et al., 2013
Houston, Texas, U.S.A.	urban area	from August to September 2006	45 ppbv h^{-1}	Chen et al., 2010; Chen et al., 2012
Houston, Texas, U.S.A.	urban area	September 2013	~30 ppbv h^{-1}	Mazzuca et al., 2016

286

287 **S4: Supplement materials for the MCM modeling.**

288 **Table S11. VOCs mixing ratios during 7- 9 December 2021 in SZMGT (units: pptv) used by the model.**

Chemicals	Classification	Mean±SD (pptv)	Chemicals	Classification	Mean±SD (pptv)
Alkanes		30516±27079	Aromatics		7098±5855
n-butane	NMHC	8803±6422	toluene	NMHC	3684±2688
propane	NMHC	7086±5169	*m*/*p*-xylene	NMHC	1392±1370
isobutane	NMHC	4983±3635	ethylbenzene	NMHC	591±582
ethane	NMHC	3461±2525	*o*-xylene	NMHC	572±563
isopentane	NMHC	1712±1249	benzene	NMHC	528±336
n-pentane	NMHC	1570±1146	styrene	NMHC	159±191
n-hexane	NMHC	633±462	1,2,4-trimethylbenzene	NMHC	39±29
2-methylpentane	NMHC	473±345	*m*-ethyltoluene	NMHC	38±28
3-methylpentane	NMHC	423±308	*p*-ethyltoluene	NMHC	21±15
3-methylhexane	NMHC	252±184	*n*-propylbenzene	NMHC	21±15
2-methylhexane	NMHC	195±142	*o*-ethyltoluene	NMHC	20±15
n-heptane	NMHC	178±130	isopropylbenzene	NMHC/	13±10
methylcyclopentane	NMHC	125±91	1,2,3-trimethylbenzene	NMHC	12±9
2,3-dimethylbutane	NMHC	122±89	1,3,5-trimethylbenzene	NMHC	7±5
n-octane	NMHC	109±80	OVOCs		40695±27180
methylcyclohexane	NMHC	102±74	formaldehyde	OVOCs	10558±5113
2,2-dimethylbutane	NMHC	71±52	ethanol	OVOCs	10537±7136
n-dodecane	NMHC	68±50	methanol	OVOCs	10320±6944
n-decane	NMHC	49±35	acetone	OVOCs	5701±4024
n-nonane	NMHC	47±34	hydroxyacetone	OVOCs	4542±3227
n-undecane	NMHC	41±30	acetaldehyde	OVOCs	3010±1939
Alkenes		2419±2086	methyl ethyl ketone	OVOCs	2714±2277
ethylene	NMHC	1493±1089	acrolein	OVOCs	605±244
propylene	NMHC	411±300	methyl vinyl ketone	OVOCs	185±101
isoprene	BVOCs	351±182	methacrylaldehyde	OVOCs	128±70
1-butene	NMHC	163±119	*m*-cresol	OVOCs	46±43
1-pentene	NMHC	29±21	phenol	OVOCs	26±26
1-hexene	NMHC	15±11			
trans-2-butene	NMHC	11±8			
cis-2-butene	NMHC	11±8			
trans-2-pentene	NMHC	5±3			
cis-2-pentene	NMHC	3±2			
Acetylene		1858±1356			
Acetylene	NMHC	1858±1356			

289 *NMHC: non-methane hydrocarbon, BVOCs: biogenic volatile organic compounds, OVOCs: oxygenated
290 volatile organic compounds.

4.1 *J* values used in the MCM model simulation

The *J* values obtained from two methods (labeled as method I and II) were used in the 3rd-stage 4-min simulation. The Tropospheric Ultraviolet and Visible (TUV) radiation model (version 5.3) (Lantz et al., 1996; Madronich and Flocke, 1999) was used to provide a representative spectral actinic flux in these two methods. The photolysis frequencies of each measured species used in TUV model ($J_{value\ TUV}$) were calculated by numerical summation over wavelength (Calvert et al., 2002):

$$J_{value\ TUV} = \int_a^b \delta_i \times \phi_i \times F_i\ \Delta\lambda_i \tag{S9}$$

where a and b represent the range of the set wavelength, δ_i, ϕ_i, and F_i stand for the absorption cross section, quantum yield, and spectral actinic flux of the species i, respectively. The spectral actinic flux was obtained from the TUV model, detailed information of these two methods is described in Tables S12 and S13.

Table S12. *J* values used in the model simulation in reaction and reference chambers.

	J values used in the model simulation	
	Measured *J* values: $J(NO_2)$, $J(O^1D)$, $J(HONO)$, $J(H_2O_2)$, $J(NO_3\_M)$, $J(NO_3\_R)$, $J(HCHO\_M)$, $J(HCHO\_R)$	Unmeasured *J* values: $J(HNO_3)$, $J(CH_3CHO)$, $J(MACR)$, $J(MEK)$, $J(HOCH_2CHO)$, $J(C_2H_5CHO)$, $J(C_3H_7CHO)$, $J(C_4H_9CHO)$, etc.
Method I	$J_{trans\ measured} \times J_{value\ measured}$	$J_{trans\ TUV} \times J_{NO2\ measured}/J_{NO2_{TUV}} \times J_{valueTUV}$
Method II	$J_{trans\ TUV} \times J_{value\ measured}$	$J_{trans\ TUV} \times J_{NO2\ measured}/J_{NO2_{TUV}} \times J_{valueTUV}$

* $J_{value\ measured}$ represents the measured *J* values of different species, $J_{trans\ measured}$ represents the measured transmittivities of each measured species in the reaction and reference chambers, which are listed in Table S7; $J_{trans\ TUV}$ represents the transmittivities of each measured species used in TUV model in the reaction and reference chambers, where the $J_{trans\ TUV}$ in the reaction chamber is regarded as 100 % $J_{trans\ TUV}$, in the reference chamber is calculated as $\frac{J_{TUV\,390\text{-}790\ nm}}{J_{TUV\,290\text{-}790nm}}$, where $J_{TUV\,390\text{-}790\ nm}$ equals to the *J* value at the wavelength of 390–790 nm, $J_{TUV\,290\text{-}790nm}$ quals to the *J* value at the wavelength of 290–790 nm, the detailed $J_{trans\ TUV}$ values of different species are shown in Table S13; $J_{NO2\ measured}$ and $J_{NO2_{TUV}}$ represent the measured and TUV modeled J_{NO2}.

Table S13. The transmittivities of *J* values used in TUV model ($J_{trans\ TUV}$) described in Table S12.

	Transmittivities							
	$J(NO_2)$	$J(O^1D)$	$J(HONO)$	$J(H_2O_2)$	$J(NO_3\_M)$	$J(NO_3\_R)$	$J(HCHO\_M)$	$J(HCHO\_R)$
Reaction chamber	1.00	1.00	1.00	1.00	1.00	1.00	1.00	1.00
Reference chamber	0.30	0.00	0.01	0.00	1.00	1.00	0.01	0.01

312 **4.2 The modeling results by using *J* values obtained from method II**

313   The variations in the radical mixing ratios (i.e., HO_2, OH, RO_2) and NO_3, NO, NO_2, and O_3 mixing

314 ratios obtained from method I and method II during the 3rd-stage 4-min model simulation are shown in

315 Fig. 8 and Fig. S18, respectively. The production and destruction reactions of HO_2, OH, RO_2, and NO_3

316 in the reaction and reference chambers obtained from methods I and II are shown in Fig. 9 and Fig. S19,

317 respectively, the production and destruction reactions of RO_X in the reaction and reference chambers

318 obtained from methods I and II are shown in Fig. S20, the detailed ROx production pathways of

319 NO_3+VOCs are shown in Fig. S21, and the final modeling results are shown in Fig. 10 and Fig. S22.

320   From Fig. S18, in the reaction chamber, HO_2, OH, RO_2, and NO_3 mixing ratios increased slightly

321 in the first few seconds and then became stable, their final concentrations were 1.97×10^8, 7.61×10^6,

322 1.06×10^8, and 8.36×10^6 molecules cm^{-3}, respectively. In the reference chamber, HO_2, OH, and RO_2

323 concentrations declined in the 1st 20 seconds and then gradually became stable, their final concentrations

324 were 8.11×10^7, 1.08×10^6, and 5.68×10^7 molecules cm^{-3}, respectively. On the contrary, the NO_3 mixing

325 ratio slightly increased at the 1st 1-2 min and then became stable at 1.88×10^7 molecules cm^{-3}.
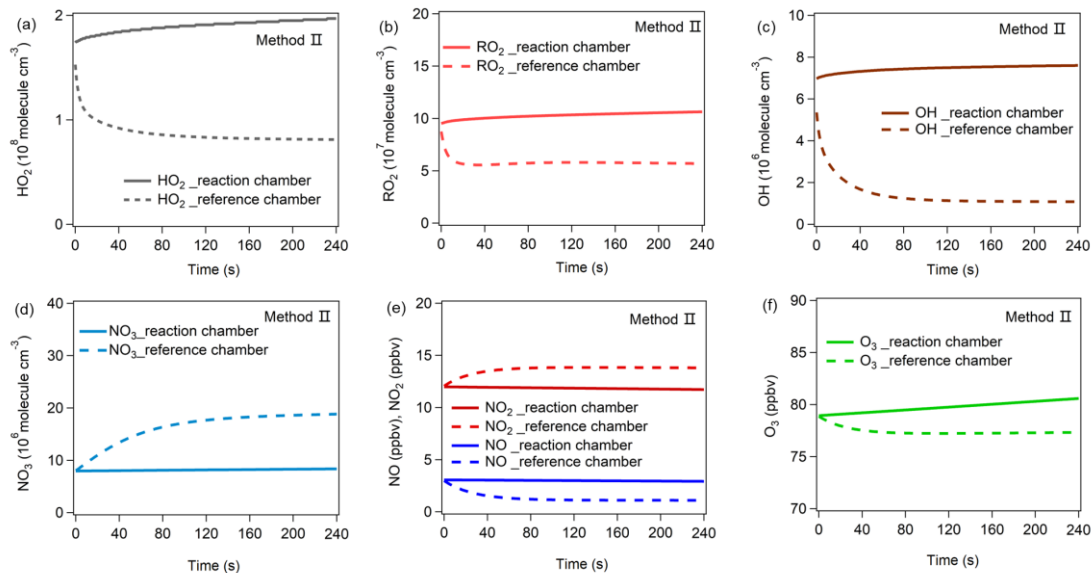
326

327 **Figure S18: The variations of (a) HO_2, (b) RO_2, (c) OH, (d) NO_3 and (e) NO, NO_2, and (f) O_3 mixing ratios**

328 **during the 3rd-stage 4-min model simulation using method II.**

329

330   OH, HO_2, RO_2, and NO_3 concentrations greatly impact the O_3 production and destruction rate. To

331 better understand the factors that drive the OH, HO_2, RO_2, and NO_3 concentration changes in method II,

332 we have added their production and destruction pathways in Fig. S19. We found that the decrease in HO_2

and RO_2 concentrations in the reference chamber in the 1st half minute was mainly due to NO titration effects, as high NO mixing ratios existed during the 1st half minute. The HO_2 and RO_2 concentrations were became stable afterwards, the main production pathway for HO_2 was $RO+O_2$ reaction/RO decomposition, followed by OH+VOCs reaction, OVOCs photolysis (i.e., $C_3H_4O_2$, $C_2H_2O_2$, $C_4H_6O_2$), and NO_3+VOCs reaction; while the main production pathway for RO_2 was OH+ VOCs reaction, followed by OVOCs photolysis (i.e., $C_3H_4O_2$, $C_2H_2O_2$, $C_4H_6O_2$), OH+CO, NO_3+VOCs reaction, etc.; the main destruction pathways for HO_2 and RO_2 were HO2+NO and RO_2+NO, respectively. The main OH production and destruction pathways in the reference chamber was HO_2+NO reaction and OH+ VOCs reaction, respectively. Due to sufficiently high J(NO_3) ($\sim$ 100 % of that in the reaction chamber) and NO_2 concentrations in the reference chamber, the NO_3 photolysis and NO_2+NO_3 reaction consumed NO_3 in the reference chamber, but the NO_3 concentrations were still high due to high production rates of NO_3 at the same time. Similar with the results obtained from method I as described in the main manuscript, for method II, the main NO_3 source in the reference chamber was the NO_2+O_3 reaction, followed by N_2O_5 decomposition. The NO concentrations were relatively high in the 1st minute and consumed NO_3 very quickly, but due to continuous NO_3 sources, the net NO_3 production rates (P(NO_3)$_{net}$) were positive (as shown in Fig. S19b4), which caused the NO_3 concentration to continue to increase (as shown in Fig. S18d). The main difference in NO_3 production in the reference chamber compared to that in the reaction chamber was the much higher N_2O_5 decomposition, which was mainly due to the high NO_2 concentrations in the reference chamber. On the other hand, although the NO+NO_3 reaction was also one of the dominant NO_3 destruction pathways, NO_3 consumed by the NO+NO_3 reaction was significantly smaller than NO_3 produced by the NO_2+O_3 reaction. The integrated production and destruction rates of RO_x are shown in Fig. S20.

356
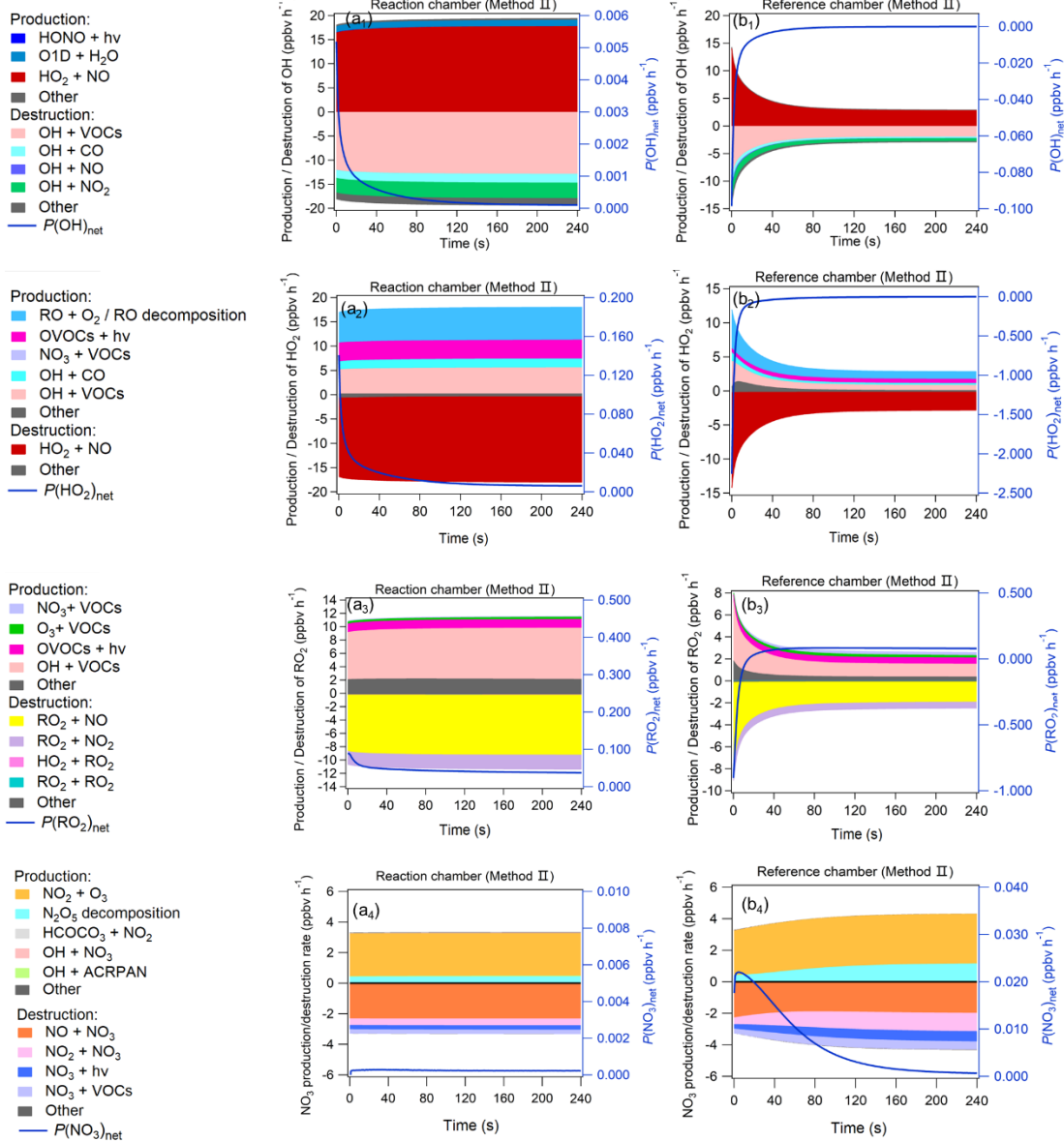
Figure S19: Production and destruction pathways of OH(a_1-b_1), HO_2(a_2-b_2), RO_2(a_3-b_3), and NO_3(a_4-b_4) during the 3rd-stag 4-min model simulation in the reaction and reference chambers in method II (c)-(d).

357

358

359
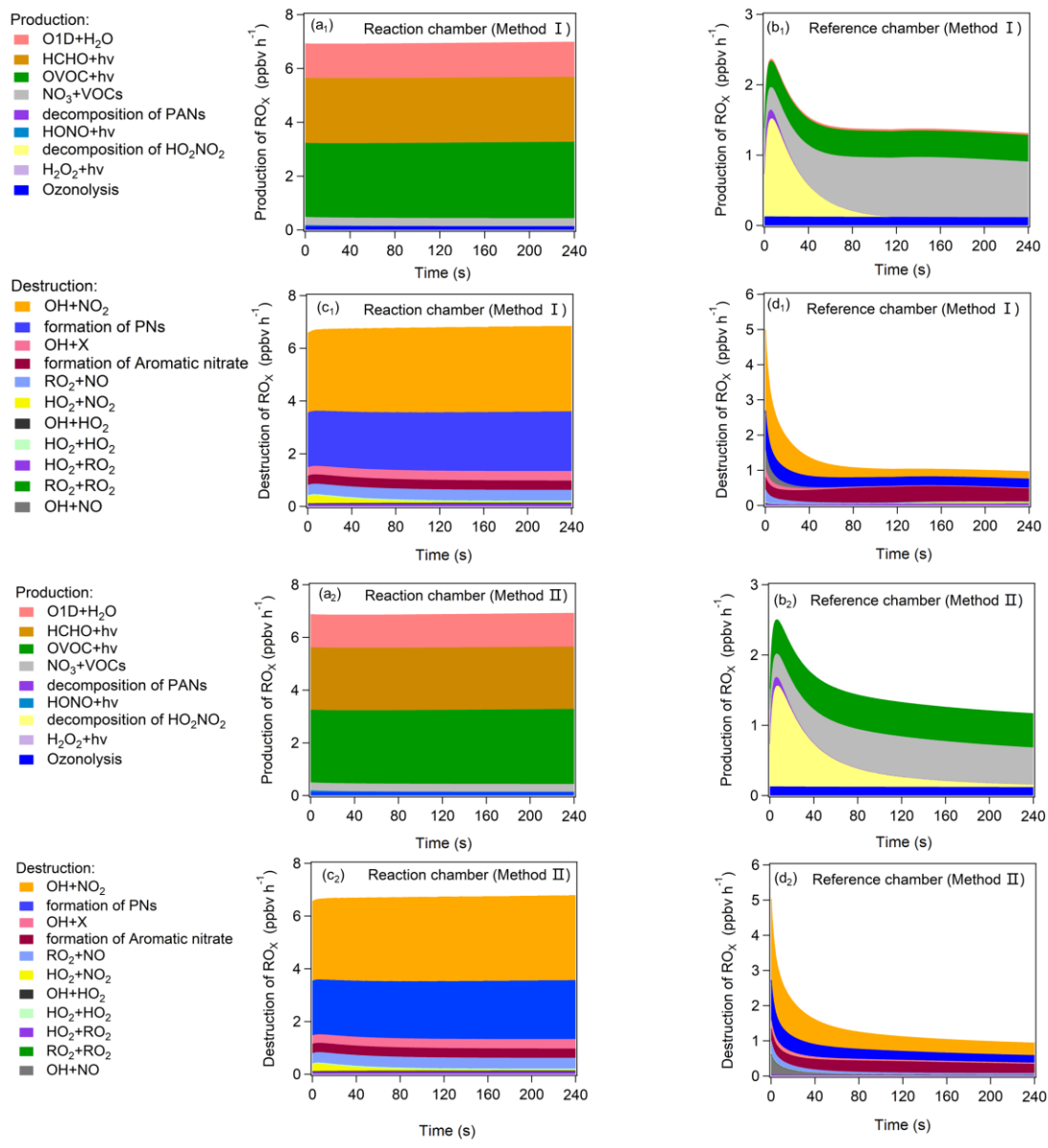
360
361 **Figure S20: Production and destruction pathways of RO$_X$ during the 3rd-stage 4-min model simulation in the**
362 **reaction and reference chambers. (PAN: Peroxyacetyl Nitrate; PNs: formations of all peroxynitrate (including**
363 **CH$_3$O$_2$NO$_2$ and PAN; X: PAN and the net loss of OH+NO to form HONO (usually small)).**
364
365
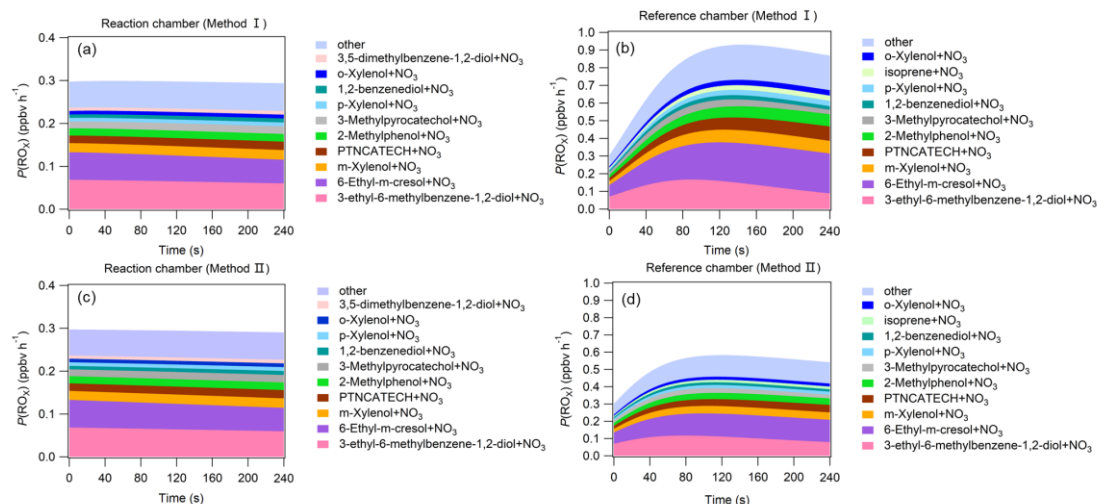
366
367
Figure S21: The $P(ROx)$ pathways related to NO_3+VOCs reactions during the 3rd-stage 4-minute model simulation in the reaction and reference chambers in method I (a)-(b) and method II (c)-(d).

370   Figures S22a–d show the modeled $P(O_3)_{net}$ and the source and sink of various species during the

371   3rd-stage 4-min simulation in method II. Figure S22a shows the steady state of $P(O_3)_{net}$ and the various

372   species in the ambient atmosphere achieved in the last 1 s of the 2nd-stage simulation; Figs. S22b-c show

373   the modeled $P(O_3)_{net}$ and the O_3 chemical budgets in the reaction and reference chambers during the

374   model simulation period; Figure S22d summarized the modeled $P(O_3)_{net}$ in the ambient atmosphere, and

375   that in the reaction and reference chambers, in order to compare the modeled results with our

376   measurement results, we calculated the integral mean of the modeled $P(O_3)_{net}$ in the reaction and

377   reference chambers and appended the related measured $P(O_3)_{net}$ value during this 4-min simulation time

378   onto Fig. S22d. Further, the reaction weights of different production and destruction reactions process of

379   O_3 are shown in Figs. S22e–h.

380

381
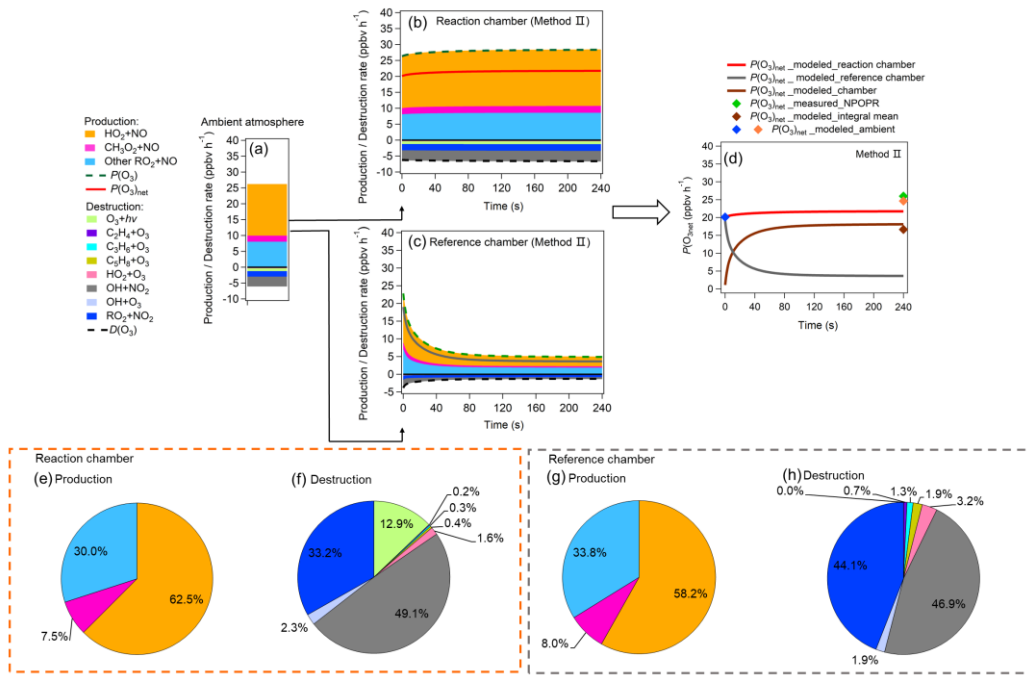
Figure S22: (a)–(c) show the modeled $P(O_3)_{net}$ and the O_3 chemical budgets in (a) the ambient atmosphere when injected into the reaction and reference chambers and (b–c) the reaction and reference chambers during the 4-min model simulation; (d) shows $P(O_3)_{net}$, where $P(O_3)_{net\_modeled\_ambient}$ represent the modeled $P(O_3)_{net}$ in the ambient air at the time before (blue marker) and after (orange marker) the sampled ambient air was injected into the dual-channel reaction chamber. $P(O_3)_{net\_modeled\_reaction}$ chamber and $P(O_3)_{net\_modeled\_reference}$ chamber represent the $P(O_3)_{net}$ changing trend during the 4-min photochemical reactions in the reaction and reference chambers, respectively, $P(O_3)_{net\_modeled\_chamber} = P(O_3)_{net\_modeled\_reaction}$ chamber–$P(O_3)_{net\_modeled\_reference}$ chamber, $P(O_3)_{net\_modeled\_integral}$ mean represents the integral mean of the $P(O_3)_{net\_modeled\_chamber}$, and $P(O_3)_{net\_measured\_NPOPR}$ represent the measured $P(O_3)_{net}$ by NPOPR detection system. (e)–(h) show the reaction weights of each production and destruction reactions process of O_3 in the reaction and reference chambers in method II.

393

394

395   **Figure S23: $P(O_3)_{net}$ changing in the reaction and reference chambers in method I with ± 5 % of measured**

396   **NO₂.**
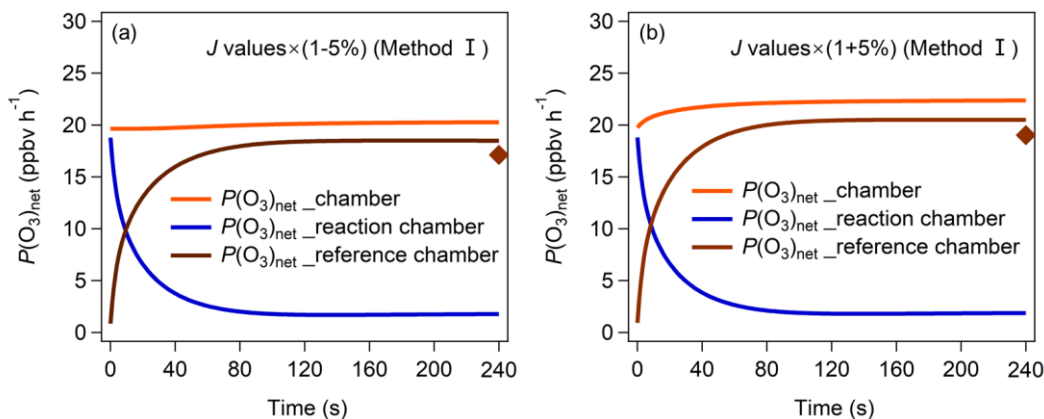
397

398   **Figure S24: $P(O_3)_{net}$ changing in the reaction and reference chambers in method I with ± 5 % of measured J**

399   **values.**

400   From Fig. S22, the $P(O_3)$ and $D(O_3)$ were almost the same within the 4-min reaction in the reaction

401   chamber (all species reached a steady state condition), while the $P(O_3)$ and $D(O_3)$ in the reference

402   chamber decreased significantly within the 1st minute, and kept stable in the following minutes. In the

403   reaction chamber, the HO_2+NO reaction contributed most to $P(O_3)$, accounting for 62.5 % of the total

404    $P(O_3)$, with the integral mean value of 17.5 ppbv h⁻¹ in the reaction chamber. The second important

405   pathway of $P(O_3)$ was RO_2+NO (occupied 37.5 % of the total $P(O_3)$). The reaction of RO_2+NO contained

406   more than 1200 types of RO_2 radicals, and the pathway of CH_3O_2+NO contributed 7.5 % of the total

407    $P(O_3)$. The most important contributor of $D(O_3)$ was OH+NO_2 (49.1 %), followed by RO_2+NO_2 (33.2 %),

408   O_3 photolysis (12.9 %), O_3+OH (2.3 %), O_3+HO_2 (1.6 %), C_5H_8+O_3 (0.4 %), C_3H_6+O_3 (0.3 %), and

409   C_2H_4+O_3 (0.2 %). In the reference chamber, the integral mean value of $P(O_3)$ was 3.7 ppbv h⁻¹, the

410   HO_2+NO contributed most to $P(O_3)$ (accounting for 58.2 % of the total $P(O_3)$), followed by RO_2+NO

411   (occupied 41.8 % of the total $P(O_3)$), in which the CH_3O_2+NO contributed 8.0 % of the total $P(O_3)$. The

412   most important contributor of $D(O_3)$ was OH+NO_2 (46.9 %), followed by RO_2+NO_2 (44.1 %), O_3+HO_2

413   (3.2 %), C_5H_8+O_3 (1.9 %), O_3+OH (1.9 %), C_3H_6+O_3 (1.3 %), C_2H_4+O_3 (0.7 %), and O_3 photolysis

414   (0.0 %). For all $P(O_3)$ reactions, the weight of RO_2+NO reaction in the reference chamber was 4.3 %

415   higher than that in the reaction chamber, however, for all $D(O_3)$ reactions, the weight of RO_2+NO_2

416   reaction in the reference chamber was 10.9 % higher than that in the reaction chamber, which will

417   somehow mitigate the high $P(O_3)$ caused by RO_2+NO in the reference chamber. Figure S22d shows that

418   the $P(O_3)_{net}$ (26.0 ppbv h^{-1}) measured by the NPOPR detection system was 9.3 ppbv h^{-1} higher than the

419   modeled value (16.7 ppbv h^{-1}). This difference was much larger than 7.5 ppbv h^{-1} obtained from method

420   I, this may be due to the transmittance of $J(NO_2)$ in the reference chamber in method II ($\sim$ 30 %) was

421   much higher than that in method I ($\sim$ 9 %), NO_2 photolysis products NO, it involved in the main O_3

422   production reactions HO_2+NO and RO_2+NO, so the modeled $P(O_3)_{net}$ in the reference chamber was

423   slightly overestimated in method II, thus leading to an underestimation of total $P(O_3)_{net}$.

424

425 **References**

426 Baier, B. C., Brune, W. H., Lefer, B. L., Miller, D. O., and Martins, D. K.: Direct ozone production rate

427 measurements and their use in assessing ozone source and receptor regions for Houston in 2013, Atmos.

428 Environ., 114, 83-91, http://dx.doi.org/10.1016/j.atmosenv.2015.05.033, 2015.

429 Calvert, J.G., Atkinson, R., Becker, K.H., Kamens, R.M., Seinfeld, J.H., Wallington, T.H., Yarwood, G.:

430 The mechanisms of atmospheric oxidation of the aromatic hydrocarbons, Oxford University Press,

431 2002.

432 Cazorla, M., and Brune, W. H.: Measurement of ozone production sensor, Atmos. Meas. Tech., 3, 545-

433 555, https://doi.org/10.5194/amt-3-545-2010, 2010.

434 Chen, S., Ren, X., Mao, J., Chen, Z., Brune, W. H., Lefer, B., Rappenglück, B., Flynn, J., Olson, J., and

435 Crawford, J. H.: A comparison of chemical mechanisms based on TRAMP-2006 field data, Atmos.

436 Environ., 44, 4116-4125, https://doi.org/10.1016/j.atmosenv.2009.05.027, 2010.

437 Chen, S., and Brune, W. H.: Global sensitivity analysis of ozone production and O_3-NO_X-VOC limitation

438 based on field data, Atmos. Environ., 55, 288-296, https://doi.org/10.1016/j.atmosenv.2012.03.061,

439 2012.

440 Deshpande, R. D., Medha, D., Virendra, P., Kumar, H., & Gupta, S. K. : Water vapor source identiffcation

441 for daily rain events at Ahmedabad in semi-arid western India: Wind trajectory analyses.

442 Meteorological Applications, 22, 754–762. https://doi.org/10.1002/met.1515, 2016.

443 Emmerson. K. M., Carslaw. N. C., Carslaw. D. C., Lee. J. D., McFiggans. G., Bloss. W. J., Gravestock.

444 T., Heard. D. E., Hopkins. J., Ingham. T., Pilling. M. J., Smith. S. C., Jacob. M., and Monks. P. S.: Free

445 radical modelling studies during the UK TORCH Campaign in Summer 2003, Atmos. Chem. Phys., 7,

446 167–181, https://doi.org/10.5194/acp-7-167-2007, 2007.

447 Hao, C., Song, L., and Zhao, W.: HYSPLIT-based demarcation of regions affected by water vapors from

448 the South China Sea and the Bay of Bengal, European Journal of Remote Sensing, 54, 348-355,

449 https://doi.org/10.1080/22797254.2020.1795730, 2020.

450 Kanaya, Y., Tanimoto, H., Yokouchi, Y., Fumikazu Taketani, F. T., Komazaki, Y., Irie, H., Takashima, H.,

451 Pan, X., Nozoe, S., and Inomata, S.: Diagnosis of photochemical ozone production rates and limiting

452 factors in continental outflow air masses reaching Fukue Island, Japan: ozone-control implications,

453 Aerosol. Air. Qual. Res., 16, 430-441, https://doi.org/10.4209/aaqr.2015.04.0220, 2016.

Lantz, K.O., Shetter, R.E., Cantrell, C.A., Flocke, S.J., Calvert, J.G., Madronich, S.: Theoretical, actinometric, and radiometric determinations of the photolysis rate coefficient of NO2 during the Mauna Loa Observatory Photochemistry Experiment 2, J. Geophys. Res.-Atmos., 101, 14613-14630, https://doi.org/10.1029/96JD00215,1996.

Madronich, S. and Flocke, S. (ed. by P. Boule): The role of solar radiation in atmospheric chemistry, 2, Environmental photochemistry, 1-26, 1999.

Mazzuca, G. M., Ren, X., Loughner, C. P., Estes, M., Crawford, J. H., Pickering, K. E., Weinheimer, A. J., and Dickerson, R. R.: Ozone production and its sensitivity to NOx and VOCs: results from the DISCOVER-AQ field experiment, Houston 2013, Atmos. Chem. Phys., 16, 14463-14474, https://doi.org/10.5194/acp-16-14463-2016, 2016.

Ren, X., van Duin, D., Cazorla, M., Chen, S., Mao, J., Zhang, L., Brune, W. H., Flynn, J. H., Grossberg, N., Lefer, B. L., Rappenglück, B., Wong, K. W., Tsai, C., Stutz, J., Dibb, J. E., Thomas Jobson, B., Luke, W. T., and Kelley, P.: Atmospheric oxidation chemistry and ozone production: Results from SHARP 2009 in Houston, Texas, J. Geophys. Res.-Atmos., 118, 5770-5780, https://doi.org/10.1002/jgrd.50342, 2013.

Sadanaga, Y., Kawasaki, S., Tanaka, Y., Kajii, Y., and Bandow, H.: New system for measuring the photochemical ozone production rate in the atmosphere, Environ. Sci. Technol., 51, 2871-2878, https://doi.org/10.1021/acs.est.6b04639, 2017.

Sklaveniti, S., Locoge, N., Stevens, P. S., Wood, E., Kundu, S., and Dusanter, S.: Development of an instrument for direct ozone production rate measurements: measurement reliability and current limitations, Atmos. Meas. Tech., 11, 741-761, https://doi.org/10.5194/amt-11-741-2018, 2018.